HYDROXYAPATITE – TZP COMPOSITES: PROCESSING, MECHANICAL PROPERTIES, MICROSTRUCTURE AND IN VITRO BIOACTIVITY

A Thesis Submitted in Partial Fulfillment of the
Requirements for the Degree of

DOCTOR OF PHILOSOPHY

in

ENGINEERING

by

YOUGOJOTI NAYAK
(Roll No: 50408005)

Supervisors:
Dr. Santanu Bhattacharyya
Dr. Smrutisikha Bal

DEPARTMENT OF CERAMIC ENGINEERING
NATIONAL INSTITUTE OF TECHNOLOGY ROURKELA
November, 2010

NATIONAL INSTITUTE OF TECHNOLOGY
ROURKELA, INDIA

CERTIFICATE

This is to certify that the thesis entitled "Hydroxyapatite – TZP Composites: Processing, Mechanical Properties, Microstructure and In vitro Bioactivity" being submitted by Mr. Yougojoti Nayak for the degree of Doctor of Philosophy in Engineering, is a record of bonafied research work carried out by him. To the best of our knowledge, the work has not been submitted to any other University or Institute for the award of any degree or diploma.

(Smrutisikha Bal)	(Santanu Bhattacharyya)
Co-Supervisor	Supervisor

CONTENTS

Chapter I - Introduction

Chapter II - Literature Review

Chapter IV - Experimental Work

Chapter V - Results and Discussions

Section A

Processing and Characterization of Hydroxyapatite

Section B

Processing and Characterization of HA-YTZP Composites

Section C

Effect of TZP Calcination Temperature

Section D

Phase,Density, Microstructure and Mechanical Properties of Hot Pressed HA-TZP Composites

Chapter VI - Results and Discussions – In Vitro Tests of HA and HA-TZP Composites

Chapter VII- Conclusions and Scope of Further work

Publications resulting from the Ph.D. work

Curriculum Vitae

Abstract

The present study describes the results on hydroxyapatite (HA)-TZP (tetragonal zirconia polycrystal) composites containing low weight percent TZP (2, 5, 7.5 and 10 wt%). The work could be divided into two parts. In the first part, hydroxyapatite was synthesized by two different chemical precipitation route; normal precipitation (NP) and reverse strike precipitation (RS) using $Ca(NO_3)_2.4H_2O$ and $(NH_4)_2HPO_4$ as the precursor for hydroxyapatite. The as precipitated amorphous powders were studied for thermal decomposition behavior (DSC/TG), phase evolution and phase stability of the calcined powder, particle size distribution and non-isothermal densification behaviour. The TEM of the calcined hydroxyapatite powder shows that HA particles prepared from both the routes have elongated morphology. The particle size distribution of $850^{O}C$ calcined powder is multimodal for NP and monomodal for RS route. The sintered density of RS route HA is higher than that of NP route for the entire sintering range studied. The results also indicate that while RS-HA remains phase stabile until $1250^{O}C$, NP-HA decomposes to a mixture of HA and TCP at that temperature.

Based on the above observations, the RS route was adopted for synthesis of HA-3Y-TZP composite containing 2, 5, 7.5 and 10 wt% of TZP respectively. The composite powders were also characterized by FTIR, DSC/TG, XRD and TEM. The raw HA-TZP powders crystallized between $650^{O}C$-$1050^{O}C$ and the calcined powder ($850^{O}C$/2hrs) had phase pure HA and TZP. The composites were sintered by pressureless sintering at $1250^{O}C$/4hrs. XRD of the sintered composites revealed that at higher TZP content (HZ5, HZ7 and HZ10), β-TCP and α-TCP along with HA and t-ZrO_2 were present. The TEM of calcined powder showed dark coloured TZP particles (5-10 nm) uniformly distributed in light colored HA (50-150 nm) matrix. The highest sintered density (> 99%) was obtained for HA- 2wt% TZP composite (HZ2). The density for 5, 7.5 and 10 wt% TZP containing composites were 96%, 92% and 90% respectively. The fracture strength of the composites appeared to be controlled by the size of the largest flaw present in the sintered sample. The highest three point bending strength was 72MPa for HZ2 composite while 30MPa was lowest for HZ5 composite. The decrease in strength at higher TZP additions could be due to the incomplete densification of the composite due

to the constraining effect of TZP. The highest fracture toughness (0.97MPam$^{1/2}$) was recorded for HA-5 wt% TZP (HZ5). SEM microstructure showed a bimodal grain size distribution with presence of very fine and coarse grains. A grain size reduction of HA was observed with TZP addition. It may be pointed out here that at a lower TZP calcination temperature (850^{O}C), the fine TZP particles forms agglomerates thereby hampering the final stage of densification. The Vickers hardness exhibited also porosity dependence. The maximum hardness (3.83GPa) was for HZ2 and the lowest (2.43GPa) was for HZ10 composites. Thus, it was anticipated that an effort should be made to increase the sintered density particularly at higher wt% TZP (i.e. 5, 7.5 and 10) which could effectively improve the strength, toughness and hardness of the composite. Therefore, in the next stage of work, an effort was made to observe the effect of TZP calcination temperature on the agglomeration behaviour of TZP and thereby on sintered density, phases, mechanical properties and microstructure of HA-TZP composites.

Therefore as discussed above, calcination temperature of TZP was increased from 850^{O}C to 1200^{O}C. It was observed that the calcination temperature had a considerable effect on the densification behaviour, phase retention, strength, toughness, hardness and microstructure of composites. Two different sets of the HA-TZP composite were prepared from TZP powders which have been calcined at two different temperatures (viz 850^{O}C and 1200^{O}C). The composites prepared from both type of TZPs were sintered in air at 1250^{O}C/4hours. When TZP was calcined at 850^{O}C, the prepared HA-TZP composites had low sintered density (except for 2% TZP composition), relatively low strength (37 MPa), toughness (0.8 MPam$^{1/2}$) and hardness (2.4 GPa) for HZ10 composite but significant amount of retained HA and TZP even at higher TZP loading such as 5, 7.5 and 10 wt%. A higher TZP calcination temperature caused a reduction in HA and TZP phase retention along with the formation of $CaZrO_3$ and TCP. Microstructure shows a substantial increase in HA grain size with increase in TZP amount. In the HA-TZP composite, containing 1200^{O}C calcined TZP, sintered density improved for all the HA-TZP compositions along with an increase in strength toughness and hardness. The maximum bending strength, fracture toughness and hardness were 65 MPa, 1.6 MPam$^{1/2}$ and 5.25 GPa respectively obtained for HA-10 wt% TZP

composite. Unlike the 850^{O}C calcined TZP batch, the strength was independent of flaw size. It was noticed that the highest strength also had high $CaZrO_3$ content thereby suggesting the presence of $CaZrO_3$ contributed to strength increase. The fracture toughness trend suggested that microcrack toughening is a contributing factor for toughness increment. It was thought the reactions between HA and TZP could be effectively suppressed or avoided by using a faster and low temperature sintering technique such as hot pressing. The hot pressed (950^{O}C/30 MPa) composites showed remarkable improvement in sintered density and phase retention. The XRD results revealed that HA and TZP were major phase in hot pressed HA-TZP composites which is strikingly different from the pressureless sintered composites. The densities of hot pressed composites are > 98% irrespective of their composition and TZP calcination temperature. The maximum flexural strength (120 MPa) and hardness (5.8GPa) was obtained for HZ2 composite containing TZP calcined at 850^{O}C (H2Z8). The toughness value is maximum (1.5 MPa$\sqrt{}$m) for HZ10 composite containing TZP calcined at 1200^{O}C (H10Z12). The SEM microstructure of hot pressed HA-TZP composite showed the HA grain size to be in the range of 200nm.

The in vitro bioactivity test was performed in our laboratory using standard SBF solution. The bioactivity tests showed apatite formation on the surface of HA-TZP composites. The volume fraction of apatite formed its morphology and size was dependent on the HA-TZP composites as well as on aging time. The cytotoxicity tests were conducted as per ISO 10993-5 using L929 mouse fibroblast cells. No toxic effects of the specimens on the cells were observed thus confirming the nontoxic behaviour of the composites after 24 hours of exposure. The blood compatibility of the composite was also examined as per ISO 10993-4 by an in-vitro hemocompatibility test using human blood and none of the composite has induced haemolysis during the scheduled exposure period.

Key words:
Hydroxyapatite (HA), HA-TZP, Density, Phase, Microstructure, Mechanical property, Calcination temperature, Hot pressing, Invitro bioactivity, Invitro biocompatibility, Invitro hemocompatibility.

ACKNOWLEDGEMENTS

I wish to express my sincere thanks my supervisor Prof. Santanu Bhattacharyya, Department of Ceramic Engineering, National Institute of Technology, Rourkela for introducing the present topic and for his guidance and valuable suggestions throughout this work. I am also grateful to my co supervisor Prof. Smrutisikha Bal for her encouragements, advice and suggestions.

I express my sincere thanks to Prof J Bera, Head, Ceramic Engineering for providing me all the departmental facilities required for the completion of the thesis.

I am grateful to Prof. Swadesh Pratihar, who’s out of the way help and guidance helped the thesis to reach the final shape. I am also thankful to all other faculty members of Ceramic Engineering Department, NIT Rourkela for their constructive suggestions and encouragement during the completion stage of the thesis.

I am grateful to Prof V Jayaram, Chairman, Materials Engineering, IISc Bangalore for providing me the hot pressing, SEM and other characterization facilities for completing the work as well as for sponsoring my stay at IISc Bangalore during the period of work.

I am thankful to Director, SCTIMST, Thiruvananthapuram for permitting me to carry out the cytoxicity and hemolysis tests in his institute.

I am also thankful to SAIF, IIT Bombay for providing the TEM analysis.

I gratefully acknowledge the financial assistance received from department of Science & Technology for completing the research at NIT Rourkela

Last but not the least, I am thankful to all the research scholars and non- teaching and technical staff members in Department of Ceramic Engineering for providing all joyful environments in the lab and helping me out in different ways.

YOUGOJOTI NAYAK

LIST OF FIGURES

Fig. No **Figure Caption** **Page No**

Chapter II - Literature Review

Chapter IV - Experimental Work

Chapter V - Results and Discussions

Chapter VI - Results and Discussion – In Vitro Tests

LIST OF TABLES

Table No **Table Caption** **PageNo**

Chapter II - Literature Review

Chapter IV - Experimental

Chapter V - Results and Discussion

Chapter VI - Results and Discussion – In Vitro Tests

Chapter I

Introduction

1. Introduction

For the last 40 years, ceramics materials are increasingly being used for the repair and reconstruction of skeletal diseases and disorders [1.1]. The term bioceramics are being used for those manmade materials which are being used as medical implant and exhibit specific positive response within the body aimed for the repair or augmentation of damaged tissue and/or skeletal parts. These bioceramic materials particularly calcium phosphate based materials are being preferred mainly as bone substitute or scaffolds due to its biocompatibility, better bone and tissue bonding ability, and its compositional similarity with the inorganic components of human bone [1.2 - 1.4]. Many of these bioceramics materials also possess excellent chemical resistance, compressive strength and wear resistance. However, there are some bioceramic materials which are inert in their bioactive response. This implies that the "bioinert" biomaterials lacks strong bond at the interface between the implant and the host tissue and are bonded through a fibrous capsule of non adhering tissue.

During 1970-90's, extensive research had been carried on the processing and property tailoring of bioceramic materials at different corners of the world which very much paved the way for present status of popularity of biomaterials and bioceramics. During this period, besides hydroxyapatite, other important bioceramics materials like bioglass, A/W glass-ceramics, calcium phosphate based ceramics, hydroxyapatite-polyethylene composites etc were developed and most of the above materials have also been successfully commercialized [1.5 - 1.7]. The development obstacles and the trials from laboratory to clinic were the results of systematic investigation and hard work of a large number of contributors like Profs Hench, Bonfield, Degroot, Kokubo, Jarco and many others. In the following sections, some of the more important bioceramic materials as well as their composites (which have been successfully implanted in humans) and their characteristics have been more elaborately discussed:

1.1 Bioglass:

Prof. Hench's phenomenal work on bioglass had its concept from the exorbitant amputation cost required for patients requiring amputations, particularly during the war times. The developed Na_2O-CaO-P_2O_5-SiO_2 based bioglass system was expected to form a direct bond with the tissue eliminating the interfacial scar tissue (which normally resulted from the use of metallic and polymeric implants). The bone bonding ability was enhanced with B_2O_3 and CaF_2 addition. The widely used bioglass composition is 45S5 (45 wt% SiO_2, Na_2O, CaO and 6% P_2O_5). 45S5 bioglass was highly bioactive (bioactivity index (I_b) = 8-10) due to the rapid formation of HCA layer on its surface in physiological body fluid or simulated body fluid. This bioglass composition underwent very rapid surface reaction with the physiological fluid or simulated body fluid thereby forming an apatite (Ca-P) like amorphous structure on its surface [1.8, 1.9]. Subsequently, the "apatite" like amorphous structure absorbed CO_3^- from the body fluid and converted to hydroxycarbonate apatite (HCA) resulting in bone bonding. The percentage of silica in bioglass controlled the nature of tissue bonding ability. When $SiO_2 \leq 53\%$, the bioglass bonded to both soft and hard tissues, between 54-60% SiO_2, bioglass could bond only with hard tissue [1.10, 1.11] and for $SiO_2 > 60\%$, bone bonding did not take place at all. The time required for bone bonding increased with SiO_2 content- higher SiO_2 amount required a longer time for HCA layer formation. Hench et.al divided all bioactive materials into two classes A and B. Class A bioactive materials had bone osteogenic and osteoproduction properties while class B bioactive materials had only osteoconductive properties [1.12, 1.13]. Excellent reports by Hatton, Hoeland, Anderson and Knowles have also documented the detailed work on the different bioglass compositions and their clinical investigations [1.14-1.17].

1.2 A-W Glass – Ceramic

Apatite-Wallastonite (A/W) glass- ceramic system originally developed by Kokubo et.al is another important class of bioactive bioceramic material [1.18]. In addition to its excellent bone and tissue bonding ability, this composite has two more added advantages- improved fracture strength and toughness and improved machinability. In A/W glass ceramic, the major crystalline phases i.e. oxyfluroapatite ($Ca_{10}(PO_4)_6(OF)_2$) and β-wollastonite ($CaO\text{-}SiO_2$) reinforce $MgO\text{-}CaO\text{-}SiO_2$ based glass matrix [1.19]. The high bending strength, fracture toughness along with comparable Young's modulus permits its use different load bearing components [1.20, 1.21].

1.3 Calcium Phosphates

Calcium phosphate based group members notably hydroxyapatite and tricalcium phosphate form an important class of bioceramic materials owing to their chemical similarity with natural bone [1.22].

1.3.1 Hydroxyapatite

Hydroxyapatite (HA) ($Ca_{10}(PO_4)_6(OH)_2$) is one of the most important member of calcium phosphate group [1.23, 1.24]. The mineralogical composition of HA resembles that of natural bone. This factor permits the use of HA and HA based composites in many different implantable applications [1.25]. However, I_B value of HA is much less than that of bioglass and A/W glass-ceramics. Where, I_B an index of bioactivity as introduced by Hench to measure the level of bioactivity is defined as:

$$I_B = 100/\ t_{0.5bb}$$

Where $t_{0.5bb}$ = time required for more than 50 % of the interface to get bonded [1.26]. This implies that HA will provide only hard tissue bonding [1.27]. While dense HA are mostly used as implants materials; porous HA are mainly used as a scaffold material [1.4]. The ideal Ca/P for HA is 1.667 (mole ratio) and 2.151 (weight ratio). Both cationic and anionic substitutions can take place in HA [1.28]. The ionic substitution affects the lattice parameters, crystal morphology, crystallinity, solubility and phase stability of HA phase. The cationic substitutions include Na^+, Mg^+, Sr^+, K+ and Mn^{++}. Anionic substitutions can replace either $(PO_4)^{3-}$ or $(OH)^-$. Fluroapatite and chloroapatite are examples anionic substitutions in HA [1.29]. Another important anionic substituted HA is carbonated hydroxyapatite (CHA) [1.30]. This has been a widely studied subject because of its similarity and abundance in bone mineral. It has been reported that carbonate ions substituted HA, due to its higher dissolution rate can cause increased bioactivity and an increased rate of bone apposition around dense HA implant [1.31]. The relatively slow rate of bone bonding ability of HA can be improved by incorporation/absorption of biological moieties such as growth factors proteins and cells in HA. Similarly, HA can also be chemically doped with (≤ 20 mol%) of elements like Si. The silicon substituted HA (Si-HA) demonstrates a significant increase in the bone apposition amount and organization around Si-HA implants.

1.3.2 Tricalcium Phosphate

Tricalcium phosphate (TCP) is a biodegradable ceramic having higher solubility in physiological fluids with respect to HA. Among the four different polymorphs, α and $\beta-$TCP are the common varieties, which occur during decomposition of HA. When Ca/P ratio of HA is < 1.67, TCP are most likely phases that form during thermal decomposition of HA [1.32]. The biodegradability of TCP (or the high dissolution rate) is an important parameter for situations when bone regrowth is possible from the scaffold. The scaffold is supposed to dissolve with progressive growth of new bone. It has been reported that for TCP with Ca/P = 1.5, the dissolution rate is high. In certain instances, mixtures of HA and TCP commonly known biphasic calcium phosphate (BCP) have also been investigated as bone substitutes [1.33]

1.4 Hydroxyapatite Coatings:

The uses of HA for load bearing application or orthopedic implant are limited owing to HA's low strength, toughness and modulus. On the other hand, the use of metals (316L, Ti alloy) causes resorption and weakening of existing bone structure due to stress shielding effect. A compromise is made by coating HA on metallic implants. The coating provides the bioactive layer for bond formation with the tissues and also prevents the metallic corrosion [1.34]. On the other hand, metallic implants possess the requisite strength and toughness. The HA coating is mostly applied through plasma spraying method as well as by ion beam sputtering technique and thermal spray method. Clinical results have demonstrated good bonding and bone deposition on coated metallic implants. De Groot et.al [1.35] and Furlong et.al [1.36] have elaborated on the processing of plasma sprayed HA coating. Coating thickness depends on volume fraction of HA in spray and the feed rate. Adherence and bond strength depends on coating thickness – the optimum coating thickness being 50-100 μm [1.37]. The degree of crystallinity of HA coating will affect the dissolution rate, in vitro biological behaviour as well as phase stability of HA phase. The plasma sprayed coated implant are now being used on younger patients [1.38]. Although successful, a thicker plasma sprayed HA films often lead to poor interfacial strength between coating and substrate. On account of this, a number of other coating methods (most of them operating at low temperature) have been investigated and have been successful in making thin HA coatings. They are electrophoresis, sol-gel, electrochemical routes, biomimetic coating, electrospray deposition, sputter technique.

1.5 Calcium Phosphate based Filler Materials and Bone Cements

Bonfield et.al first investigated the use of calcium phosphate (HA) as a filler material in polymer matrix, thereby improving the mechanical properties and bioactivity of the composites [1.39]. The developed composite materials (using calcium phosphate/hydroxyapatite) as a filler material in a polymeric matrix which has been widely used is HAPEX. The advantages of polymer-matrix calcium phosphate composites are improved plasticity, toughness, strength and ease of shaping at the operation table itself. The polymer-HA combination can also be used to prepare graded composites having a wide range of stiffness from one face of the composites to the other. Calcium phosphates have also been used as injectable bone cement providing a means for in situ moulding. A wide variety of calcium phosphate combinations (calcium phosphate + dicalcium phosphate) have also been used as bone cement [1.40]. However, the uses of bone cement for fixing of implants are no longer recommended due to the possibility of damage to the healthy tissues due to the high heat of setting of bone cements.

1.6 Calcium Phosphate Based Bone Grafting Materials for Tissue Engineering

Increased use of biomaterials or bio-ceramic materials will depend how the material can be adapted/modified to permit tissue engineering with the help of implant [1.41, 1.42]. The methodology of tissue engineering essentially requires the use of a scaffold for onsite cell delivery. Preferably scaffolds should have 70-80% porosity with high degree of interconnectivity. The pore size (large fenestration) of the scaffold should be ≥ 100μm to permit healthy growth of tissue as well as for vascularization.

The present day bone grafting primarily relies on natural bone materials – often the bone from another operation, due to limited availability of such grafting material.

1.7 Hydroxyapatite Based Composites - Present and Future Trend

At present there is a growing demand of orthopedic implants which helps in improving the quality of life of the patients. Among the various form of implants available, synthetic implants have a major role to play. The emergence of synthetic bone graft has significantly reduced the use of autogenous and allogenic bones which are the potential carrier of viral and bacterial infections from the doner. On the other hand, use of ceramic implants prepared by high temperature processing eliminates the risk of bacterial and viral infection. Among the various ceramic implants hydroxyapatite based implants are known to promote bone growth and form a strong and effective bonding with bone tissue. However, owing to its relatively poor mechanical properties and brittleness (strength and toughness) it has been used mostly in non load bearing areas. The use of HA in load bearing parts can be explored provided the strength and toughness of HA can be increased. Among many oxide reinforcements, ZrO_2 is an important one, which has been used to increase the strength and toughness of Al_2O_3, mullite, spinel and many other ceramic materials. High sintered density and ultra fine particles (in the nano range) will ensure ZrO_2 mostly in tetragonal phase leading to improve mechanical properties of the composites via dispersion strengthening.

The initial successes of HAPEX, led the scientists and technologists to work towards the development of different hydroxyapatite based composite materials [1.43, 1.44]. The reinforcements included A-W glass ceramics, bioglass (in polyethylene) [1.45, 1.46] etc. Current researches have also tried to incorporate, Al_2O_3, mullite, TiO_2, ZrO_2 and carbon nanotubes in hydroxyapatite matrix with an aim to improve the mechanical performance of the latter [1.47, 1.48]. While in HA-nano carbon composites, the reaction between HA and reinforcement is not a major issue, it becomes an important factor when Al_2O_3, TiO_2 and ZrO_2 (either as monoclinic ZrO_2 or as tetragonal zirconia polycrystals) are the reinforcements for HA. The reasons for this enhanced reaction comes from the high affinity of CaO towards Al_2O_3, TiO_2 and ZrO_2 leading to a premature decomposition of HA. Thus, the processing of these composites becomes tricky and challenging. The main aim should be to retain the reinforcement and matrix phases as much as possible in the sintered composites.

1.8 Fixation of Prosthesis to Bone and Initial Biological Events Surrounding an Implant

Non HA coated prosthesis stems are fixed to bone by a number of processes. If the prosthesis is bio inert (e.g. dense alumina, zirconia etc), and the implant does not form an interfacial bonding with bone, the fixation is done by mechanical interlocking. However, in case of porous implant a mechanical fixation is obtained through tissue ingrowths into pores (termed as biological fixation) [1.49]. The use of bone cement such as PMMA and PEMA is another option for fixing prosthesis stems to bone [1.34]. However, a cement less prosthesis is more desirable. This shift from cemented fixation to cementless fixation is due to longer life of cement less fixation as compared to cemented prosthesis. Moreover, in most of the cases polymeric bone cements (PMMA, PEMA) also results in the death of bone tissues (bone necrosis) at the interface due to an exothermic reaction during polymerization of bone cement.

The clinical success of any implant depends on two major factors: formation of a stable interface with the connective tissue and functional matching of the mechanical property of the implant with the surrounding tissues. However, the problem lies in the fact that not many materials including few ceramics satisfy such criteria.

There are certain unavoidable issues associated with any type of implantation. There is damage of the tissues surrounding the implant zone and the tissue responses to such damage as well as the damage control are termed as inflammatory response. Any such response by the surrounding tissues is marked by reddening or swelling of the zone around damaged tissue. This phenomenon is due to the increased supply of blood to the damaged zone which is promoted by the chemicals (histamine, progladines) released by damaged tissues. The release of these chemicals dilates the blood vessel causing more flow of blood and supply of cells required for repair process. The most prominent among them being the phagocytes cells (originated as white blood cell). The WBC is known for their ability to ingest, digest and remove foreign materials. Later on phagocytes diminish and fibroblasts multiply. This fibroblast helps in producing fibrous tissues such as collagen. During the initial stage of fibroblast generation, collagen fibrils are randomly oriented. Later on they orient themselves and form the frame work of bone. [1.49].

Some studies have shown that before formation or adherence of any oestoblast cells, protein from blood, bone marrow etc gets adsorbed to the implant. This feature controls the subsequent cell adhesion phenomenon. Studies have also shown that chemical composition, surface energy and topographical features of the implant also affects the type and concentration of protein adsorbed. Certain protein such as fibronectin and vitronectin even mediates the attachment, differentiation and growth of required cells on the implant surface [1.50-1.55].

On the other hand, a series of events occur on the tissue side of the implant after formation of carbonated apatite on implant surface. The first such event includes the incorporation of collagen fibrils without the presence of cell, enzymes etc and the bonding of collagen with apatite formed. The next step includes the action of macrophages followed by attachment of stem cells [1.56].

References

1.1 Larry .L.Hench and June Wilson in. “An introduction to Bioceramics, Vol 1”. Advanced Materials Research Centre. University of Florida. Gainesville,FL.

1.2 K. De Groot, C.P.A.T. Klein, J.G.C. Wolke, J.M.A. Blieck-Hogervorst in “Chemistry of calcium phosphate bioceramics”, CRC Handbook of Bioactive Ceramics, . Calcium Phosphate and Hydroxylapatite Ceramics, vol. II, CRC press, Boca Raton, FL, 1990.

1.3 P. Ducheyne, Q. Qiu, “Bioactive ceramics: the effect of surface reactivity on bone formation and bone cell function”, Biomaterials, 20, 2287-2303 (1999).

1.4 M. K. Sinha, D. Basu, P. S. Sen, “Porous hydroxyapatite ceramic and its clinical applications”, InterCeram: International Ceramic Review, 49, 102-104 (2000).

1.5 L. L. Hench, “Bioceramics”, Amer. Ceram. Soc., 7, 1705-1727 (1998).

1.6 S. F. Hulbert. J. C. Bokros, L. L. Hench, “Ceramics in clinical applications :past, present and future”, High Tech ceramics, P. Vincenzini (ed), Elsevier, Amsterdam, 189-213 (1987).

1.7 V. A. Dubok, “Bioceramics — Yesterday, Today, Tomorrow”, Powder Metallurgy and Metal Ceramics, 39, 7-8 (2000).

1.8 M. Ogino, L. L. Hench, “Formation of calcium phosphate films on silicate glasses”, *J. Non-Crystalline Solids*, 38 and 39, 673–678 (1980).

1.9 C. G. Pantano Jr., A. E. Clark Jr., L. L. Hench, “Multilayer corrosion films on glass surfaces”, *J. Am. Ceram. Soc.*, 57, 412–413 (1974).

1.10 M. Vallet-Regii, C. V. Ragel, A. J. Salinas, “Glasses with medical applications”, Eur J Inorg Chem, 6, 1029–42 (2003).

1.11 K. Ohura, T. Nahamura, T. Kokubo, Y. Ebisawa, Y. Kotoura, M. Oka. “Bone-bonding ability of P_2O_5-free CaO–SiO_2 glasses”, J Biomed Mater Res, 25, 357–365 (1991).

1.12 H. Oonishi, L. L. Hench, J. Wilson, F. Sugihara, E. Tsuji, S. Kushitani, H. Iwaki, “Comparative bone growth behaviour in granules of bioceramic materials of various sizes”, *J. Biomed. Mater. Res.*, 44, 31–43 (1999).

1.13 L. L. Hench, J. K. West, “Biological applications of bioactive glasses”, *Life Chem. Rep.*, 13, 187–241 (1996).

1.14 C. A. Miller, T. Kokubo, I . M. Reaney, P. V. Hatton and P. F. James, *J. Biomed. Mater. Res.* 59**,** 473, (2001).

1.15 W. Hoeland "Biocompatible and bioactive glass-ceramic-state of the art and new directions", *Journal Non-Crystalline Solids,*; 219, 192-197 (1997).

1.16 L.L. Hench and O. Anderson, Bioactive glass coatings In: L.L. Hench and J. Wilson, Editors, *An Introduction to Bioceramics*, World Scientific, Singapore (1993), pp. 239–259.

1.17 J.C. Knowles, S. Talat and J.D. Santos, "Sintering effects in a glass reinforced hydroxyapatite", Biomaterials, 17, 1437-1442 (1996).

1.18 T. Kokubo, M. Shigematsu, Y. Nagashima, M. Tashiro, T. Nakamura, T. Yamamuro, S. Higashi, "Apatite- and Wollastonite-containing glass ceramics for prosthetic applications", *Bulletin of the Institute for Chemical Research*, *60*. Kyoto University, pp. 260–268 (1982).

1.19 T. Kokubo, "Bioactive glass ceramics: properties and applications", Bioamtaterials, 12, 155-163 (1991).

1.20 T. Yamamuto, L. L. Hench, J. Wilson, "Bioactive glasses and glass-ceramics: Handbook on bioactive ceramics, vol.1, CRC press, Boca Raton, Florida (1990).

1.21 T. Kokubo, "Surface chemistry of bioactive glass-ceramics", J. Non-cryst. Solids, 120, 138-151(1990).

1.22 Y. M. Kong, H.E. Kim, H. W. Kim "Phase conversion of tricalcium phosphate into Ca-deficient apatite during sintering of hydroxyapatite-tricalcium phosphate biphasic ceramics" J. Biomed. Mater. Res. B, 84B, 334-339 (2008).

1.23 N. Rameshbabu, K. Prasad Rao, T. S. Sampat Kumar, "Accelerated microwave processing of nano crystalline hydroxyapatite", Journal of Materials Science, 40, 6319-6323 (2005).

1.24 S. Suzuki, M. Ogaki, M. Ichiyanagi, M. Ozawa, "Preparation of needle like hydroxyapatite", J. Mater. Sci .Lett., 17, 181-183 (1998).

1.25 Y. M. Kong, D. H. Kim, H. E. Kim, S. J. Heo, J. Y. Koak, "Hydroxyapatite-Based composite for Dental implants: an in Vivo Removal Torque Experiment". 2002, 714-721.

1.26 An Introduction to Bioceramics, L. L. Hench and J. Wilson, chapter 3, page 41-62, World Scientific publishing co, 1999.

1.27 W. Suchanek, M. Yoshimura, Processing and properties of hydroxyapatite-based biomaterials for use as hard tissue replacement implants, J. Mater. Res. 13 (1998) 94–117.

1.28 C. Ergun, T. J. Webster , R. Bizios, R. H. Doremus, “Hydroxyapatite with substituted Mg, Zn, Cd and Y: structure and microstructure”, Journal of Biomedical Materials Research, 59, 305-311 (2002).

1.29 R. A. Young and J. C. Elliot, “Scale Bases for several properties of Apatite”, Archs. Oral. Biol. 11 (1966) 699-707.

1.30 J. E. Barralet, S. Best, W. Bonfield, “Effect of Sintering Parameters on the Density and Microstructure of Carbonate Hydroxyapatite”, J. Mater. Sci:Mats. in Med., 11, 719-24 (2000).

1.31 J. C. Elliot, “The crystallographic structure of dental Enamel and related Apatite” (PhD Thesis, University of London, 1964).

1.32 I.R. Gibson, I. Rehman, S.M. Best, W. Bonfield, “Characterization of the transformation from calcium-deficient apatite to β-tricalcium phosphate”, J. Mater. Sci., Mater Med. 11, 533-539 (2000).

1.33 S. H. Kwon, Y. K. Jun, S. H. Hong, H. E. Kim, “Synthesis and dissolution behaviour of β-TCP and HA/β-TCP composite powders”, J. European. Ceram. Soc., 23, 1039-1045 (2003).

1.34 An Introduction to Bioceramics, L. L. Hench and J. Wilson, chapter 12, page 223-238, World Scientific publishing co, 1999.

1.35 K. De Groot, R. G. T. Geesink, C. P. A. T. Klein, P. Serekian, “Plasma sprayed coatings of hydroxylapatite”, *J. Biomed. Mater. Res.*, 21,1375–1381(1987).

1.36 R. J. Furlong, J. F. Osborn, “Fixation of hip prostheses by hydroxyapatite ceramic coating”, *J. Bone Joint Surg.*, 73B, 741–745 (1991).

1.37 L. Sun, C. C. Berndt, K. A. Gross, A. Kucuk, “Materials fundamentals and clinical performance of plasma-sprayed hydroxyapatite coatings: a review”, *J. Biomed. Mater. Res.*, 58B, 570–592 (2001).

1.38 T. W. Bauer, R. G. T. Geesink, R. Zimmerman, J. T. McMahon, “Hydroxyapatite-coated femoral stems. Histological analysis of components retrieved at autopsy”, *J. Bone Joint Surg.*, 73A, 1439–1452 (1991).

1.39 Bonfield, W., Grynpas, M. D., Tully, A. E., Bowman, J. and Abram, J., Hydroxyapatite reinforced polyethylene: a mechanically compatible implant. *Biomaterials*, 1981, 2, 185–186.

1.40 E. Fernandez, F. X. Gil, M. P. Ginebra, F. C. M. Driessens, J. A. Planell, S. M. Best, "Calcium phosphate bone cements for clinical applications, part I, solution chemistry", *J. Mater. Sci.: Mater. Med.*, 10, 169–176 (1999).

1.41 J.M. Gomez-Vega, E. Saiz, "Bioactive glass coatings with hydroxyapatite and bioglass particles on Ti-based implants 1. Processing", Biomaterials 21 (2000) 105.

1.42 R. Murugan, S. Ramakrishna, "Bioresorbable composites bone paste using polysaccharide based nano hydroxyapatite", Biomaterials 25 (2004) 3829.

1.43 M. Wang, N. H. Ladizesky, K. E. Tanner, I. M. Ward, W. Bonfield, "Hydrostatically extruded HAPEX®", *J. Mater. Sci.*, 35, 1023–1030 (2000).

1.44 S. Nayar , A. Sinha, "Systematic evolution of a porous hydroxyapatite-poly(vinyl alcohol)-gelatin composite", Colloids and Surfaces B: Biointerfaces, 35, 29-32 (2004).

1.45 D. C. Tancred, A. J. Carr, B. A. O. McCormack, "The sintering and mechanical behavior of hydroxyapatite with bioglass additions", Journal of Materials Science: Materials in Medicine, 12**,** 81–93 (2001).

1.46 S. Velayudhan, P. Ramesh, H. K. Varma, K. Friedrich, "Dynamic mechanical properties of hydroxyapatite-ethylene vinyl acetate copolymer composites", Materials Chemistry and Physics, 89, 454-460 (2004).

1.47 D. J. Curran, T. J. Fleming, M.R. Towler, S. Hampshire, "Mechanical properties of hydroxyapatite-zirconia compacts sintered by two different sintering methods", J. Mater Sci.: Mater Med, 21, 1109-1120 (2009).

1.48 S. Nath, K. Biswas, B. Basu, "Phase stability and microstructure development in hydroxyapatite –mullite system", Scripta Materialia, 58, 1054-1057 (2008).

1.49 An Introduction to Bioceramics, L. L. Hench and J. Wilson, Chapter 1, page 1-24, World Scientific publishing co, 1999.

1.50 G. Balasundaran, T. J. Webster, "A prespective on nanophase material for orthopedic implant applications", Journal of Materials Chemistry, 16, 3737-3745 (2006).

1.51 J. M. Schakenraad, in Biomaterial Science, ed. B. D. Ratner, A. S. Hoffman, F. J. Schoen and J. E. Lemons, Academic Press, Inc., San Diego, 1996, page. 140–141.

1.52 K. C. Dee, D. A. Puleo and R. Bizios, in An Introduction to Tissue-Biomaterial Interactions, John Wiley & Sons, Inc., Hoboken, New Jersey, 2002, pp. 37–52.

1.53 T. J. Webster, in Advances in Chemical Engineering, ed. J. Ying, Academic Press Inc., CA, 125–166 (2003).

1.54 T. J. Webster, C. Ergun, R. H. Doremus, R. W. Siegel and R. Bizios, “Specific proteins mediate enhanced osteoblast adhesion on nanophase ceramics”, J. Biomed. Mater. Res., 51, 475-483 (2000).

1.55 S. B. Kennedy, N. R. Washburn, C. G. Simon Jr. and E. J. Amis, “Combinatorial screen of the effect of surface energy on fibronectin-mediated osteoblast adhesion, spreading and proliferation”, Biomaterials, 27, 3817-3824 (2006).

1.56 An Introduction to Bioceramics, L. L. Hench and J. Wilson, Chapter 3, page 41-62, World Scientific publishing co, 1999.

Chapter II

Literature Review

2.1 General Literature on Hydroxyapatite

Among various available calcium phosphate ceramics, Hydroxyapatite (HA) having the general formula $Ca_{10}(PO_4)_6(OH)_2$ is well known synthetic material used for the replacement for human bone on account of its excellent biocompatibility in human body. It shows excellent phase stability above pH 4.3 and as the pH of human blood is around 7.3, HA is a suitable replacement material for applications involving blood contact (Table 2.1). [2.1]

Table 2.1Solubility and pH stability of different phases of calcium phosphates[2.1]

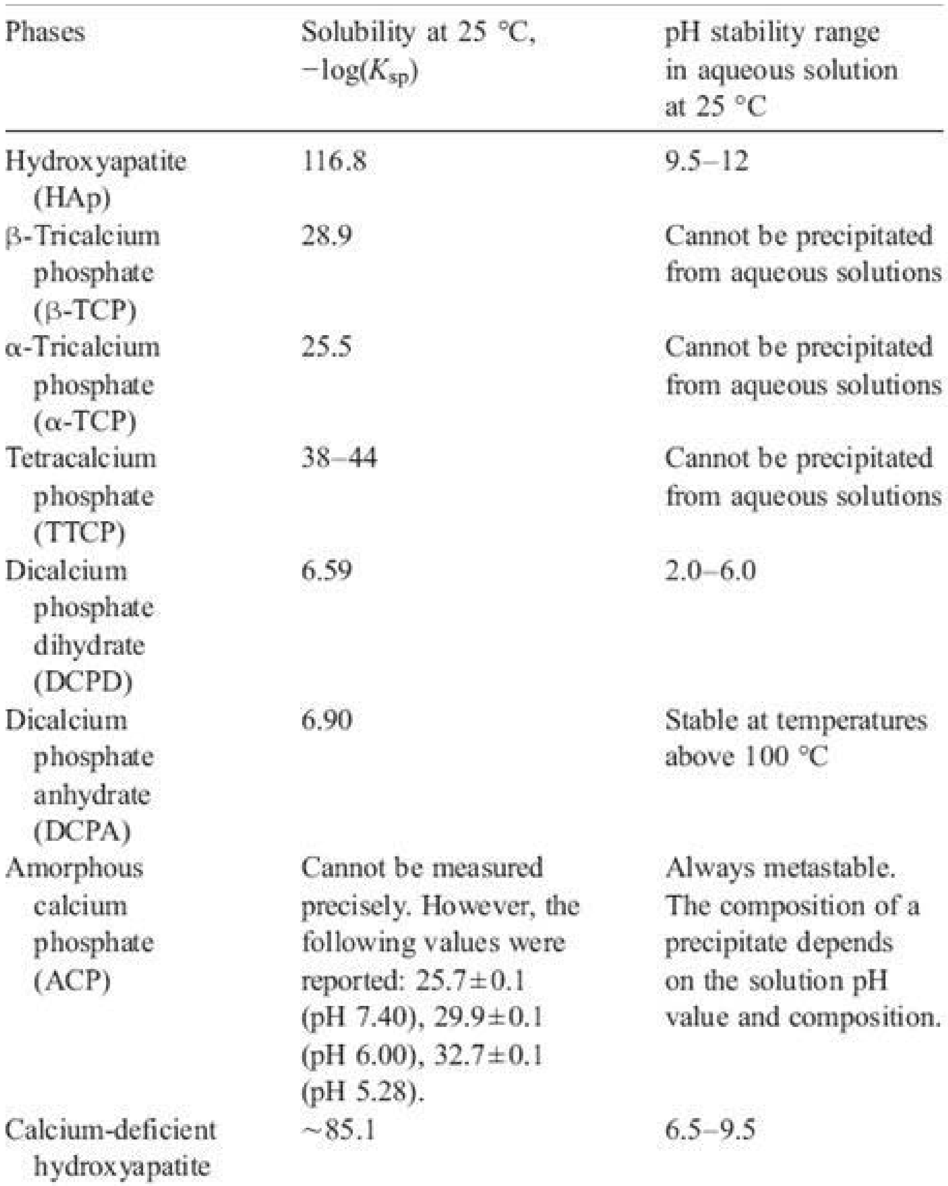

Phases	Solubility at 25 °C, $-\log(K_{sp})$	pH stability range in aqueous solution at 25 °C
Hydroxyapatite (HAp)	116.8	9.5–12
β-Tricalcium phosphate (β-TCP)	28.9	Cannot be precipitated from aqueous solutions
α-Tricalcium phosphate (α-TCP)	25.5	Cannot be precipitated from aqueous solutions
Tetracalcium phosphate (TTCP)	38–44	Cannot be precipitated from aqueous solutions
Dicalcium phosphate dihydrate (DCPD)	6.59	2.0–6.0
Dicalcium phosphate anhydrate (DCPA)	6.90	Stable at temperatures above 100 °C
Amorphous calcium phosphate (ACP)	Cannot be measured precisely. However, the following values were reported: 25.7±0.1 (pH 7.40), 29.9±0.1 (pH 6.00), 32.7±0.1 (pH 5.28).	Always metastable. The composition of a precipitate depends on the solution pH value and composition.
Calcium-deficient hydroxyapatite	~85.1	6.5–9.5

Main factor which separates HA from other calcium phosphate ceramics (viz. $Ca_3(PO_4)_2$ i.e. TCP)) is the higher in vivo stability of the former material with respect to TCP. HA is also an important component of bone and have compositional and structural similarity to that of human bone with ions similar to that found in physiological environment [2.2] .All these above mentioned characteristics of HA makes it a better biocompatible material with an improved bone bonding ability along the bone – implant interface. The bone bonding takes place through the formation of a thin apatite layer as a result of the reaction between HA and body fluid. It has also been noticed that the crystal structure, degree of crystallinity, is largely controlled by pH. Therefore, several studies have been carried out to understand the effect of crystal structure on the physiological behaviour of the apatite in body environment [2.3 - 2.6].

The positions of Ca^{2+}, PO_4^{3-} and $(OH)^-$ ions in the HA the unit cell is shown below:

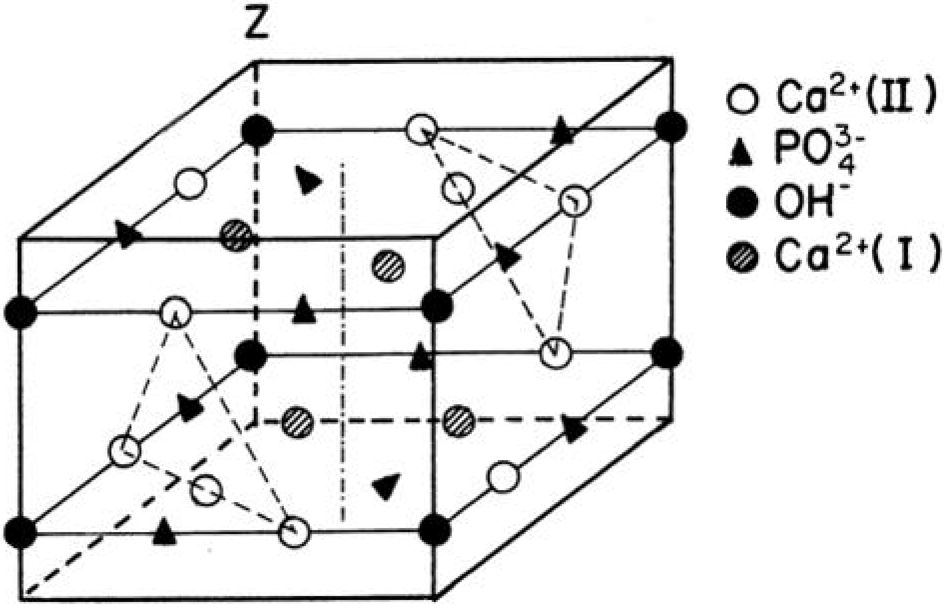

Fig. 2.1 Unit Cell structure of hydroxyapatite (HA)

The unit cell contains ten Ca^{2+} ions. Of these, six Ca^{2+} ion lies completely within the unit cell at Ca(II) position each forming a triangular group of three Ca^{2+} ions at z = 0.25 and z = 0.75 respectively. The Ca^{2+} ions surrounds the $(OH)^-$ groups at the corners of the unit cell at z = 0.25 and z = 0.75. Eight other Ca^{2+} ions lies at the periphery of Ca(I) position and being shared by adjacent unit cells, so that the allocation for each unit cell is four. Similarly the eight $(OH)^-$ ion lying at the edge of each unit cell is being shared by adjacent unit cell to provide a residual of two to each unit cell. Finally, out of the ten $(PO_4)^{3-}$ group two lies completely within the unit cell and eight at the periphery with an overall contributing of six to each unit cell. [2.7 - 2.9].

In the early seventies, a number of studies reported that HA existed in two different crystalline forms viz. monoclinic and hexagonal [2.10, 2.11]. Dense synthetic HA often possesses a hexagonal structure (S.G. $P6_3/m$, 2 formula units per cell) with cell dimensions a=b=9.42 Ǻ and c=6.8 8Ǻ (six- fold symmetry axis with a three-fold helix and a microplane). Ca/P molar ratio for HA is 1.67 and weight ratio of Ca/P is 2.151. The theoretical density of HA is 3.153 $gm.cm^{-1}$.

HA can be synthesized by a number of techniques solid state reactions between CaO and P_2O_5 as well by different chemical routes such as sol gel, mechano-chemical synthesis, microwave irradiation technique etc. Although solid state reaction route is the easiest to understand but it is difficult to control the starting purity of raw materials, and the route usually produces inhomogeneous nonstoichiometric HA which require high temperature for HA formation. On the other hand, chemical synthesis routes produce phase pure HA at a much lower processing temperature. Therefore, it is important to understand and discuss the effect of different processing techniques on the phase stability of HA, its crystallinity, ultimate Ca/P ratio in HA, stoichiometry and the final mechanical property of HA. Therefore, this section makes a thorough review on such aspects of powder processing.

2.2 Processing of HA

2.2.1 Synthesis of HA by Wet Precipitation Route

Guzman et.al [2.12] synthesized stoichiometric HA by two different routes: wet precipitation method and sol gel process. In the former, two different types of wet precipitation routes were used. The first precipitation route used $Ca(OH)_2$ and H_3PO_4 as precursors and the second precipitation route used $Ca(NO_3)_2$ and $(NH_4)_2HPO_4$ as the starting material. The precipitates from precipitation route were calcined at $850^{O}C$ and

1200^{O}C respectively. The first precipitation process gave a more crystalline HA compared to the second route. The sol gel process though provided a near stoichiometric HA at Ca/P ratio 1.67 compared to precipitate one, but is less economical compared to precipitation route. [2.13 - 2.15].

Karina et.al [2.17] prepared HA by two wet-chemical precipitation methods A and B [2.16]. In method A, $Ca(NO_3)_2.4H_2O$ and $(NH_4)_2HPO_4$ were the only ingredients used whereas method B included small amount of pyrophosphate ions along with magnesium and carbonate ions. The latter ions were added in an effort to retain the amorphous state of the calcium phosphates. The obtained precipitates were washed, dried and sintered at 900^{o}C for 1 hour. Further development involved the mixing of 1gm of powder A with 2 gm of powder B (BIO) followed by compaction and sintering. Although the XRD pattern of all these powder corresponded to that of HA but sample A showed a higher compressive strength (6-9 MPa), B sample strength was < 1MPa and the mixture (BIO) showed the highest compressive strength of 26-30 MPa after sintering. The Ca/P ratio of sample B and BIO was higher than 1.67. The presence of large amount of CaO decreased the strength value as in case of B. However, when CaO was present in trace amount or in the form of CaO based additives the mechanical properties were substantially improved. Besides, sintering additives (~ 2.5 wt%) did not hamper the phases of pure HA.

Jillavenkatesa et.al [2.18] synthesized hydroxyapatite by sol-gel route using calcium acetate and triethyl phosphate as the calcium and phosphate source. Various organic alcohols were also added to study their effect on the reaction. It was observed that the slow rate of hydrolysis of phosphate could be accelerated by using organic alcohols. However, it may also be noted that the formation of calcium oxide (in the temperature range 780 – 900^{o}C) due to the decomposition of calcium carbonate had an adverse effect on the stoichiometry and phase of synthesized HA. The powders were treated with 0.01 HCl along with high temperature curing (>900^{O}C) for improving the hydroxyapatite yield as well as to remove carbonates and residual CaO present in the system.

2.2.2 Agglomeration of Hydroxyapatite Particles Prepared by Precipitation Route

Saeri et.al [2.19] prepared stoichiometric HA by wet precipitation technique using orthophosphoric acid and calcium hydroxyapatite. The investigation was focused to study the effect of reaction time and calcination temperature on the morphology of the synthesized particle by using field emission microscopy. The result revealed that although the precipitation process could be assumed to be an efficient one compared to others as the precipitation continues during 'ageing time' but the precipitated particles are well agglomerated as seen by the FE-SEM micrographs. The agglomeration tendency of the precipitates largely depended on aging temperature as well as ripening method and time.

I. Mobasherpour et.al [2.20] used TEM and SEM to determine the particle size, morphology, and agglomeration state of HA powder synthesized by precipitation route using transmission electron microscopy and scanning electron microscopy. The SEM microstructure of the powder calcined at 1200^{O}C showed the presence of large agglomerates made up of fine particles formed during drying. However, the TEM micrograph of the powder showed particle size in the range 40-50 nm. The processing route had caused a remarkable improvement in the crystallinity of the powder [2.21].

2.2.3 Process modification for ensuring phase stability of Hydroxyapatite Prepared by Precipitation Route

Choi et.al [2.22] synthesized chemical enriched HA by aqueous precipitation route using $CaCl_2$ and Na_3PO_4 as the calcium and phosphorous source respectively. NaOH was added to ensure completion of the precipitation reaction at room temperature. The XRD pattern showed that the HA synthesized by the addition of stoichiometric amount of NaOH maintained the phase stability till 1200^{o}C as compared to the other batch which were prepared from non stoichiometric amount of NaOH. The change of pH with time was pronounced in case of the batch not containing NaOH. The ICP-OES (Inductively coupled plasma optical emission spectroscopy) result showed that with the addition of stoichiometric amount of NaOH, the ((Ca+Na)/P) ratio became 1.738 which made the HA more stable.

Zhengwen et.al [2.23] studied the influence of microwave irradiation method on the phase stability of precipitated HA powder. The work focused on the effect of microwave irradiation time and power on the phase stability of HA. The results showed that the thermal stability of HA increased with an increase in microwave radiation power and time along with ageing time. The microwave energy hastened the movement of substance molecule in the solution, thereby improving the reaction rate with an attenuation of high Ca/P molar ratio in short time.

2.2.4 Preparation of Carbonated Apatite

Yanbao et.al [2.24] developed carbonate substituted amorphous HA using ammonium carbonate($(NH_4)_2CO_3$) and polyethylene glycol along with calcium nitrate hydrate ($(CaNO_3)_2.4H_2O$) and ammonium hydrogen phosphate($(NH_4)_2HPO_4$). The chemical composition of carbonated HA being closer to that of bone mineral was a subject of interest. The carbonated HA showed better biological properties and sinterability than pure HA. The synthesized carbonated amorphous hydroxyapatite (Ca/P = 1.73) had nanosized particles and were highly agglomerated. The primary nanosized particle cluster on calcination at $800^{O}C$ was converted to carbonated HA with the primary particle size of 50nm. The growth of primary particles occurred by the fusion of cabonated crystalline hydroxyapatite.

2.2.5 Preparation of Hydroxyapatite by Biomimetic Route

A. Cuneyt Tas [2.25] introduced a novel biomimetic synthesis process to produce Ca-Hydroxyapatite. He used synthetic body fluid (SBF) solution instead of pure water at pH 7.4 and temperature $37^{o}C$. Calcium nitrate and di-ammonium hydrogen phosphate were used as the starting material. The obtained powder was phase stable till $1600^{o}C$ without any decomposition of HA to β -TCP. This result was definitely different with that of others [2.26 - 2.28]. Although, trace amount of organic ions were also incorporated into the HA structure from the SBF solution, it did not affect the sintered density and the sintered samples had a relative density of ~ 96% on sintering at $1200^{O}C$ for 6 hrs.

Above reviews suggest the utility of wet precipitation route in producing fine particles of crystalline HA with improved mechanical properties. However the drawbacks of this route, such as the agglomeration tendency of the particles, low stoichiometry (due to localized precipitation) adversely affects the densification behavior and phase stability of the processed powders. On the other hand, routes such as sol-gel though produces a stoichiometric HA but is poorly crystallized which result in poor mechanical property of such materials. Few papers also suggest the usefulness of microwave irradiation in restoring the phase stability of precipitated powder. Thus it could be concluded that wet precipitation technique with some process modification could be adopted as an effective and cheaper route for synthesis of HA powder

2.3 Effect of Processing Parameters on Different Properties of Hydroxyapatite

2.3.1 Effect of Processing Temperature, Reactant Concentration and Ca/P ratio on the Powder Morphology and Mechanical Properties of Sintered Hydroxyapatite

Kothapalli et.al [2.29] systematically observed the effect of reactant concentration and temperature on the morphology, sintering behaviour and mechanical strength of the HA prepared by wet precipitation method. Aqueous solutions (pH 12) of calcium nitrate and ammonium hydrogen ortho phosphate were considered as the starting material. Three different precursor concentrations (0.5, 1, 2 gm/dL) were used and for each concentration three different reaction temperature (25^{O}C, 70^{O}C and 100^{O}C) were used. Results showed that at a constant reactant concentration, particle size decreased with a decrease in reaction temperature. However, lower reaction temperature produced more agglomerated powders due to the increased surface area of the particle at lower reaction temperature. However, the results could not explain the effect of concentration on the agglomerate size but it was observed that the precursor concentration had a certain effect on the morphology of the obtained particles. The aspect ratio (c/a ratio) of the processed hydroxyapatite particles increased on increasing the reactant concentration while holding the reaction temperature constant. The biaxial flexural strength of sintered hydroxyapatite increased proportionately with the reaction temperature at a constant precursor concentration. However, at a reaction concentration of 2 gm/ml and processing temperature 100^{O}C the density as well as the strength was lowest due to severe decomposition of hydroxyapatite.

Varma et. al [2.30] had processed HA at two different synthesis temperature [viz 0^{O}C(sample A) and 80^{O}C(sample B)] and studied their relative effect on the particle size and morphology of the obtained precipitate. The 0^{O}C samples was spherical having 30-50 nm crystallites while 80^{o}C powder had acicular shape with size > 100nm. The microstructural analysis showed that sample A had a uniform microstructure (grain size ~ 250nm) and minimum intergranular porosity. The maximum microhardness for sample A was 6 GPa.

Yun et.al [2.31] prepared hydroxyapatite using novel ultrasonic precipitation method and studied the effect of [Ca^{2+}], reaction temperature, Ca/P ratio and ultrasonic power on the crystallinity and morphology of hydroxyapatite nanoparticles. The [Ca^{2+}], Ca/P molar ratio and temperature of the solutions were varied between 0.01- 0.1 mol/L, 1.2-2.5 and 293-353K respectively. XRD revealed that the crystallinity improved with the increase in [Ca^{2+}]. HA phase also remained stable for the [Ca^{2+}] range 0.01- 0.1 mol/L. However, the stability of HA deteriorated when [Ca^{2+}] was further increased to 0.2 mol/L. Particle size was smaller at lower [Ca^{2+}] and at higher ultrasonic power (300W), the particle morphology also changed from acicular to spherical. Finally, the particle size decreased from 15 nm to 10 nm when the reaction temperature was increased from 315K-355K.

2.3.2 Effect of Process Modification and Sintering Temperature on the Density and Mechanical Property of Sintered Hydroxyapatite

Thangamani et.al [2.32] studied the effect of powder processing and sintering temperature on the densification, morphology and mechanical properties of the HA ceramics which were sintered between 1000 – 1400^{o}C for 3hrs. The as precipitated HA powders were calcined at two different temperatures of 800^{o}C and 1000^{o}C for 3hrs. A part of the calcined powders were subjected to planetary milling in propanol medium followed by uniaxial pressing at 65MPa. Calcination at 800^{o}C not only reduced the particle size but also narrowed the particle size distribution. It was observed that low temperature calcination (800^{O}C) followed by milling of as prepared hydroxyapatite produced a higher density (97%) body at 1100^{O}C. The fracture toughness value of such body was 0.88 MPa.m$^{1/2}$ and hardness was 6.3 GPa.

2.3.3 Effect of Calcination Temperature on the Sinterability and Mechanical Properties of Hydroxyapatite

Juang et.al [2.33] studied the effect of calcination temperature on the sintering behaviour and strength of hydroxyapatite. The hydroxyapatite were calcined at four different temperature of 700 ,800, 900, 1000^{o}C for 4 hours followed by pressure less sintering in the range of 1200-1400^{O}C. The calcination step changed the particle size distribution from trimodal to monomodal and the distribution also became narrower at higher calcination temperature. At the same time, the mean particle size of 1000^{O}C calcined powder increased from 0.97μm to 4.19 μm post calcination. The results indicated that the temperature accelerated the conversion of finer particle to coarser one. The four point bending strength as a function of sintering temperature showed that the compacts prepared from 900^{O}C calcined powder and sintered at 1250^{o}C.had highest strength (55MPa).

2.3.4 Phase Stability of Hydroxyapatite

Tampeiri et.al [2.34] had studied the improvement of the thermal stability of the synthetically prepared HA by wet precipitation technique. The authors added various amount of dry $Ca(OH)_2$ powder ranging from 0.7-7wt% to the HA powders of two different crystallinity (A = 70% and B = 20%) which were prepared by varying the reaction temperature between 35-95^{o}C.The result showed that the Ca/P ratio as calculated by ICP analysis is 1.601 for powder A and 1.565 for powder B. This showed that an higher initial crystallinity produced a phase stabile final product. It was also observed that the addition of only 1.4 wt% $Ca(OH)_2$ to A-type powder could stabilize the HA till 1400^{O}C.On the other hand, powder B did not decompose till 1350^{O}C when 2.8 wt% of $Ca(OH)_2$ was added. Calculation also showed that these were the requisite amount for fixing the accurate HA stoichiometry.

Seckler et.al [2.35] made a comprehensive study on the effect of reagent addition time, temperature, NH_4OH concentration, pH and carbonate ion on the stoichiometry and crystallinity of HA. The reactants used were 1 M ammonium acetate solution, 0.1 M calcium nitrate solution, 0.0543 M diammonium phosphate solution and 0.1 M to 7.7 M ammonium hydroxide solution. Results showed that the addition of low concentration NH_4OH (0.1M) gives higher crystillinity. A higher processing temperature of 90^{0}C gives a stoichiometric HA while HA synthesized at room temperature showed β-TCP along with HA as the major phases. A longer addition time ($\geq$ 60 min) not only contributes a HA of higher crystallinity but also take cares of its stoichiometry. A higher pH (~10) and high carbonate ion incorporation also produces a crystalline HA. Moreover, the analysis indicated that stoichiometric and crystalline HA can be produced at low super saturation value.

Zhang et.al [2.36] studied the effect of drying conditions on the final particle size and microstructure of the synthesized HA. The reacted slurry of $CaHPO_4.2H_2O$ and $CaCO_3$ (by ball milling) was dried at five different temperatures for 3, 7, 10, 14, 18 and 21 days followed by calcination at 720^oC for 8hr. However, the result signifies there is no such tailoring effect of drying temperature on the final property of the product. Whereas, the XRD of the powder dried at 60^0C and calcined at 720^0C/8hr shows all peaks corresponding to HA. Particle size distribution of the powder dried at 60^oC for 3, 10, 18 days shows that distribution narrows down with the increase in drying time. A similar effect was also observed in case of the calcined powder. The specific surface area of the as dried powder is very high compared to that of calcined one. Additionally, the surface area for the as dried powder shows a decreasing inclination with increase in drying time. But the TEM photo graphs of the calcined powder shows no significant effect of drying time on the final morphology of the powder.

Prakash et.al [2.37] also has studied the effect of super saturation level on the particle morphology and particle size. Some others authors have reported that the synthesis temperature along with the nature of initial precursor plays a crucial role in defining the morphology of the obtained precipitate [2.38]. It was concluded that temperature has a lesser effect on HA particle morphology as compared to the effect produced by varying super saturation level of the reactant. The results indicated that the addition of a small amount of acetic acid to $Ca(OH)_2$ solution at 100^0C increases the solubility of $Ca(OH)_2$. There by increasing Ca^{2+} concentration in solution. As a result of Ca^{2+} concentration increase the aspect ratio of spheroid HA particle increased dramatically.

In a study by Murray et.al [2.39] the particle agglomeration tendency for wet precipitation and sol-gel route hydroxyapatite powder was correlated with the sinterability and final mechanical properties. The authors introduced an emulsion refinement step for avoiding hard agglomerate formation. This resulted in an improvement in the green density as well as the final sintered density as compared to non emulsion refined powder. The enhanced sinterability of emulsion refined HA powder resulted in higher fracture strength (170MPa) as compared to the conventional powder (70MPa).

Wang et.al [2.40] synthesized HA nanorods of controlled dimensions by precipitation route using organic modifier such as polyethylene glycol, Tween 20, trisodium citrate and D - sorbitol. It was observed polyethylene glycol addition was beneficial for the formation of high aspect ratio HA nano rod. On the other hand linear structured D–sorbitol leads to the formation of long HA nano rod at low synthesis temperature. The addition of both Tween 20 and trisodium citrate were good in making small size HA nano rod.

2.3.5 Effect of pH, Stirring Seed its Duration and Sintering Atmosphere on the Stoichiometry and Phase Stability of Sintered Hydroxyapatite.

Afsar et.al [2.41] has studied the effect of important processing parameters such as atmosphere control, pH, solution stirring speed and time on the final stoichiometry and phase stability of HA. Due to the receptive nature of HA for CO_2 present in air, $(CO_3)^{2-}$ can easily substitute the hydroxyls or phosphates sites of HA to form A or B type of carbonated HA respectively. In order to avoid the CO_2 contamination, an inert atmosphere with CO_2 absorber was used. A high stirring speed (2000 rpm) along with prolonged stirring time helped in decreasing the intensity of free CaO peak.

2.4 Sintering of Hydroxyapatite and Hydroxyapatite Based Composites

2.4.1 Sintering of Hydroxyapatite

Best et.al [2.42] investigated the sintering and mechanical behaviour of three different powders (A, B, C) having different physical properties. Powder A had non uniform, acicular shaped particles and powder B consisted of uniform spheroid particles; which at higher magnification showed it to be agglomerates of finer crystallites of around 0.1mm, Powder C were angular fragments composed of spheroid crystallites of 0.5μm. Surface area of the powders A, B, C were 18, 2, 63 m^2/gm respectively. The particle size distribution of powder A and B were nearly monomodal, although the distribution was narrower for A. Powder C showed wider particle size distribution of biomodal type. The density graph showed that while powder A and C attained the maximum density of 97% and 98.8% of theoretical at 1280^{o}C, powder B could not attain the same even at

1300^oC.The density variation reflected in the hardness which was 680 and 880Hv for A and C powder with $50H_V$ for B.

Fanovich et.al [2.43] studied the consequence of thermal pretreatment, sintering temperature and effect of additives (Li^+ and Mg^{2+}) on the microstructure and sintering behaviour of HA having different Ca/P ratio (1.51 and 1.77). Results revealed that HA with Ca/P 1.51 not only partially transformed to β-$Ca_3(PO_4)_2$ but also shifted the onset of shrinkage to a higher temperature, thereby affecting the final sintered density. Similarly, when HA was preheated to 500^OC prior to sintering at 1100^0C; then HA having Ca/P = 1.77 provided a dense sample. Among Li^+ and Mg^{2+} addition, it was observed that an optimal addition of Li^+ ensured liquid phase sintering by the formation of Li-phosphate and Ca-phosphate glasses. The presence of these glassy phases reduced β-TCP content in HA samples having Ca/P = 1.51. The addition of Mg^{2+} however, only inhibited the grain growth of HA.

Ramesh et.al [2.44] studied the effect of sintering temperature, sintering atmosphere and sintered grain size on the mechanical property and phase purity of the sintered HA. In the study, HA was synthesized by wet chemical route followed by sintering over a range of temperature (900^0C to 1300^0C). The XRD results of the sintered compacts showed that phase pure HA was stable till 1300^0C. The greater stability of HA phase was attributed to presence of moisture which prevented dehydroxylation of HA lattice at high temperature. The presence of higher moisture also helped to attain 97% density by 1000^0C which increased to > 98% at 1300^0C. The grain size increased gradually till 1150^0C followed by an exponential increase beyond that temperature. However, higher grain size had adverse effect on the hardness and fracture toughness.

2.4.2 Reinforcement by Hydroxyapatite Whiskers

Suchanek et.al [2.45] investigated the reinforcement of HA by the incorporation of HA ≤ 30% whiskers. The composite structure was fabricated by pressureless sintering, hot pressing or hot isostatic pressing. Highest fracture toughness (2 $MPam^{1/2}$) was obtained for HAp 20% -30% HAp whisker sample fabricated by hot isostatic pressing which was twice that obtained for unreinforced. Crack deflection by the whiskers was considered to be the toughening mechanism. HAp - 20% HA whisker composites sintered by hot pressing shows the maximum toughness value of 1.4 $MPam^{1/2}$ at 1000^0C with the density showing a decreasing trend with an increase in whisker content. However, a slightly non stoichiometric Ca/P molar ratio of HA whiskers (1.66) with respect to that of pure HA (1.67) affects the phase purity of the composites with the formation of β-TCP.

2.4.3 Effect of Grain Size and Porosity on Mechanical Property of Hydroxyapatite:

Dense HA ceramic was prepared by Veljovic et.al [2.46] using a novel hot pressing technique. The samples were cold isopressed into green shapes and hot pressed at 20 MPa at 900^0C, 950^0C and 1000^0C. The control samples were pressureless sintered between 1000^OC to 1200^OC in air. The air sintered samples had a porous microstructure with mean grain size 3 μm. On the other hand, the hot pressed samples (1000^0C for 1 hr) showed a dense microstructure with an average grain size of 140 nm, which further decreased to 50 nm on decreasing the hot pressing temperature to 950^0C. The maximum indentation fracture toughness and the micro hardness was 1.52 $MPam^{1/2}$ and 4.3 GPa respectively for 950^0C hot pressed composite.

Ranito et.al [2.47] has also studied the grain size and residual porosity effect on the mechanical properties of HA. The results showed that it was difficult to sinter HA compact above 1300^0C without causing any decomposition with β-$Ca_3(PO_4)_2$. An increase in sintering temperature from 1300^0C to 1325^0C caused a sharp increase in grain size. However, exaggerated grain growth lowered the four point bending strength and indentation fracture toughness.

2.4.4 Effect of Sintering Additives on the Phase, Density and Mechanical Property of Hydroxyapatite:

Knowles et.al [2.48] studied the use of glass (31mol% Na_2O, 24 mol% CaO and 45 mol% P_2O_5) as a sintering aid for improving the mechanical properties of HA. 2 and 4 wt% of glass was added to the powder compact and sintered at four different temperatures (1200^0C, 1250^0C, 1300^0C and 1350^0C). Only, a small amount of β-TCP was found in all the glass added HA system sintered at 1200 and 1250^0C, but sintering at 1300 and 1350^0C showed presence of both β and α - TCP. The amount of TCP (β and α) was maximum in case of HA reinforced with 4 wt% of glass. Both 2 and 4 wt % glass reinforced HA showed significant improvement in flexural strength as compared to that of pure HA, with 2 wt% addition showing a steady improvement with temperature. However, in HA with 4 wt% glass addition, a sharp decrease in flexural strength was noted above $1300^{O}C$ due to the large volume of liquid phase formed above $1300^{O}C$.

Suchanek et.al [2.49] studied the effect of various sintering additives on the phase, densification and grain growth of HA. Among the various known sintering additives K_2CO_3, Na_2CO_3 and KCl along with a few sodium phosphates was found to improve the densification of HA significantly. However, excluding some sodium phosphates and KCl all other additives lead to the formation of undesirable phases such as CaO and β-TCP.

The effect of ternary glassy sintering aid on the densification behaviour and phase stability of HA was studied by Kalita et.al [2.50]. In their study, 2.5 wt% of CaO-P_2O_5-Na_2O based additives were used. Among the five different additives that were tried, the one with CaO: P_2O_5: Na_2O :: 3:3:4 showed the highest microhardness of 4.6 GPa and with 2.5 wt% of CaO addition, the maximum compressive strength of 220 MPa on sintering at $1300^{O}C$. These additions did not have any adverse effect on the phase stability of HA. Microstructural analysis showed that except for HA-2.5 wt% CaO composition, liquid phase sintering was achieved with all other sintering additives. The in vitro study of HA compositions (containing 2.5 wt% additives) with human osetoblast cell line showed an enhanced cell proliferation with respect to pure HA.

2.4.5 Effect of Sodium Free Glass Reinforcement on the Mechanical Properties of Hydroxyapatite

A study by Oktar et.al [2.51] showed that sodium free glasses could be better accommodated by HA structure. HA-10 wt% CaO-P_2O_5 binary glass (45.5 wt% P_2O_5, 54.5 wt% CaO) composite sintered at $1200^{O}C$ showed higher strength (67 MPa) along with high hardness (285 H_V) than that of HA-10 wt% ternary glass (45 wt% P_2O_5, 28 wt% CaO, 27 wt% Na_2O) composite. However, the compressive strength of HA - binary glass composite decreased on increasing the sintering temperature from $1200^{0}C$ to $1300^{0}C$.

2.5 Hydroxyapatite - High ZrO_2 Composite

The application of HA as a bone replacement had been limited mainly to the non-load bearing components, e.g., small unloaded or low loaded implants, coating on metal implants and as bioactive filler as a powder or as a second phase in polymer based composites [2.52. 2.53]. Owing to its low strength and toughness, a wide range of ceramic materials have been tried as reinforcement for HA, e.g. Al_2O_3, PSZ, TiO_2, Mullite etc. Of them PSZ has the potential to be a very good reinforcement for HA on account of stress induced transformation of tetragonal (t) – monoclinic (m) zirconia. A number of approaches have been tried to prepare HA-ZrO_2 composites containing higher fraction of ZrO_2 (20-40 vol%) [2.54]. Usually, the decomposition of HA to TCP takes place at high temperature (1200 -1300^{o}C) associated with the removal of $(OH)^-$ from the HA structure which disturbs HA's stoichiometry. The decomposition temperature is lowered (1000^{0}C-1050^{0}C) in the presence of ZrO_2 because of diffusion of CaO to ZrO_2, thus making HA Ca-deficient (CD-HA) and promoting decomposition [2.55]. The reaction between HA and ZrO_2 at the sintering temperature (> 1000^{O}C) not only reduced HA amount but also caused a reduction of t-ZrO_2 content due to the formation of $CaZrO_3$ phase. The presence of CD-HA, TCP, $CaZrO_3$ phases slowed down the densification of composite. The end product was a porous body having lower strength and toughness along with high resorbability of the composite. In presence of ZrO_2, the loss of $(OH)^-$ from HA structure starts around 950^{O}C. In order to control the decomposition reactions, the dehydroxylation of HA around 950^{O}C need to be suppressed. This could be possible either by lowering the sintering temperature, shortening the high temperature processing time or by sintering in a humid atmosphere. Parameters like type of zirconia (stabilized/unstabilised), volume fraction of ZrO_2 and sintering schedule will be the key monitoring parameters for achieving a HA - ZrO_2 composites with greater phase stability and improved mechanical properties. It is well known that fluorapatite has a higher thermal stability than HA without sacrificing its biocompatibility [2.56]. Thus, use of additives such as CaF_2, MgF_2 etc may be providing a greater stability against phase decomposition of HA and HA based systems.

2.5.1 Effect of Fluoride Additives on the Phase and Mechanical Properties of Sintered HA-TZP Composites

Kim et.al [2.57] studied the effect of CaF_2 addition (≤ 10 vol%) on the phase stability and densification behaviour of HA-ZrO_2 composite containing up to 40 vol% ZrO_2. The addition of a small amount (< 5 vol%) of CaF_2 not only improved the thermal stability of HA but also made a significant improvement in low temperature densification of the composite. This improvement in densification was due to the low decomposition of HA to TCP or TetCP, due to the substitution of F^- for OH^- in the HA structure. Although, the addition of CaF_2 suppressed the decomposition of HA to β-TCP to a large extent but $CaZrO_3$ was observed though HA decomposition was not observed. The highest flexural strength (180 MPa) and fracture toughness of (2.3 $MPam^{1/2}$) was observed for the batch containing 40 vol % ZrO_2 sintered at 1350^oC. The cell proliferation test conducted on HA-ZrO_2 system (containing CaF_2) using human osteoblast like cell (MG63) showed a similar response to that of HA after proliferation for 7 days.

In a similar study, Kim et.al [2.58] found that in HA-20 & 40 vol% ZrO_2, the replacement of CaF_2 by MgF_2 (≤ 10 vol%) showed improvement in the HA phase stability with minimal decomposition of HA to TCP up to 1400^oC. The microstructure of sintered (1400^OC) HA – 20 vol% TZP (containing 5 vol% MgF_2) showed greater phase stability, higher density and larger grain size. However, with 10 vol% MgF_2 addition, large pores developed due to the melting of residual MgF_2 which did not enter the HA structure. Highest flexural strength (170 MPa) and hardness (7 GPa) was noticed in 1300^oC sintered HA - 40% vol% TZP composites containing 2.5 vol% MgF_2.

2.5.2 Preparation of Hydroxyapatite – High ZrO_2 Composites by Solid State Route

Rao et.al [2.59] synthesized HA - zirconia composite by solid state mixing of TCP, $Ca(OH)_2$ and m-ZrO_2 followed by heat treatment at 1000^oC for 8 hours. The ZrO_2 amount was 10, 20 and 30 wt% and the TCP to $Ca(OH)_2$ molar ratio was 3:2. The XRD pattern of the sintered composite containing 10 and 20 wt% of m-ZrO_2 addition showed retention of reasonable amount of t-ZrO_2 due to the stabilizing effect of CaO (from HA). However, this transformed the HA to Ca deficient HA which subsequently decomposed partially to β-TCP. On increasing the amount of m-ZrO_2, the decomposition of HA further increased and more m-ZrO_2 phase was retained due to the unavailability of CaO. However, an increase in sintering temperature above 1100°C resulted in the decomposition of HA to β-TCP along with formation of t-ZrO_2 and $CaZrO_3$.

2.5.3 Effect of High ZrO_2 Addition on the Microstructure and Mechanical Properties of Sintered Hydroxyapatite-ZrO_2 Composites

Silva et.al [2.60] synthesized HA - ZrO_2 (calcia stabilized) composite containing 40 and 60 vol% ZrO_2 by coprecipitation route using $Ca(NO_3)_2$ and $(NH_4)_2HPO_4$ as the starting precursor for HA. The XRD patterns of both the compositions showed that HA was present in very small amount along with high fraction of $Ca_{0.15}\,Zr_{0.85}\,O_{1.85}$ and significant amount of t and m-ZrO_2. A model was developed and proposed describing the substitution of Ca^{2+} by Zr^{4+} in HA structure.

Another work by Silva et.al [2.61] investigated the effect of 40 and 60 vol% ZrO_2 additions on the final microstructure and mechanical properties of HA-ZrO_2 composite. Z4H6 batch registered the highest density (89%) on sintering at 1400°C. On the other hand, Z6H4 had 91% theoretical density after sintering at 1300°C. The grain size increased sharply above 1300°C. However, the 2% variation in density did not affect the strength and hardness and both for Z4H6 and Z6H4 composite, the highest strength and hardness was recorded in 1300°C sintered samples. Sintering at 1400°C and 1500°C caused both strength and hardness to decrease due to the formation of micro cracks.

2.5.4 Effect of Moist Environment on the Phase Stability of HA-High ZrO_2 Composite

Delgado et.al [2.62] prepared HA-20 wt% Mg-PSZ composite by pressure less sintering at 1250°C/4 hours in wet oxygen atmosphere. The composite sintered in moist atmosphere had zero decomposition whereas the one sintered in air transformed to β-TCP and $CaZrO_3$. The presence of moisture in the sintering environment reversed the chemical decomposition process thus, stabilizing the HA phase. The instability/stability of hydroxyapatite-TZP phase determined to a large extent the mechanical properties of the composite, particularly bending strength and fracture toughness. A large difference in α value between HA, TZP and other phases generated microcracks which increased toughness through microcrack toughening mechanism.

Thus, the major obstacles in the processing of HA-ZrO_2 composites were the control of HA-ZrO_2 decomposition as well as the retention of ZrO_2 in the tetragonal phase. It appeared that both the difficulties could be overcome if the composite could be sintered at low temperatures (< 1000^0C). A lower sintering temperature will not only result in finer grain size and higher fraction of retained tetragonal ZrO_2 but also will prevent the decomposition of HA to TCP. Many techniques have been adopted for preparing dense HA-ZrO_2 composites at lower sintering temperatures. Some of these techniques are hot pressing/hot isostatic pressing and spark plasma sintering.

2.5.5 Effect of Novel Processing Technique on the Phase and Mechanical Properties of Sintered Hydroxyapatite-ZrO_2 Composite

Kimta et.al [2.63] produced a dense HA- ZrO_2 composite containing 20 wt% of ZrO_2 by hot pressing method at four different temperatures 1150^oC, 1200^oC, 1250^oC and 1300^oC respectively. ZrO_2 powder with three different morphology (fine, coarse and needle like) and phases (t or m-ZrO_2) were used as the reinforcement phase. The effect of reinforcement on the final phase and mechanical property of the composite were studied. The XRD pattern showed no substantial effect of ZrO_2 morphology on the ultimate phase of the composite. An increase in bending strength and fracture toughness was observed for the composite with respect to monophasic HA.

Takagi et.al [2.64] prepared HA-TZP composite containing 10.1, 16.3 and 26.8 wt% TZP by hot isostatic pressing between 800^OC to 1150^OC at 100 MPa pressure. A fully dense compact was obtained in all the cases at 1100^OC. XRD pattern of 26.8 wt% TZP content batch had only HA and tetragonal zirconia below 1150^OC and TCP and cubic zirconia above that temperature. Till 1100^OC, both toughness and hardness of the composite increased with an increase in sintering temperature. The bending strength, toughness and hardness of fully dense composite showed an increasing trend with increasing TZP content. On the other hand, the toughness of monophasic HA was independent of sintering temperature.

. Therefore, it can be concluded that in order to minimize the reaction between HA and TZP and thereby suppress the formation of TCP, the sintering temperature of HA-TZP composite needs to be lowered and/or the sintering time needs to be shortened. However, lowering the sintering temperature or shortening the processing time sometimes may halt the densification at a premature stage. Therefore, although a lower sintering temperature is desirable, it needs to be ensured that densification is complete. The spark plasma sintering technique is another novel densification technique which though has similarity to the conventional hot pressing promotes sintering by charge discharge between particle in addition to heat and pressure.

Miao et.al [2.65] synthesized HA – 40 wt% 3YSZ composite by spark plasma sintering. The maximum density (93% of theoretical) was obtained at $1200^{O}C$ with slight decomposition of HA to α-TCP. Small microcracks were observed along the HA/HA and the HA/YSZ grain boundaries induced by the differential thermal expansion coefficient of HA ($\sim 16.9 \times 10^{-6}\ {}^{O}C^{-1}$) and YSZ ($\sim 10 \times 10^{-6}\ {}^{O}C^{-1}$). The Knoop microhardness, Young's modulus and bending strength of the sintered composite ($1200^{O}C$) were 9 GPa, 160 GPa and 200 MPa respectively.

In another interesting work, Shen et.al [2.66] studied HA-ZrO_2 composite containing varying volume % of 3Y-TZP (90, 80, 70, 60 and 50) respectively were sintered by a novel spark plasma sintering technique at $1150^{O}C$ for 5 minutes at a pressure of 50 MPa. A fully dense HA-TZP composite was obtained without any decomposition of HA to TCP along with complete retention of tetragonal zirconia. The decomposition reaction zone proceeded from surface to interior via surface diffusion mechanism and therefore, the decomposition of HA to TCP was avoided by suppressing the diffusion of water from the interior to the surface through the formation of closed frame work by zirconia matrix. It was observed that the presence of nanostructured ZrO_2, improved the flexural strength of the composite (439 MPa at 50 vol% ZrO_2 addition) but due to its smaller grain size (< 100nm) could not enhance the fracture toughness value [2.67].

Moon et al [2.68] also sintered HA - 3 mol% Y-ZrO_2 composite by pulse electric current sintering method. Samples containing 0, 10, 20 and 30 wt% of ZrO_2 were sintered at $1100^{O}C$, $1150^{O}C$, $1200^{O}C$ and $1250^{O}C$ under a pressure of 50 MPa for 5 minutes in vacuum atmosphere. Maximum flexural strength was obtained for the batch containing 20 wt% HA at $1200^{O}C$. Increasing the temperature beyond $1200^{O}C$ decreased the strength due to reaction between HA and ZrO_2 phase.

Khalil et.al [2.69] consolidated HA-20 vol% 3YSZ composite by high frequency induction heat sintering. Maximum density was 98.6% of theoretical for the composite sintered at $1100^{O}C$ and beyond this temperature the shrinkage curve showed expansion due to the decomposition of HA to TCP. Highest hardness (7GPa) was obtained in $1150^{O}C$ sintered composite and maximum toughness (2.35 $MPam^{½}$) was recorded in $1000^{O}C$ sintered composite.

2.5.6 Effect of ZrO_2 Calcination Temperature on the Phase and Mechanical Property of Sintered Hydroxyapatite-ZrO_2 Composite

The differential shrinkage between HA and ZrO_2 had often adversely affected the sinterability of the composite. The usual perception was to adjust the calcination temperature of either ZrO_2 or HA powder or both to provide a substantial decrease in differential shrinkage. In an important study by Wu et.al [2.70], extensive investigation of the effect of ZrO_2 and HA calcination temperature on the final density of the composite was accomplished. In order to demonstrate such effect, the calcination temperature of ZrO_2 was increased from $800^{O}C$ to $1200^{O}C$ keeping the calcination temperature of HA at $800^{O}C$. The result was a significant increase in sintered density of the composite due to reduction in shrinkage of ZrO_2 agglomerate and thus the reduction in differential shrinkage between HA and ZrO_2 particulate. Further decrease in calcination temperature of HA from $800^{O}C$ to $750^{O}C$ while keeping that of ZrO_2 fixed at $1200^{O}C$ increased the sintered density of the composite even further, which could be attributed to the increased shrinkage of HA and thus decreasing the differential shrinkage further.

2.6 Hydroxyapatite - Low ZrO_2 Composite

All the HA-ZrO_2 composites discussed above involved high volume fraction (≥ 10vol%) of ZrO_2 addition. HA-ZrO_2 composite can also be prepared with low volume % ZrO_2 addition (≤ 10vol%). However, very little information is available on the densification behaviour and mechanical properties of HA - ZrO_2 composites containing low volume fraction of ZrO_2. Some interesting studies show a significant effect of low wt% ZrO_2 addition (≤10 wt %) on the final phase and mechanical properties of the composite especially strength, hardness and toughness without sacrificing the bioactive and biocompatibility aspect of HA, which might be critically hampered by high ZrO_2 loading owing to the bio inertness of ZrO_2 with respect to HA [2.71- 2.75].

2.6.1 Effect of Low ZrO_2 Addition on the Phase Stability of HA-ZrO_2 Composite

Theoretically, considering the gram molecular weights of both HA (1005 gms) and ZrO_2 (123 gms) the decomposition reaction between HA and ZrO_2, requires ≥10 wt% of ZrO_2 for full decomposition all HA to TCP and the decomposed phase in turn determines the final mechanical properties. Such observations were also being reported by Towler et.al [2.71] produced HA-ZrO_2 composite by adding 1, 2, 3, 4, 6 and 10 wt% Y_2O_3-ZrO_2 sol to HA during precipitation. The XRD evidence showed that up to 6 wt% ZrO_2 additions, the stability of HA phase was not affected. Further, additions beyond 6 wt% lead to the decomposition of HA to β-TCP.

In an extension to the above work, Towler et.al [2.72] added low level of zirconia (≤20 wt%) to HA matrix for studying the effect of ZrO_2 addition on the mechanical properties of HA. The variation of sintered density with ZrO_2 addition indicated that above 2.5 wt % ZrO_2 addition the density decreases to 74% for batch containing 20 wt% ZrO_2. A maximum micro hardness (330H_V) and flexural strength (46 MPa) was observed for 1.5 and 2 wt% ZrO_2 additions respectively.

2.6.2 Effect of Low ZrO_2 Addition on the Microstructure and Mechanical Properties of Hydroxyapatite-ZrO_2 Composites

Besides ZrO_2, several other oxide ceramics such as Al_2O_3, TiO_2 have also being tried for reinforcing HA. These ceramics with a grain size below 100 nm and in dense form are supposed to display an enhanced bioactivity with respect to their polycrystalline form. They are also expected to exhibit enhanced bioactivity when the grain sizes are less than 100 nm. Mezahi et.al [2.73] tried to improve the mechanical properties of HA by incorporating different type of oxides like 5 wt% of 12Ce-TZP, Al_2O_3 and TiO_2. The obtained composites were sintered at 1300^{O}C for 2 hrs. For the batch containing 12Ce-TZP, decomposition of HA to β-TCP and free CaO resulted in the formation of $CaZrO_3$.Powder containing TiO_2 shows a partial decomposition of HA to β-TCP. On the other hand, the composite containing Al_2O_3 showed complete decomposition of HA to β-TCP. Similar effects were also observed in case of density, where ZrO_2 addition did not affect the density of HA composite but with TiO_2 the decomposition was accompanied with a decrease in density (90% of theoretical). For HA-Al_2O_3, the composite were highly densified (97% of theoretical density of β-TCP). Micro hardness of the composite with ZrO_2 reinforcement showed higher value than others.

Studies have shown that nanocrystalline HA showed a better biocompatibility compared to polycrystalline HA. Thus efforts have been made to retain HA as well as its reinforcement (ZrO_2) to a grain size below 100 nm which could lead to the formation of nano composites with increased biocompatibility. The advantages of microstructural features could be achieve the same dispersion at low ZrO_2 loading lead to phase stability of final product. Incorporation of all these aspects could only be realized by hot pressing, hot isostatic pressing and spark plasma sintering. This pressure assisted sintering processes allowed a faster densification of compact at low sintering temperature, thereby arresting grain growth [2.65 - 2.68, 2.74, 2.75].

Ahn et.al [2.74] studied the effect of low weight% (1.5 - 15 wt%) nano zirconia loading in HA matrix. The nano zirconia was incorporated by colloidal processing route. Results showed that a high dispersion of ZrO_2 in HA matrix was achieved when zirconia loading was below 8 wt %. Significant improvement in strength and hardness was realized only at low volume percent ZrO2 addition (i.e. up to 3 wt %). The maximum hardness and bending strength of 7.3 GPa and 243 MPa respectively was achieved at 1.5 wt% ZrO_2 loading. High density of the composites in this investigation was obtained by hot pressing the compact at 1000^{o}C under a load of 50 MPa.

Pyda et.al [2.75] studied the effect of low weight % ZrO_2 addition (11.9 vol%) on the sintered microstructure, phase and mechanical properties of hot pressed composite. The hot pressing was carried out between 1150^{O}C - 1250^{O}C for 0.5 hr at 25 MPa pressure in an argon atmosphere. ZrO_2 in various polymorphic forms had been used in this case such as, unstabilised, stabilized with 3 mol% Y_2O_3 or 6 mol% CaO. Needle shaped CaO stabilized ZrO_2 particles prepared by hydrothermal treatment was also incorporated in HA matrix to visualize the effect of reinforcement morphology change on properties of composite. The composite with non stabilized ZrO_2 showed an increase in tetragonal phase with increase in sintering temperature, but the one with CaO and Y_2O_3 stabilized showed cubic phase and the one with needle shape particles showed monoclinic phase. However, no decomposition of HA to TCP was observed in any of the case. The composite with Y_2O_3 stabilized ZrO_2 achieved full densification at lowest sintering temperature i. e $1150^{O}C$. HA with non stabilized zirconia showed highest bending strength (180 MPa) and toughness (1.07 $MPam^{1/2}$) value at $1250^{O}C$.

2.7 Preparation of Hydroxyapatite and Hydroxyapatite–ZrO_2 Composite from Natural Sources

Besides the synthetic routes which uses different calcium and phosphate sources such as $Ca(NO_3)_2$, $Ca(OH)_2$, $CaCO_3$ and $(NH_4)_2HPO_4$, H_3PO_4 etc, attempts have also been made to produce HA from natural sources such as dental enamel, gonipora, sea coral etc. A biomimetic HA comprising of Mg^{2+}, CO_3^{2-}, Na^+, P, F^-, Cl^- , and trace amount of Sr^{2+}, Pb^{2+}, Ba^{2+}, Fe^{3+}, Zn^{2+}, Cu^{2+} could be produced in these cases with the prepared HA resembling the HA found in natural bone structure.

Erkmen et.al [2.76] prepared HA –PSZ composite (with 5 and 10 wt% PSZ) using two different source of HA, enamel derived (EHA) and commercially available (CHA). The XRD patterns showed that for both the sources $CaZrO_3$, β-TCP along with HA and ZrO_2 were present in the samples. The $CaZrO_3$ and β-TCP amount in case of EHA-PSZ, increased both with sintering temperature as well as ZrO_2 content. CHA-PSZ composite on the other hand, showed more $CaZrO_3$ formation at $1200^{O}C$. The compacts containing 5 wt% PSZ showed better hardness value at $1300^{O}C$.There was a decrease in compressive strength for CHA-PSZ(50MPa) composite above $1100^{O}C$ whereas, EHA-PSZ(100MPa) composite behaved differently to give maximum compressive strength at $1300^{O}C$.

Murugan et.al [2.77] synthesized biphasic calcium phosphate ceramics from natural gonipora under microwave irradiation technique. 5 and 10 mol% of ZrO_2 were added to the precipitated powder. The decomposition of HA to β-TCP was lowered to $900^{O}C$ with the addition of ZrO_2. The lowering of decomposition temperature resulted in a biphasic calcium phosphate which could be used as ideal bone substitute due to better resorbability of TCP.

2.8 Phase Stability of HA-ZrO_2 Composite

Before discussing the effect of various parameters on the phase stability of HA in HA-TZP composite, for convenience a detail analysis of the phase diagram of hydroxyapatite system would be useful.

Figure 2.2 refers to the phase diagram of CaO-P_2O_5 in ambient condition and without the presence of any water vapor. The phase diagram shows that various calcium phosphates such as tetra calcium phosphate (C_4P), α-tricalcium phosphate (α C_3P), monetite (C_2P) and mixtures of CaO and C_4P form at different temperatures. However, this phase diagram does not show HA which implies that HA is not stable in ambient condition without water vapor [2.78].

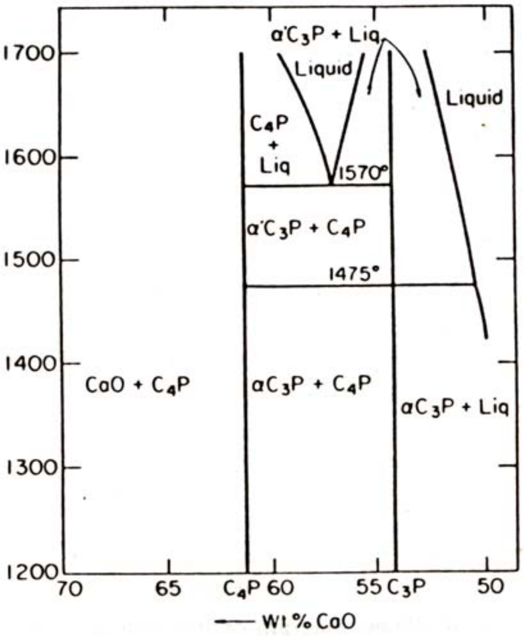

Fig. 2.2. Phase diagram of the system CaO-P_2O_5 at high temperature (vertical axis ^{O}C). No water present. [2.78]

Figure 2.3(a) shows the same phase diagram of CaO-P_2O_5 in ambient condition with presence of water vapor (P H_2O = 500 mmHg) and at different partial pressure of water (Figure 2.3(b)). As the partial pressure of water is increased to 50 mm Hg, HA (Ap) forms. However, the exact stoichiometry of HA depends on the presence of other calcium phosphates mainly C_4P, C_3P and CaO.

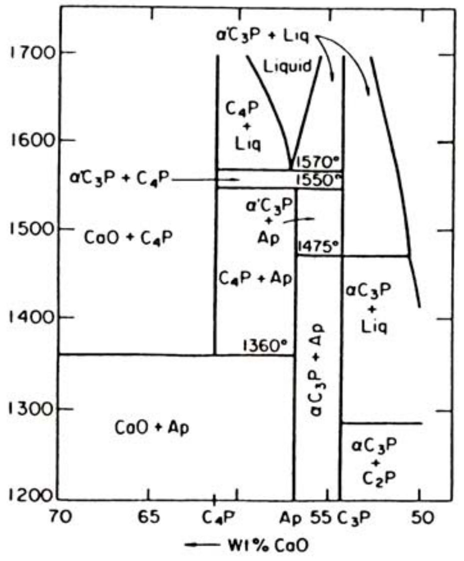

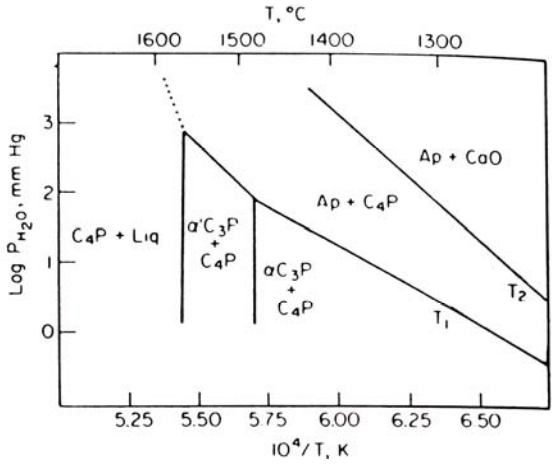

Fig. 2.3(a) Phase diagram of the system CaO-P_2O_5 at high temperature (vertical axis ^{O}C). Water vapor P H_2O = 500 mm Hg. [2.78]

Fig. 2.3(b) Influence of ambient water vapor pressure (vertical axis P H_2O in mmHg) on phase composition. [2.78]

Figure 2.3(a) shows the same phase diagram of CaO-P_2O_5 in ambient condition with presence of water vapor (P H_2O = 500 mmHg) and at different partial pressure of water (Figure 2.3(b)). As the partial pressure of water is increased to 50 mm Hg, HA (Ap) forms. However, the exact stoichiometry of HA depends on the presence of other calcium phosphates mainly C_4P, C_3P and CaO.

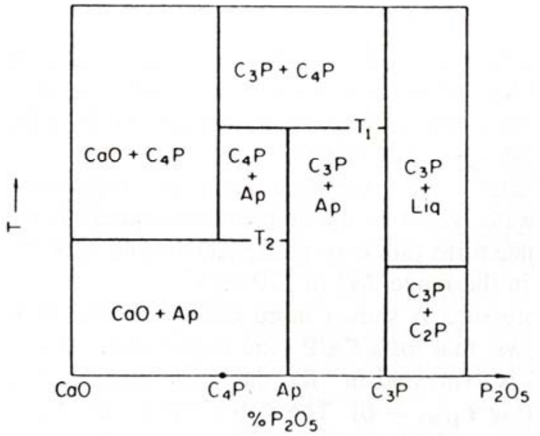

Fig. 2.4 Enlarged part of Fig. 2.3(a) instead of 1360^{O}C T_2 is used and instead of 1475^{O}C T_1 is used, to indicate that these values hold only for P H_2O = 500 mmHg. [2.78]

The importance of partial pressure of water vapor on the phase stability of CaO-P_2O_5 system can be seen in Figure 2.4 which is an enlargement of Figure 2.3(a). The diagram shows that for Ca/P > 1.66 (T = 1300^OC), $10^4/T = 6.4$ and H_2O pressure = 1mm Hg (Log $P_{H_2O} = 0$) the stable phases are a mixture of C_3P and C_4P. On increasing the partial pressure of water from 1mm – 10 mmHg the stable phases are Ap and C_4P. When the P_{H_2O} = 100 mmHg (log pH_2O = 2) the stable phases are A_p + CaO. Thus, if the Ca/P ratio slightly exceeds that of stoichiometric apatite the phase stability depends on P_{H_2O} which is shown in Table 2.2.

Table 2.2 Phase stability as a function of P_{H_2O} [2.78]

log P_{H_2O}	**Stable Phases**
0	$C_3P + C_4P$
1	Ap + C_4
2	Ap + CaO

The above phase diagram demonstrates that the densification and phase stability of HA depends on sintering temperature, Ca/P ratio and water vapor pressure during sintering.

2.8.1 Phase Stability of HA-ZrO_2 Composite

In an attempt to reduce the decomposition of HA in presence of ZrO_2 Heimann et.al [2.79] synthesized HA – 50 wt% monoclinic ZrO_2 composite. Excess amount of CaO (10 ,20, 50 mol%) was added. The phase evolution of the composite with temperature was studied by sintering the composite at 1000^OC, 1100^OC, 1200^OC and 1300^OC each for 1hr. The XRD results showed that t-ZrO_2 amount gradually increased with complete conversion of m-t ZrO_2 taking place at 1300^OC. Although $CaZr_4O_9$ or c-ZrO_2 were absent in any of the samples, $CaZrO_3$ was observed in all the cases. It appeared that the excess CaO added reacted with m-ZrO_2 to form CaO doped t-ZrO_2 and $CaZrO_3$. Thus, the addition of CaO shifted the equilibrium from TCP and tetra CP to HA as observed by the XRD results.

Evis et.al [2.80] made a detailed analysis of the reaction mechanisms between HA and ZrO_2 in a HA-ZrO_2 composite containing low wt % (3, 5.8 and 8.4 wt %) ZrO_2. The authors proposed that Ca^{2+} is extracted from HA matrix by ZrO_2 and the process involved an ion exchange reaction between ZrO^{2+} and Ca^{2+} in the HA matrix. Owing to the larger ionic radius of ZrO^{2+} (0.21nm) compared to that of Ca^{+2}(0.1nm) the unit cell volume of HA was increased with ZrO^{2+} substitution for Ca^{2+}. Thus the ion exchange introduced strains in HA structure making HA structure susceptible for HA to TCP decomposition. On the other hand, with the substitution of Ca^{2+} for ZrO^{2+} the unit cell volume of ZrO_2 shrinked to transform into t-ZrO_2, leading to an increase in density from 5.68 gm/cm^3 (m-ZrO_2) to 6.1 gm/cm^3 (t-ZrO_2). However, the above ion exchange mechanism was possible only if ZrO_2 and HA surfaces were in contact, thus suggesting that the above reactions between HA and ZrO_2 are possible in dense HA-ZrO_2 composite.

Adolfsson et.al [2.81] studied the effect of hot isostatic pressing at 1200^{O}C as well as spark plasma sintering at 1100^{O}C on the phase stability of HA in HA - (40-60 vol%) ZrO_2 composite. The results revealed that in both the cases, HA and ZrO_2 were stable till high temperature. However, the mechanism was different for each case. The theory of the thermal stability of HA, depended on the minimal loss of structural water from HA which could be achieved by hot isostatic pressing technique due to the shift of equilibrium towards HA. Similarly, due the reduced time and temperature required by SPS technique for densification, the diffusion of water from HA lattice was minimized thus maintaining the thermal stability of the composite till 1100^{O}C.

Zhu et.al [2.82] tried a unique way to restore HA phase of the calcined (1500^{O}C) powder with different Ca/P ratio (1.4, 1.5, 1.6, 1.67, 1.7) followed by post heat treatment at 900^{O}C in moist atmosphere. HA powder with different Ca/P ratio (1.4, 1.5, 1.6, 1.67, 1.7) were pre heated at 800^{O}C for 3 hr followed by calcination at 1500^{O}C for 3hrs. XRD results showed that HA decomposed to α-TCP along with small amount of TTCP in all the case, although HA powder with 1.67 Ca/P ratio showed minimal decomposition. Annealing the above calcined (1500^{O}C) powders at 900^{O}C in wet atmosphere lead to the reconstitution of HA phase while the α-TCP and TTCP phase was reduced, which was more pronounced for HA with Ca/P ratio 1.4 and 1.5 respectively along with 1.67.

Park et.al [2.83] studied the effect of hydrothermal reaction temperature and pH on the crystallite size and phase of HA and on HA-20 wt% 3YTZP composite. An increase in reaction temperature decreased the solubility of calcium phosphate leading to a super saturation of the reactant thereby increasing the crystallite size. The TCP content of the compact sintered at $1250^{O}C$ also increased with decrease in pH because the solubility of Ca^{2+} from HA increased at lower pH. Nano HA in HA-TZP composite prepared by hydrothermal treatment at $200^{O}C$ and pH 9 had greater stability compared to the one containing commercial HA, because the outward diffusion of water in dense nanosized HA was slow thereby making HA decomposition difficult.

Prakash et.al [2.84] observed the bands corresponding to CO_3^{-2} in the FTIR spectra of the HA precipitated at various temperature. The spectra also showed the substitution of CO_3^{2-} for OH^- and PO_4^{3-} group in the HA lattice. With an increase in temperature, the carbonate substitution level also decreased as revealed by the spectra. This substitution might have resulted from the carbonate present as impurities in the reactant or the absorption of atmospheric carbon dioxide.

Kim et.al [2.57] prepared HA-ZrO_2 composite (ZrO_2 content up to 50 vol%) in which CaF_2 was added up to 5 vol%. The partial substitution of $(OH)^-$ by F^- suppressed the decomposition of HA to β-TCP along with the formation of fluorapatite. As fluorapatite has a higher thermal stability compared to HA, its decomposition even in the presence of ZrO_2 was suppressed leading to an enhanced sinterability.

Kmita et.al [2.85] prepared HA–ZrO_2 composite by hot pressing using three different type of ZrO_2 viz coarse grained, fine grained and needle shaped. The effect of ZrO_2 morphology and grain size on the sintered phase of the composite was studied. The results depicted that the composite prepared with coarse grained and needle shaped ZrO_2 showed a transformation of monoclinic ZrO_2 to tetragonal symmetry with rise in temperature. However, the composite with fine grain ZrO_2 did not show any such effect.

2.9 In vitro Tests

Although HA possess an excellent biocompatibility, it cannot be presumed that HA based composites are also going to display similar biocompatibility. The stringent processing route may alter the microstructure, composition and many other properties which directly or indirectly may affect the biological reactions between the implant, body fluid and the host tissue. However, the problem with a ZrO_2 reinforced HA composite is its altered biocompatibility, arising out of partial decomposition of HA to TCP, tetracalcium phosphate, release of CaO during the processing of HA-ZrO_2 composite.

The presence of all these phases has an adverse effect on the biocompatibility of composite. Although, TCP (particularly β-TCP) is biocompatible, due to its high resorbability in body fluid, its presence in large amount in HA based composites is undesirable in terms of long stability. Therefore, HA based composite are required to be rigorously tested for evaluating its bioactivity and/or dissolution in a simulated condition generated through SBF.

2.9.1 In vitro Bioactivity of Hydroxyapatite and Hydroxyapatite Based Composite

Delgado et.al [2.86] investigated the effect of SBF aging for 4 weeks on the mechanical as well as the physical activities of HA - ZrO_2 composite. For this purpose, HA- 20 wt% Mg-PSZ composite as well as pure HA (control sample) were prepared, and pressurelessly sintered at 1250^OC/4hrs. The results show a fall in pH value of SBF with aging time which is more evident in case of pure HA. The pH drop could be correlated to the formation of $CaOH^+$, $H_2PO_4^-$ or $CaH_2PO_4^+$ [2.87]. In post SBF aged composite, no significant change in fracture toughness was noticed for either of the samples probably due to the high density of the sintered composite.

Kumar et.al [2.88] carried out the in vitro analysis of HA-20 wt% ZrO_2 composite which had been synthesized by spark plasma sintering. The SEM analysis of the composite surface after SBF aging showed that small spherical structures of hydroxy-carbonated apatite (HCA) were formed on the surface which grew both in density and size with increase in immersion time. The formation of HCA layer at the surface improved the biocompatibility and imitated tissue growth in physiological environment.

Kim et.al [2.89] discussed the effect of SBF treatment on the bone like apatite formation on HA surface sintered at two different temperature 800^OC and 1200^OC respectively. The authors made a thorough investigation of apatite formation mechanism, using a combined TEM EDX analysis. Results showed that the exposure time required for the formation of bone like apatite on sintered (1200^OC) HA is more compared to the one sintered at 800^OC. The first structural change which the HA goes in its course of interaction with SBF was the formation of a Ca rich amorphous calcium phosphate (ACP) on the surface. The second structural change involved the formation of a Ca deficient ACP, when HA interacted with the $(PO_4)^{3-}$ available in SBF using the Ca rich ACP. The next step featured the gradual crystallization of Ca poor apatite to bone like apatite through which HA stabilized on the surface as shown below (Fig. 2.5). The iso - electric point of HA in water lies between pH-5 to pH-7, since the pH of SBF is higher (7.4) on submersion in SBF a negative surface charge could be developed by exposing the hydroxyl and phosphate ions in its structure.

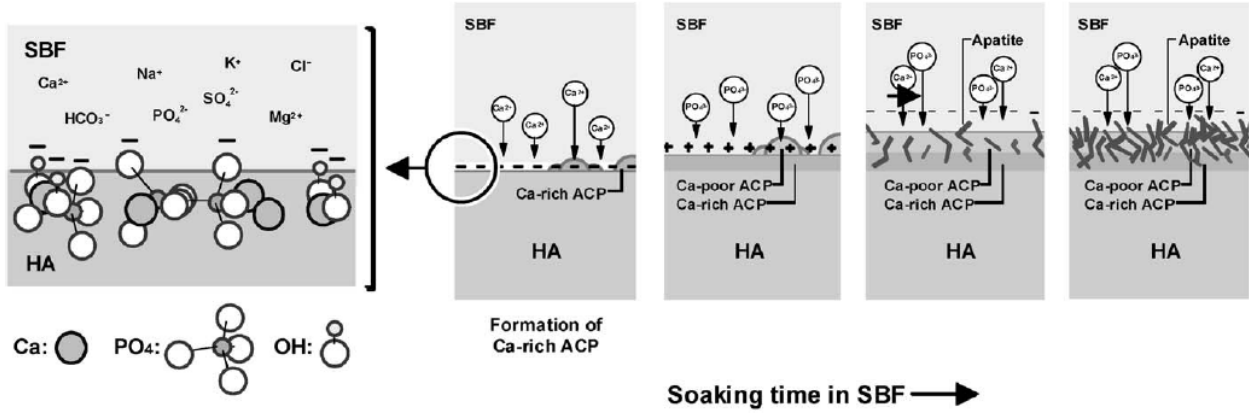

Fig. 2.5 Kinetics of apatite formation on HA surface in SBF [2.89]

The investigation by Kokubo et.al [2.90] showed the utility of SBF in predicting the in vivo bioactivity of material. Several systems such as Na_2O-CaO-SiO_2-P_2O_5 glass, Na_2O-CaO- B_2O_3-Al_2O_3-SiO_2-P_2O_5 glass, A-W glass ceramics along with hydroxyapatite and Apatite/β-tricalcium phosphate form apatite layer on their surface on immersion in SBF and a similar response was observed with the formation of calcium phosphate layer in vivo. However, there are certain materials like A-W glass ceramic, which behaved the other way, demonstrating no such effect both in SBF or in vivo test proving the importance of SBF in predicting the in vivo bioactivity. Besides, there are certain other materials such as abalone shell which showed apatite formation on their surface in SBF but does not bond to living bone owing to the antibody reactions to proteins in the shell. [2.91, 2.92] This confirms that a material forming apatite layer in SBF is expected to behave in the same way in a living body provided no anti body or toxic reactions take place. Thus, the number of animal experiment i.e. in vivo could be easily reduced.

Xin et.al [2.93] discussed in detail the induced calcium phosphate formation on several bioceramics surfaces such as HA, HA/TCP, β-TCP, α-TCP, bioglass, glass ceramics etc in simulated body fluid and in rabbit muscle site. A comparative in vitro analysis of the above substances in SBF showed no calcium phosphate formation on the surface of β-TCP even after immersion in SBF for 5 days. HA, HA/TCP and α-TCP along with A-W glass ceramic showed reasonable amount of calcium phosphate granules of various morphology and amount being formed on their surfaces after one day of SBF treatment. Although the precipitation on the specimen surface after being implanted in rabbits muscle is much less (even after one week) compared to in vitro SBF treatment for one or two day, but still HA/TCP and α-TCP specimen showed best result with β-TCP again not showing any sign of Ca-P formation on its surface even after being implanted for 6 weeks.

Obata et.al [2.94] found an alternative method to enhance the bioactivity of β-TCP along with other bioceramics such as HA. Results showed that autoclaving the samples with distilled water in the range 100-180^{O}C for 1 hr can improves the bone like apatite formation on the surface of both β-TCP and HA remarkably but, no such deposit was observed on the surface of non autoclaved β-TCP. The low surface potential and roughness induced by autoclaving could be the reason behind formation of bone like apatite on β-TCP surface. Similar change in surface morphology of HA with formation of leaf like apatite was also observed by the effect of autoclave.

Tas [2.25] prepared biomimetic HA from synthetic body fluid at 37^{O}C. The important aspect of this work also included the preparation of SBF in a modified manner with its ionic concentration being more close to that of human plasma, particularly of Cl^- with respect to the SBF synthesized by Kokuba et.al [2.90] as shown below (Table 2.3). The HA obtained by following the method of Tas route was found to mimic natural bone structure with thermal stability up to 1600^{O}C.

Table 2.3 Ion concentrations of SBF solutions and human plasma [2.25, 2.90]

Ion	**Kokubo et.al. (mM)**	**Tas et.al. (mM)**	**HumanPlasma (mM)**
Na	**142.0**	**142.0**	**142.0**
Cl^-	**147.8**	**125.0**	**103.0**
HCO_3^-	**4.2**	**27.0**	**27.0**
K^+	**5.0**	**5.0**	**5.0**
Mg^{2+}	**1.5**	**1.5**	**1.5**
Ca^{2+}	**2.5**	**2.5**	**2.5**
HPO_4^{2-}	**1.0**	**1.0**	**1.0**
SO_4^{2-}	**0.5**	**0.5**	**0.5**

2.9.2 In vitro Biocompatibility Test of Hydroxyapatite and Hydroxyapatite-ZrO_2 Composite

Quan et.al [2.95] studied the in vitro biocompatibility of a graded HA-ZrO_2 composite through acute toxicity test, cytotoxicity test and hemolysis assay. The cytotoxicity behaviour was evaluated by studying the cell proliferation ratio and cell morphology using L929 mouse fibroblast. The blood compatibility of the composite was tested with hemolysis assay. This is significant in the sense that damaged blood cells may lead to serious consequence with the formation of thrombus. The hemolysis ratio of the sample group in this case is 1.7%, which is close to that of negative control sample (0%). The results indicated the compatibility of the composite with red blood cell. Based on these results, in vitro tests and animal tests were also performed, which confirmed the biocompatibility of the composite.

Sadi et.al [2.96] analysed the effect of PSZ addition on the biological property of HA - high density polyethylene (HA/HDPE) composite. The biocompatibility in this case was observed by making in vitro analysis using human osteoblast cells. Results showed that increasing the amount of HA to HDPE increased the ALP production of osteoblastic cells. Addition of PSZ to HA/HDPE composite showed further increase in ALP production after incubating for 14 days indicating PSZ addition was beneficial for bone bonding.

Kmita et.al [2.97] carried out cytotoxicity test on hot pressed (1150 -1300^{O}C) HA-20wt % ZrO_2 composite. The invitro method using mouse fibroblast 3T3/ Balb was used to study the cytotoxicity. The interaction at cell material interface was observed to evaluate the biocompatibility of the composite. The cell culture was done on HA-ZrO_2 composite, and monophasic HA and six control samples. The biocompatibility of monolithic HA was highest, and with ZrO_2 addition (i.e. in HA-ZrO_2 composite) no adverse effect on the biocompatibility of the composite was observed. This could be attributed to the absence of other phases like $CaZrO_3$ which reduces biocompatibility.

Hing et.al [2.98] studied the effect of impurity phases such as CaO on the in vivo behaviour of HA. For this purpose, HA with two different Ca/P ratios 1.67 and 1.7 were prepared. The XRD graph of the HA, with Ca/P 1.7, showed the presence of a small peak of CaO. In vivo analysis was performed by implanting a cylindrical sample for 3 weeks in the distal femur of a New Zealand rabbit. The morphology of bone generated around both the implant was quite different both in terms of volume and level of organization of osseous tissue. The bone formed around HA with excess CaO was less dense with a disordered structure. However, a direct bone formation on the surface of phase pure HA was observed.

Chen et.al [2.99] carried out HRTEM study of the in vivo bonded zone between HA and bone. After 3 months of implantation, continuous nano structure was formed between the bones and HA having Ca and phosphorus level higher than that of natural bone. The bond formation appeared to be due to the higher superstauration level of the submerging solution which transformed crystalline HA to an amorphous structure by a dissolution and reprecipitation mechanism.

In a study by Nagarajan et.al [2.100] the in vitro cell test carried out using SP2-O cells on HA-ZrO_2 composite showed good biocompatibility. The growth inhibition percentage was estimated by counting number of living cells in the samples and comparing it with the positive control. In one of the composite 20% prohibition in growth was observed but this value is assumed to be secure and adequate for biomedical applications.

References

2.1. S. J. Kalita, A. Bhardwaj, H. A. Bhatt, “Nanocrystalline calcium phosphate ceramics in biomedical engineering”, Mater. Sc. and Engg. C, 27, 441-449 (2007).

2.2. C. Meneghini, M.C. Dalconi, S. Nuzzo, S. Mobilio and R.H. Wenk, “Rietveld Refinement on X-Ray Diffraction Patterns of Bioapatite in Human Fetal Bones”, BioPhysical Journal, 84, 2021-2029(2003),] .[J.S. Bow, S.C. Liou and S.Y. Chen, Biomaterials, 25, 3155 (2004).

2.3. C. Meneghini, M.C. Dalconi, S. Nuzzo, S. Mobilio and R.H. Wenk, “Rietveld Refinement on X-Ray Diffraction Patterns of Bioapatite in Human Fetal Bones”, BioPhysical Journal, 84, 2021-2029 (2003).

2.4. C.A. Beevers and D.B. McIntyre, “The Atomic Structure of Fluorapatite and its Relation to that of Tooth and Bone Mineral”, Miner. Mag., 27, 254-259 (1956).

2.5. J.F. Kay, “Calcium Phosphate Coating for Dental Implants”, Dent. Clin. North. Amer.,36, 1-18(1992).

2.6. R.A. Young and D.W. Holeomb, “Variability of Hydroxyapatite Preparation”, Calcif. Tissue. Int., 34, 517-532(1982).

2.7. Larry .L.Hench and June Wilson . “An introduction to Bioceramics, Vol 1”. Advanced Materials Research Centre. University of Florida. Gainesville,FL.

2.8. V.V. Silva and F.S. Lameiras, “Synthesis and characterization of composite powders of partially stabilized zirconia and hydroxyapatite”. Materials Characterization 45, 51- 59 (2000).

2.9. Robinson RA. “An electron-microscopic study of the crystallite inorganic component of bone and its relationship to the organic matrix.” J Bone Jt Surg, 34, 389- 435 (1952).

2.10. T.S.B. Narasaraju and D.E. Febe, “Some Physico-Chemical Aspects of Hydroxylapatite”, Journal of Materials Science, 31, 1-21(1996).], [J.C. Elliot, P.E. Mackie and R.A. Young, “Monoclinic Hydroxyapatite”, 180, 4090(10-55 – 1057).

2.11. J.C. Elliot, P.E. Mackie and R.A. Young, “Monoclinic Hydroxyapatite”, 180, 4090(1055 – 1057.

2.12. C.G. Vazquez, C.P. Barba and N. Munguia, “Stoichiometric hydroxyapatite obtained by precipitation and sol gel processes”, Revista Mexicana De Fisica, 51**,** 3, 284–293 (2005).

2.13. R.E. Rimana, W.L. Suchaneka, K. Byrappaa, C.W. Chena, P. Shuka and C.S. Oakesa, Solid State Ionics 151, 393 (2002).

2.14. S.H. Rhee and J. Tanaka,. “Hydroxyapatite coating on a collagen membrane by a biomimetic method”*, J. Am. Ceram Soc.,* 3029 (1998).

2.15. L. B. Kong, J. Ma and F. Boey, “Nanosized hydroxyapatite powders derived from coprecipitation process”, Journal of Materials Science 37, 1131(2002).

2.16. K. Donadel and M.C.M. Laranjeira, V.L. Gonealves, V.T. Faver, J.C. Lima and L.H.M. Prates, “Hydroxyapatite produced by wet- chemical methods”, J. Am. Ceram. Soc., 88, 2230-2245 (2005).

2.17. S. J. Kalita, S. Bose, H. L. Hosik and A. Bandyopadhyay, “CaO-P_2O_5-Na_2O based sintering additives for hydroxyapatite (HAp) ceramics”, Biomaterials, 25, 2331-2339 (2004).

2.18. A. Jillavenkatesa and R.A. Condrate, “Sol-gel processing of hydroxyapatite”, Journal of Materials Science, 33, 4111-4119 (1998).

2.19. M.R. Saeri, A. Afshar, M. Ghorbani, N. Ehsani and C.C. Sorrell, “Wet precipation process of hydroxyapatite”, Materials letter, 57, 4064-4069 (2003).

2.20. I. Mobasherpour , M. Soulati Heshajin , A. Kazemzadeh and M. Zakeri, “Synthesis of nano crystalline hydroxyapatite by using precipation technique”, Journal of Alloys and Compounds, 430, 330-333 (2007).

2.21. N. Rameshbabu, K.P. Rao and T.S. Sampat Kumar, “Accelerated microwave processing of nanocrystalline hydroxyapatite”, Journal of Material Science, 40, 6319-6323 (2005).

2.22. D. Choi and P.N. Kumta, “An alternate chemical route for the synthesis and thermal stability of chemically enriched hydroxyapatite”, J. Am. Ceram. Soc., 89, 444-449 (2006).

2.23. Z. Yang, Y. Jiang, Y. Wang, L. Ma and F. Li, “Preparation and thermal stability analysis of hydroxyapatite derived from the precipitation process and microwave irradiation method”, Materials Letters, 58, 3586-3590 (2004).

2.24. Y. Li and D. li, “Preparation of nano carbonate - substituted hydroxyapatite from an amorphous precursor”, International Journal of Applied Ceramic Technology, 5, 442-448 (2008).

2.25. A. C. Tas, “Synthesis of biomimetic Ca-hydroxyapatite powders at 37^{o}C in synthetic body fluid”, Biomaterials, 21, 1429-1438 (2000).

2.26. M. Jarcho, C.H. Bolen, M.B. Thomas, J. Babock, J.F. Kay and R.H. Doremus, “Hydroxyapatite synthesis and characterization in dense polycrystalline form”, J. Mater. Sci., 11, 2027-2035 (1976).

2.27. A.C. Tas, F. Korkusuz, M. Timucin and N. Akkas, “An investigation of the chemical synthesis and high-temperature sintering behaviour of calcium hydroxyapatite (HA) and tricalcium phosphate (TCP) bioceramics”, J Mater Sci: Mater Med, 8, 91-96 (1997).

2.28. H.E.L. Madsen and G. Thodvadarson, “Precipitation of calcium phosphate from moderately acid solutions”, J. Crystal Growth 66, 369-376 (1984).

2.29. C. Kothapalli, M. Wei, A. Vasiliev and M.T. Saw, “Influence of temperature and concentration on the sintering behaviour and mechanical properties of hydroxyapatite”, Acta Materialia, 52, 5655-5663 (2004).

2.30. H. Varma, S.P. Vijayan and S.S. Babu, “Transparent hydroxyapatite ceramics through gel casting and low temperature sintering”, J. Am. Ceram. Soc, 85, 493-495 (2002).

2.31. C.L. Yun, Z.C. Bo and H.J. Feng, “Influence of temperature, [Ca^{2+}], Ca/P ratio and ultrasonic power on the crystallinity and morphology of hydroxyapatite nano particles prepared with a novel ultrasonic precipitation method, Materials Letters, 59, 1902-1906 (2005).

2.32. N. Thangamani, K. Chinnakali and F.D. Gnanam, “The effect of powder processing on densification, microstructure and mechanical properties of hydroxyapatite”, Ceramics Internationls, 28, 355-362 (2002).

2.33. H.Y. Juang and M.H. Hon, “Effect of calcination on sintering of hydroxyapatite”, Biomaterials, 17, 2059-2064 (1996).

2.34. A. Tampeiri, G. Celotti, S. Sprio and C. Mingazzini, “Characteristics of synthetic hydroxyapatites and attempts to improve their thermal stability”, Materials Chemistry and Physics, 64, 54-61(2000).

2.35. M.M. Seckler, M. Danese, S. Derenzo, J.V. Valarelli, M. Giulietti and R.R. Clemente, “Influence of process conditions on hydroxyapatite crystallinity obtained by direct crystallization”, Materials Research, 2, 59-62, 1999.

2.36. Y. Zhang and Y. Yokogawa, “Effect of drying conditions during synthesis on the properties of hydroxyapatite powders”, J. Mater Sci: Mater Med., 19, 623-628 (2008).

2.37. K.H.Prakash, C.P. Ooi, R.Kumar, K.A. Khor and P. Cheng, “Effect of super saturation level on the size and morphology of hydroxyapatite precipitate”,IEEE, (2006).

2.38. N. Asaoka, S. Best, J.C. Knowles and W. Bonfield, “Characterisation of hydroxyapatite precipitated from different reactants”, Bioceramics, 8, Butter worth: oxford, 331-337 (1995).

2.39. M.G.S. Murray, J. Wang, C.B. Ponton and P.M. Marquis, “An improvement in the processing of hydroxyapatite ceramics”, Journal of Materials Science, 30, 3061-3074 (1995).

2.40. A. Wang, H. Yin, D. Liu, H. Wu, Y. Wada, M. Ren, Y. Xu, T. Jiang and X. Cheng, “Effects of organic modifiers on the size-controlled synthesis of hydroxyapatite nanorods”, Applied Surface Science, 253, 3311-3316 (2007).

2.41. A. Afshar, M. Ghorbani, N. Ehsani, M.R. Saeri and C.C. Sorrell, “Some important factors in the wet precipitation process of hydroxyapatite”, Materials and Design, 24, 197-202 (2003).

2.42. S. Best and W. Bonfield, “Processing behaviour of hydroxyapatite powders with constrating morphology”, Journal of Materials Science: Materials in Medicine, 5, 516-521 (1994).

2.43. M.A. Fanovich and J.M. Porto Lopez, “Influence of temperature and additives on the microstructure and sintering behaviour of hydroxyapatites with different Ca/p ratio”, Journal of Materials Science: Materials in Medicine, 9, (53-60) 1998.

2.44. S. Ramesh, C.Y. Tan, I. Sopyan, M. Hamdi and W.D. Teng, “Consolidation of nanocrystalline hydroxyapatite powder”, Science and Technology of Advanced Materials, 8, 124-130 (2007).

2.45. W. Suchanek, M. Yashima, M. Kakihana and M. Yoshimura, “Hydroxyapatite/Hydroxyapatite-whisker composites without sintering additives: Mechanical properties and microstructural evolution”, J. am. Ceram. Soc.,80, 2805-2813(1997).

2.46. D. Veljovic, B. Jokic, R. Petrovic, E. Palcevskis, A. Dindune, I.N. Mihailescu and D. Janackovic, “Processing of dense nanostructured HAP ceramics by sintering and hot pressing”, Ceramic international, 35, 1407-1413 (2009).

2.47. C.M.S. Ranito, F.A. Costa Oliveira and J.P. Borges, “Mechanical characterization of dense hydroxyapatite blocks”, Materials Science Forum, 514-516, 1083-1086 (2006).

2.48. J.C. Knowles, S. Talat and J.D. Santos, “Sintering effects in a glass reinforced hydroxyapatite”, Biomaterials, 17, 1437-1442 (1996).

2.49. W. Suchanek, M. Yashima, M. Kakihana and M. Yoshimura, “Hydroxyapatite ceramics with selected sintering additives”, Biomaterials, 18, 923-933 (1997).

2.50. S.J. Kalita, S. Bose, H.L. Hosick and A. Bandyopadhyay, “CaO-P_2O_5-Na_2O based sintering additives for hydroxyapatite ceramics”, 25, 2331-2339 (2004).

2.51. F.N. Oktar and G. Goller, “Sintering effects on mechanical properties of glass reinforced hydroxyapatite composites”, Ceramic International, 28, 617-621(2002).

2.52. M.S. Abu Bakar, P. Cheang and K.A. Khor, Mater. Sci. Eng. A, 345, 55 (2003).

2.53. P. Maiti, Y. Prakash, P. Jaya, J. Nanosci. Nanotechnol. 8, 1858 (2008).

2.54. H. W. Kim, Y. H. Koh, B. H. Yoon, and H. E. Kim, “Reaction sintering and mechanical properties of hydroxyapatite-zirconia composites with calcium fluoride additions“, J. Am. Ceram. Soc., 85, 634 (2002).

2.55. R. Ramachandra Rao and T. S. Kannan, “Synthesis and sintering of hydroxyapatite-zirconia composites”, Mater. Sci. Eng., 20, 187 (2002).

2.56. A. Krajewski, A. Ravaglioli, N. Roveri, A. Bigi and E. Foresi, “Effect of fluoride, chloride and carbonate ions introduced by cyclic pH fluctuation on the physic-chemical properties of apatite - based ceramics”, Journal of Materials Science, 25, 3203-3207 (1990).

2.57. H.W. Kim, Y.J. Noh, Y.H. Koh, H.E. Kim and H.M. Kim, “Effect of CaF_2 on densification and properties of hydroxyapatite-zirconia composites for biomedical applications”, Biomaterials, 23, 4113-4121 (2002).

2.58. S.H. Kim, H.C. Lee, H.G. Bang and S.Y. Park, “Effect of MgF_2 additive on the mechanical properties in hydroxyapatite/zirconia composites”, Materials Science Forum, 510, 478-481 (2006).

2.59. R.R. Rao and T.S. Kannan, “Synthesis and sintering of hydroxyapatite-zirconia composites”, Materials Science and Engineering C, 20, 187-193 (2002).

2.60. V.V. Silva and F.S. Lameiras, “Synthesis and characterization of composite powders of partially stabilized zirconia and hydroxyapatite”, Materials Characterizations, 45, 51-59 (2000).

2.61. V.V. Silva, F.S. Lameiras and R.Z. Domingues, “Microstructural and mechanical study of zirconia-hydroxyapatite (ZH) composite ceramics for biomedical applications”, Composites Science and Technology, 61, 301-310 (2001).

2.62. J.A. Delgado, L. Morejon, S. Martinez, M.P. Ginebra, N. Carlsson, E. Fernandez, J.A. Planell, M.T.C. Mora and J. R. Viejo, “Zirconia – toughened hydroxyapatite ceramic obtained by wet sintering”, Journal of Materials Science: Materials in Medicine, 10, 715-719 (1999).

2.63. A.R. Kimta, A. Slosarczyk and Z. Paszkiewicz, “Mechanical properties of HAp-ZrO_2 composites, Journal of the European Ceramic Society, 25, (2005).

2.64. M. Takagi, M. Mochida, N. Uchida, K. Saito and K. Uematsu, “Filter cake forming and hot isostatic pressing for TZP- dispersed hydroxyapatite composite”, Journal of Materials Science: Materials in Medicine, 3, 199-203 (1992).

2.65. X. Miao, Y. Chen, H. Guo and K.A. Khor, “Spark plasma sintered hydroxyapatite-yttria stabilized zirconia composites”, Ceramics International, 30, 1793-1796 (2004).

2.66. Z. Shen, E. Adolfsson, M. Nygren, L. Gao, H. Kawaoka and K. Niihara, “Dense hydroxyapatite-zirconia ceramic composites with high strength for biological applications”, Advanced Materials, 3, 13 (2001).

2.67. R.H.J. Hannink , P.M. Kelly and B.C. Muddle, J. Am. Ceram. Soc., 83, 461(2000).

2.68. B.K. Moon, D.H. Choi, R.J. Sung, S.H. Kim and K. Niihara, “Fabrication of zirconia-hydroxyapatite composites for biological materials”, Materials Science Forum, 486-487, 101-104 (2005).

2.69. K.A. Khalil, S.W. Kim and H.Y. Kim, “Consolidation and mechanical properties of nanostructured hydroxyapatite – (ZrO_2 + 3 mol% Y_2O_3) bioceramics by high frequency induction heat sintering”, Materials Science and Engineering A, 456, 368-372 (2007).

2.70. J.M. Wu and T.S. Yeh, “Sintering of hydroxylapatite-zirconia composite materials”, Journal of Materials, 23, 3771-3777 (1988).

2.71. M.R. Towler, I.R. Gibson and S.M. Best, “Novel processing of hydroxyapatite zirconia composites using nano-sized particles”, Journal of Materials Science letters, 19, 2209-2211 (2000).

2.72. M.R. Towler and I.R. Gibson, “The effect of low levels of zirconia addition on the mechanical properties of hydroxyapatite”, Journal of Materials Science Letters, 20, 1719-1722 (2001).

2.73. F. Mezahi, A. Harabi, S. Zouai, S. Achour and D.B. Assollant, “Effect of stabilized ZrO_2, Al_2O_3 and TiO_2 on sintering of hydroxyapatite”, Materials Science Forum, 492-493, 241-246 (2005).

2.74. E.S. Ahn, N.J. Gleason and J.Y. Ying, “The effect of zirconia reinforcing agents on the microstructure and mechanical properties of hydroxyapatite - based nanocomposites”, J. Am. Ceram. Soc, 88, 3374-3379 (2005).

2.75. W. Pyda, A. Slosarczyk, M. Haberko, Z. Paszkiewicz, A. R. Kmita and A. Pyda, “Effect of chemical composition and morphology of zirconia particles on properties of HAp-zirconia particulate composites”, Key Engineering Materials, 206-213, 1567-1570 (2002).

2.76. Z.E. Erkmen, Y. Genc and F. N. Oktar, “Microstructural and mechanical properties of hydroxyapatite –zirconia composites”, J. Am. Ceram. Soc, 90, 2885-2892 (2007).

2.77. R. Murugan and S. Ramakrishna, “Effect of zirconia on the formation of calcium phosphate bioceramics under microwave irradiation”, Materials Letters, 58, 230-234 (2003).

2.78. An Introduction to Bioceramics, L. L. Hench and J. Wilson, chapter 11, page 199-222, World Scientific publishing co, 1999.

2.79. R.B. Heimann and T.A. Vu, “Effect of CaO on thermal decomposition during sintering of composite hydroxyapatite-zirconia mixtures for monolithic bioceramic implants”, Journal of Materials Science Letters, 16, 437-439 (1997).

2.80. Z. Evis, “Reactions in hydroxylapatite-zirconia composites”, Ceramics International, 33, 987-991 (2007).

2.81. E. Adolfsson and Z. Shen, “Densification of zirconia-hydroxyapatite ceramics without phase changes”, Key Engineering Materials, 309-311,1141-1144 (2006).

2.82. Q. Zhu, M. Lv and J. Wu, "Effect of Ca/P molar ratio and heat treatment on thermal decomposition and reconstitution of hydroxyapatite", 330-332, 107-110 (2007).

2.83. S.H. Park, I.Y. Ryu, D.J. Kim, J.S. Han and M.H. Lee, "Influence of hydrothermal reaction temperature and ph on phase stability of hydroxyapatite", Key Engineering Materials, 330-332, 147-150 (2007).

2.84. K.H. Prakash, C.P. Ooi, R. Kumar, K.A. Khor, P. Cheang, "Effect of super saturation level on the size and morphology of hydroxyapatite precipitate", IEEE, (2006).

2.85. A.R. Kmita, A. Slosarczyk, Z. Paszkiewicz and C. Paluszkiewicz, "Phase stability of hydroxyapatite-zirconia (HAp – ZrO_2) composites for bone replacement", Journal of molecular structure, 704, 333-340 (2004).

2.86. .A. Delgado, S. Martinez, L. Morejon, M.P. Ginebra, E. Fernandez, M.T. Clavaguera-Mora, J.R. Viejo, F.J. Gil and J.A. Planell, "Physical and mechanical behaviour of zirconia - hydroxyapatite ceramics after aging in simulated body fluid", Key Engineering Materials, 218-220, 161-164 (2002).

2.87. S. Raynaud, E. Champion, D. B. Assolant and D. Teratd, "Dynamic fatigue an degradation in solution of hydroxyapatite ceramics", J. Mater. Sci: Mater . Med., 9, 221-227 (1998).

2.88. R. Kumar, P. Cheang and K.A. Khor, "Spark plasma sintering and in vitro study of ultra-fine HA and ZrO_2-HA powders", Journal of Materials Processing Technology, 140, 420-425 (2003).

2.89. H.M. Kim, T. Himeno, T. Kokubo and T Nakamura, "Process and kinetics of bonelike apatite formation on sintered hydroxyapatite in a simulated body fluid", Biomaterials, 26, 4366-4373 (2005).

2.90. T. Kokubo and H. Takadama, "How useful is SBF in predicting in vivo bone bioactivity?", Biomaterials, 27, 2907-2915 (2006).

2.91. C. Ohtsuki, Y. Aoki, T. Kokubo, Y. Fujita, S. Kotani and T. Yamamuro, "Bioactivity of lime stone and abalone shell", Transactions of the 11th annual meeting of Japanese Society for Biomaterial, 12 (1989).

2.92. Y. Fujita, T. Yamamuro, T. Nakamura, S. Kotani, T. Kokubo and C. Ohtsuki, "The bonding behaviour of limestone and abalone shell to bone", Transactions of the 11th annual meeting of Japanese Society for Biomaterial, 3 (1989).

2.93. R. Xin, Y. Leng, J. Chen and Q. Zhang, “A comparative study of calcium phosphate formation on bioceramics in vitro and in vivo”, Biomaterials, 26, 6477-6486 (2005).

2.94. A. Obata, T. Fujimoto and T. Kasuga, “Enhancement of bone like apatite forming abilities of calcium phosphate ceramics in SBF by autoclaving”, Journal of the Ceramic Society of Japan, 114, 63-66 (2006).

2.95. R. Quan, D. Yang, X. Wu, H. Wang, X. Miao and W. Li, “In vitro and in vivio biocompatibility of graded hydroxyapatite-zirconia composite bioceramic”, J. Mater Sci: Mater Med, 19, 183-187 (2008).

2.96. A.Y. Sadi, M.A. Shokrgozar, S.H. Homaeigohar, M. Hosseinalipour, A. Khavandi and J. Jadavpour, “The effect of partially stabilized zirconia on the biological properties of HA/HDPE composites in vitro”, J. Mater Sci: Mater Med, 17, 407-412 (2006).

2.97. A.R. Kmita, A. Slosarczyk, Z. Paszkiewicz and D. Paluch, “Evaluation of HAp-ZrO_2 composites and monophase HAp bioceramics. Invitro study”, Journal of Materials Science, 39, 5865-5867 (2004).

2.98. K.A. Hing, I.R. Gibson, P.A. Revell, S.M. Best and W. Bonfield, “Influence of phase purity on the in vivo response to hydroxyapatite”, Key Engineering Materials, 192-195, 373-376 (2001).

2.99. Q.Z. Chen, W.W. Lu, C.T. Wong, K.M.C. Cheung, J.C.Y. Leong and K.D.K. Luk, “ HRTEM and EDX investigation of microstructure of bonding zone between bone and hydroxyapatite in vivo”, Key Engineering Materials, 254-256, 165-168 (2004).

2.100. V.S. Nagarajan and K.J. Rao, “Structural, mechanical and biocompatibility studies of hydroxyapatite - derived composites toughened by zirconia addition”, J. Mater. Chem., 3, 43-51 (1993).

Chapter III

Statement of Problem

A comprehensive review on HA and HA-TZP composites reveal that wet precipitation technique was mainly used for composite powder preparation, which is more likely to produce a more homogeneous powder through the control of a number of processing parameters such as pH, temperature, aging time etc. At the same, it may be mentioned that studies also focused on the processing of HA-ZrO_2 composites through solid state route because of the sheer simplicity of the process and its cost effectiveness. However, it was also observed that this process resulted in a less dense composite with decomposition of HA, lower amount of retained t-ZrO_2 as well as formation of TCP, tetracalcium phosphate, $CaZrO_3$ etc. In light of this as already mentioned major processing routes were the chemical precipitation routes. It was also noted that most of the investigation on HA-ZrO_2 composite contained high (≥ 15 volume %) ZrO_2. It is well known that HA has affinity towards ZrO_2 and in the HA-ZrO_2 composites, the reaction leads to the decomposition of HA as well as loss of ZrO_2. The presence of large amount of ZrO_2 hampered the densification process and it also accelerated the decomposition of HA to TCP along with conversion of TZP to $CaZrO_3$. The use of sophisticated techniques like hot pressing, hot isostatic pressing and spark plasma sintering helps to arrest these decomposition reaction through low temperature densification. All these HA- high ZrO_2 composites had good strength and some improvement in K_{IC}. The best reported values for strength and toughness were 439MPa (50vol% ZrO_2) and 2.35MPam$^{1/2}$ (20vol% ZrO_2) respectively. The results indicate that transformation toughening did not have a major role in toughness enhancement and rather microcrack toughening was the more possible mechanism. On the other hand the processing, densification behaviour and mechanical properties of HA – ZrO_2 composites with low volume fraction ZrO_2 (< 10 volume %) has been less widely studied. The possible reason may be the apprehension that low volume fraction ZrO_2 may not enhance properties as desired and the second reason may be due to difficulty of uniform dispersion of low volume % zirconia in HA matrix. But since the ZrO_2 volume is lower it will cause lesser interaction and will help to retain both HA and TZP phase, thus it is expected that HA - TZP composites containing lower volume fraction of TZP will have improved mechanical properties. Small amount of TZP also not expected to have an adverse effect on the biological characteristics of the composite. But some processing modification is still needed to obtain a dense HA-TZP composite, while minimizing the decomposition reaction between HA and TZP phase.

Thus, the present study aims to study the following specific aspects of HA-TZP composites containing low volume % TZP:

I. Hydroxyapatite powder processing by two chemical precipitation routes using $Ca(NO_3)_2.4H_2O$ and $(NH4)_2HPO_4$ as the source material and its effects on the phase, thermal stability and densification behaviour to be studied. This aspect will be studied using two different powder processing routes for HA, viz. normal precipitation (NP) route and reverse strike precipitation (RS) route.

II Preparation of dense HA -TZP nanocomposite having varying weight percent of TZP (2, 5, 7.5 and 10 weight%) i.e. 1.02, 2.65, 4.01 and 5.44 volume percent using optimized precipitation route and to study the composite properties i.e. phase, microstructures, strength, toughness and hardness. The main aim is to maximize the fraction of hydroxyapatite (HA) and TZP retention in the sintered sample.

III Study of the effect of TZP calcination temperature on the density, phase, microstructure and mechanical properties of the sintered HA-TZP composite. To study this part, the observed strength, toughness and hardness values will be correlated with phase, density and microstructure.

IV Study of the effect of hot pressing on phase, density, microstructure and mechanical properties of HA-TZP composites. The hot pressing experiment will be done on the batches containing TZP calcined at different temperatures $850^{O}C$ and $1200^{O}C$.

V Study of the physiological behaviour of sintered and hot pressed HA-TZP composites through *invitro* bioactivity, *invitro* cytotoxicity and *invitro* hemocompatibility tests.

Chapter IV

Experimental Work

4. Preparation of HA-TZP Composite Powder:

HA-ZrO_2 composite containing varying weight % of TZP (2, 5, 7.5 and 10) was prepared by reverse strike precipitation technique. The precursors for hydroxyapatite were $Ca(NO_3)_2.4H_2O$ (Merk, India) and $(NH_4)_2HPO_4$ (Nice Chemical, India) and for TZP preparation, $ZrOCl_2.8H_2O$ (Loba,India) and Y_2O_3 (Indian Rare Earth Limited, India) were used. Stock solutions of precursors such as $Ca(NO_3)_2.4H_2O$, $(NH_4)_2HPO_4$ and $ZrOCl_2.8H_2O$ were prepared by dissolving them in deionized water. The concentration of $Ca(NO_3)_2.4H_2O$, $(NH_4)_2HPO_4$ solution were 1 mol/Lit and for $ZrOCl_2.8H_2O$ the solution concentration was 0.75 mol/Lit.

4.1 Quantitative Analysis of $Ca(NO_3)_2$ and $ZrOCl_2$ Stock Solution by Gravimetry:

For the estimation of the above precursors, 3 ml of corresponding stock solution was taken in a clean and dried 250 ml volumetric flask. To the aliquot, 2-3 drops of methyl-red indicator was added and the color changed to pink both for $ZrOCl_2$ and $Ca(NO_3)_2$ solution. The indicator mixed solution was titrated with AAC buffer solution (NH_4OH & NH_4Cl) for $ZrOCl_2$ and with NaOH for $Ca(NO_3)_2$. The complete precipitation of $Zr(OH)_4$ took place between pH of 9-10 and for $Ca(OH)_2$, pH was between 7-8. The end point of the reaction was marked by the change in the solution color from light pink to pale yellow. The white precipitates were warmed and filtered through Whatman 40 filter paper for $ZrOCl_2$ and through Whatman 42 for $Ca(NO_3)_2$. The precipitates were washed with hot water to remove nitrates, chloride and excess AAC buffer solution. The washing was continued till the color of the precipitate changed from pale yellow to colorless. The precipitate along with the filter paper was transferred to a pre-weighed platinum crucible and fired at 1000°C for 1hr in a furnace. The weight of the calcined precipitate on firing was equivalent to weight of the oxide per 3ml of solution. The possible chemical reaction during precipitation could be written as follows:

$$Ca(NO_3)_2 + 2NaOH \rightarrow Ca(OH)_2 + 2NaNO_3 \qquad (4.1)$$

$$ZrOCl_2 + AAC \rightarrow Zr(OH)_4 + 2NH_4Cl \qquad (4.2)$$

The precipitated $Zr(OH)_4$ and $Ca(OH)_2$ could be correlated to their respective oxides according to the following equations:

$$Zr(OH)_4 \rightarrow ZrO_2 + 2H_2O \tag{4.3}$$

$$Ca(OH)_2 \rightarrow CaO + H_2O \tag{4.4}$$

4.2 Powder Synthesis

The hydroxyapatite powder was prepared by two different routes:

(a) Normal precipitation route (NP route)

(b) Reverse strike precipitation route (RS route)

4.2.1 Synthesis of Hydroxyapatite Powder by NP Route

In this method of powder preparation, $(NH_4)_2HPO_4$ solution (1.63 mol/liter) was added dropwise to an equimolar solution of Ca $(NO_3)_2.4H_2O$ along with simultaneous addition of (1:1) NH_4OH solution to make the pH 10.5, resulting in a dense white precipitate. The precipitates were stirred for various time periods (6hrs, 12hrs and 18hr) to optimize the reaction/aging time required for completion of the precipitation reaction. It was found that in this case, overnight stirring (i.e. 12 hours) ensured completion of reaction. The obtained precipitates were washed with water and alcohol. The washed precipitates were dried in a laboratory oven ≤ $100^{O}C$ for 24hrs and the dried precipitate was ground to a fine powder in an agate mortar and pestle. The powder was calcined in air at $850^{O}C$ with a hold for 2 hrs time at the peak temperature. The flow diagram for normal precipitation route is shown in Fig.4.1.

4.2.2 Synthesis of Hydroxyapatite Powder by RS Route

In this process, equimolar solution (1.63 mol/liter) of both $Ca(NO_3)_2.4H_2O$ (Merk, India) and $(NH_4)_2HPO_4$ (Nice Chemical, India) were mixed together to obtain Ca/P ratio 1.67. This was followed by the addition of few drops of (1:1) HNO_3 to get a clear solution. This clear solution was drop wise added to a beaker containing large volume of (1:1) NH_4OH solution maintained pH at 12.5, while the solution is being vigorously stirred. On addition of the mixed solution of Ca $(NO_3)_2.4H_2O$ and $(NH_4)_2HPO_4$ initially the pH dropped from 12.5 to 10.5 and all possible measures were taken to maintain the pH at 10.5

throughout the reaction (by addition of NH_4OH solution if required). However unlike sec 4.2.1, in this case, the stirring was continued for 3 hrs only. The remaining steps of the powder processing by this route were similar to that of normal precipitation route. This precipitation process termed as the reverse strike precipitation process (RS) is thus different from the normal precipitation process route (NP route). (in which NH_4OH is added to the mixed cation solution). The flow diagram for normal precipitation route is shown in Fig.4.2.

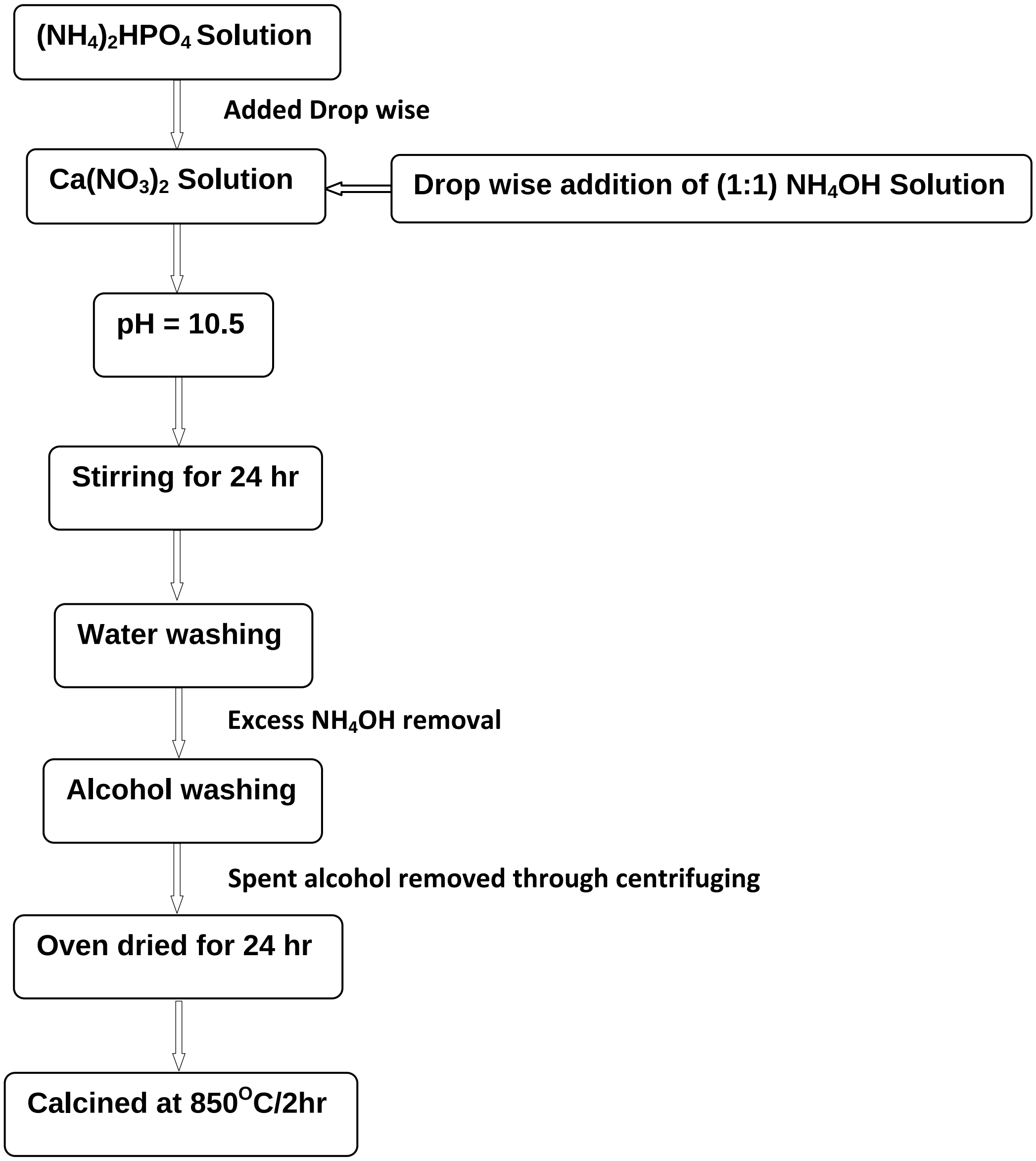

Fig.4.1. Flow diagram for processing of HA powder by NP route

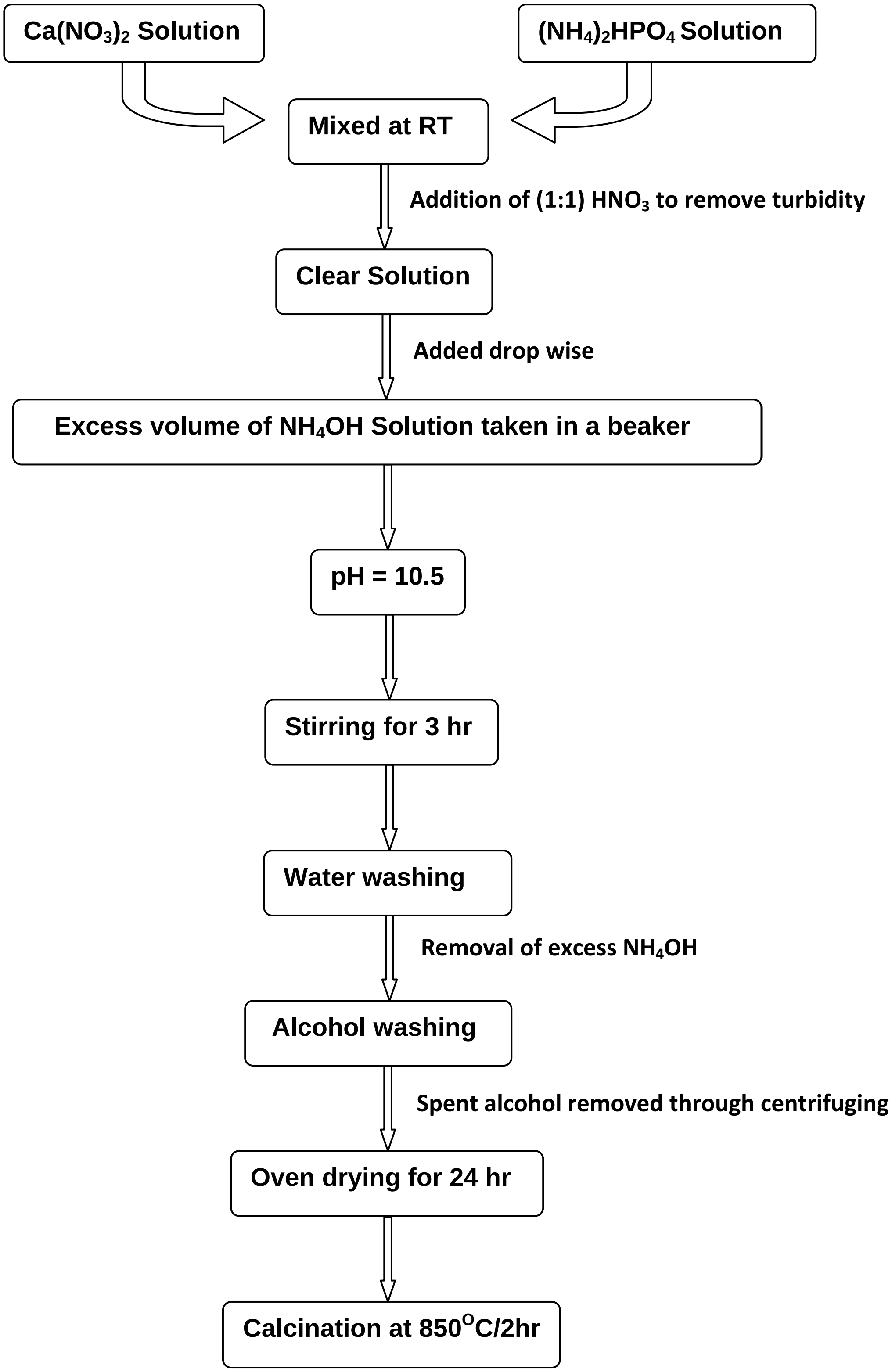

Fig. 4.2. Flow diagram for processing of HA powder by RS route

4.3 Preparation of HA - nano TZP Composite Powder

The HA - nano TZP composite was prepared following the two steps:

(a) Preparation of nano TZP (2.5 mol% Y_2O_3) powder using normal precipitation method and

(b) Preparation of HA - nano TZP composite (containing 2, 5, 7.5 and 10 wt% TZP and denoted as HZ2, HZ5, HZ7, HZ10 respectively) by reverse strike precipitation method.

The flow diagram for the above precipitation route for HA – nano TZP composite is shown in Fig.4.3.

4.3.1 Preparation of nano 3Y-TZP Powder using NP route

The precursors were $ZrOCl_2.8H_2O$ (Loba chemical, India) and Y_2O_3 (Indian Rare Earth Limited, India). The flow diagram for the powder synthesis is shown in Fig.4.3. The concentration of $ZrOCl_2$ solution was 0.75 moles/liter in which requisite amount of Y_2O_3 powder (dissolved in HNO_3) was added. Drop wise addition of (1:1) NH_4OH solution to the mixed solution of $ZrOCl_2$ and $Y(NO_3)_3$ resulted in the precipitation of $Zr(OH)_4$ and $Y(OH)_3$ and the final pH was 10.5. The precipitates were washed to remove chloride ions followed by drying and calcination at $850^{O}C$/2h. Some other batches $Zr(OH)_4$-$Y(OH)_3$ precipitate were also calcined at $1200^{O}C$/2hours.

4.3.2 Preparation of HA - nano TZP Composite (containing 2, 5, 7.5 and 10 wt% TZP) by RS Method

HA - nano TZP composite (hence forth reported as HA-TZP composite) containing different wt% of TZP were prepared by adding requisite amount of TZP i.e. 2, 5, 7.5 and 10 wt% to a large volume of (1:1) NH_4OH solution as shown in Fig.4.3. Possible measures were taken to keep the TZP particle in dispersed state by simultaneous application of ultrasonic energy and mechanical stirring during the subsequent HA precipitation. The mixed precursor solution for HA precipitation ($Ca(NO_3)_2$ + $(NH_4)_2HPO_4$) was drop wise added to the mixed TZP - NH_4OH solution to obtain dense white precipitates (pH 10.5), through simultaneous addition of (1:1) NH_4OH solution (if required). The precipitates were washed with water by decantation method for the removal of excessive ammonia followed by alcohol washing to avoid the agglomeration of HA particles, centrifuging (for solvent removal), drying, grinding followed by calcination at 850°C for 2 hours.

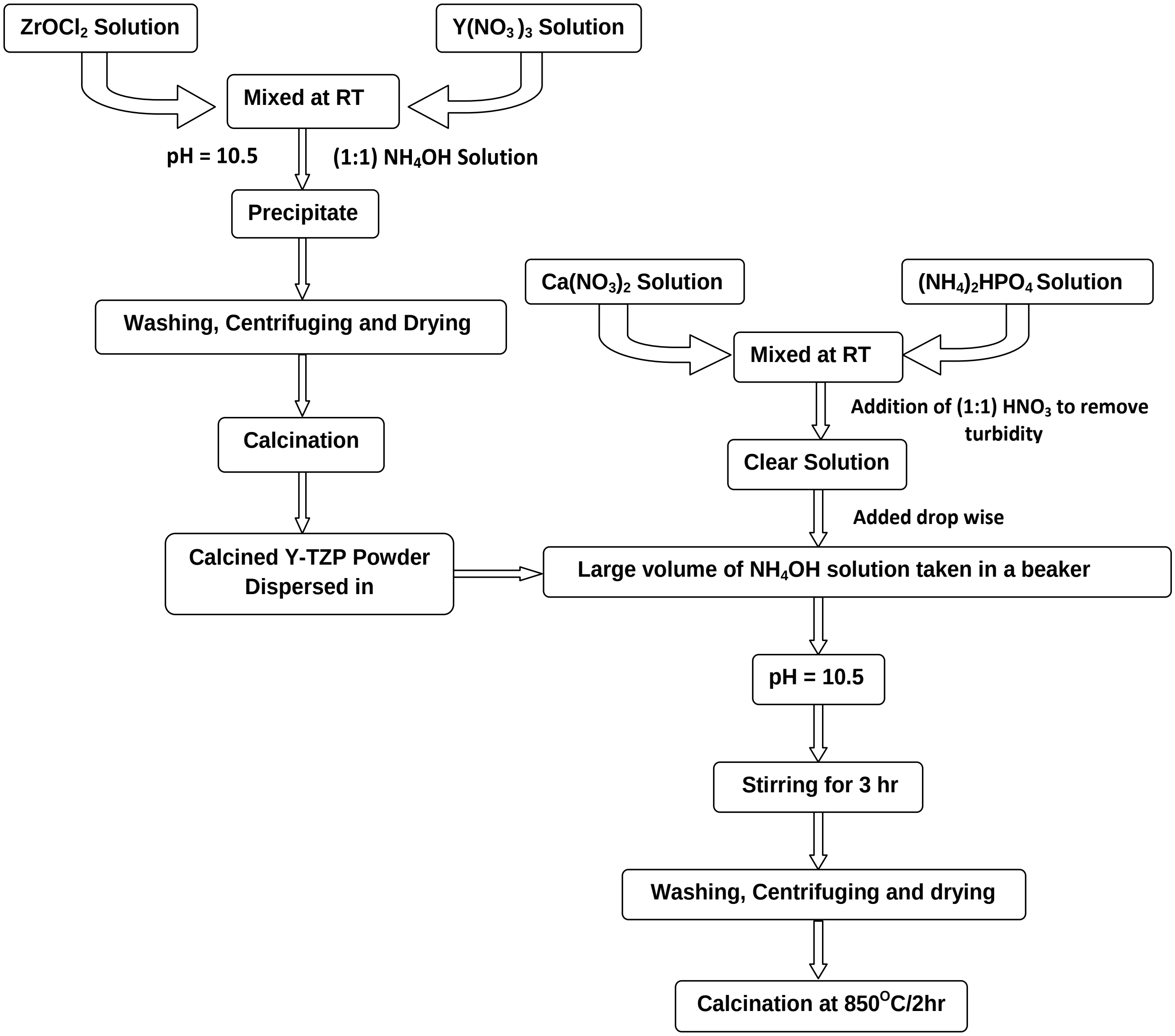

Fig. 4.3. Flow diagram for processing of HA-TZP composite powder by RS route

4.3.3 Calcination:

HA powder prepared by both NP (section 4.2.1) and RS route (section 4.2.2) as well as powder of HA-TZP composite were calcined at different temperature ranging from 650-950^{O}C with 2 hours holding time at the peak temperature.

4.4 Characterization of Dried Precipitate and Calcined Powder:

The dried precipitate was characterized for its thermal decomposition behaviour through DSC/TG, identification of the functional group present in raw as well as calcined powder (calcined at different temperatures between 650-950^{O}C for 2 hrs) through FTIR spectroscopy. The phase analysis and crystallite size of both the raw as well as calcined powder (as a function of calcination temperature) was carried out by XRD. Particle size and the morphology of the calcined powder were studied by TEM. BET surface area of the calcined powder was measured using BET (Brunauer-Emmett-Teller) powder surface area analyzer.

4.4.1 DSC/TG of Dried Precipitate:

The thermal analysis of the dried precipitate was carried out by DSC/TG (Netzsch STA/409 C) in an ambient atmosphere at a heating rate of 10^{O}C/ minute using α-Al_2O_3 as reference material. A small quantity of finely ground dried precipitate was used. This DSC/TG provided the information about the decomposition and crystallization behaviour of hydroxides.

4.4.2 FTIR Spectroscopy of as Precipitated and Calcined Powders:

The functional groups present and nature of ions adsorbed on the dried precipitate as well as calcined powder was studied through FTIR. The powder sample was mixed with requisite amount of KBr in an agate mortar and pressed into 0.1mm thickness pellet. A transmittance mode spectra was taken in a Perkin Elmer FTIR Spectrophotometer (Model 84005) in the wave number range 4500-450 cm^{-1}.

4.4.3 Phase Analysis of Dried Precipitate and Calcined Powder:

Phase analysis of dried precipitate and calcined powder was done by X-ray diffractometer (Phillips PW 1830, Holland). The radiation was Cu-Kα (λ = 1.542), filtered with Ni filter. The samples were scanned in the 2θ range 20-80 ° at a scan rate of 2°/min. Some of the samples were also step scanned at a slow scan rate of 0.35°/min in the 2θ range 26-34 ° for resolving of overlapping peaks. The accelerating voltage and current were 35kV and 30mA respectively. The crystallite size of the powder was measured from X-ray line broadening using Scherrer's formula [4.1, 4.2].

$$D = \frac{0.9\lambda}{B\cos\theta} \tag{4.5}$$

Where, **D** is the crystallite size, λ is the wavelength of the radiation, θ is the Bragg's angle and **B** is the full width at half maximum

$$B^2 = B^2_{meas.} - B^2_{inst.} \tag{4.6}$$

Where, B_{meas}= Observed full width at half maximum from peak values

$B_{inst.}$ = Instrumental broadening.

The fraction of crystalline phase (X_c) in calcined HA powder was calculated from the following equation

$$X_c \sim (1-(V_{112/300})/I_{300}) \tag{4.7}$$

Where $V_{112/300}$ is the intensity of hollow between (112) and (300) diffraction peaks. I_{300} is the is the intensity of (300) diffraction peak [4.1,4.3].

The relative x-ray intensity of various phases present was determined using 100% peak intensity of each phase by the following equation 4.8 [4.4, 4.5].

$$V_r = \frac{I_r}{(I_{vt} + I_{vh} + I_{vcz} + I_{vbtcp} + I_{vatcp})} \tag{4.8}$$

where I_{vt} , I_{vh} , I_{vcz}, I_{vbtcp} and I_{vatcp} are the strongest peak intensity (100% peaks) of different phases (e.g. TZP, HA, $CaZrO_3$, α-TCP and β-TCP) and I_r being the intensity of the required phase. The same parameters were also used for sintered and hot pressed samples.

4.4.4 Surface Area of Calcined Powder:

The BET surface area analyzer (Quantachrome Instruments, U.S.A.) was used to measure the specific surface area of the calcined powder. The instrument operates on liquid nitrogen adsorption and desorption by the powder surface. The degassing of the calcined powder was carried out at 100°C and surface area was measured from five point analysis technique. The BET equation for specific surface area (S) is given as:

$$S = S_t / w \qquad (4.9)$$

where S_t = total surface area and w = sample weight

$S_t = W_m N A_{cs} / M$

W_m = Weight of the monolayer

N = Avogadro's number

A_{cs} = Molecular cross sectional area of the adsorbate

M = molecular weight of the adsorbate

The average particle size (d_{BET}) was calculated from surface area according to Equation (4.10) [4.6, 4.7]. The average particle size is the diameter of the spheres equivalent to surface of powder.

$$d_{BET} = \frac{6}{S_p \rho} \quad \text{(spherical approximation)} \qquad (4.10)$$

d_{BET} = average particle diameter, S_p = specific surface area (m^2/gm); ρ= true density of the material.

4.4.5 Particle Size Distribution:

The particle size (or the agglomerate size) and its distribution of the calcined HA-TZP powder was calculated by dynamic light scattering technique (Malvern MASTER SIZER, U.K.). The refractive indexes of the powders, dispersant and medium are important parameters in defining the scattering behaviour of LASER by the particle. Therefore, the refractive index and bulk density of both the medium and samples were determined before carrying out the particle size distribution. The true density of the powder was measured by Pycnometer using kerosene as medium. The powder was ultrasonically dispersed in water. The D_{50} was determined from the size frequency curve calculated on the basis of the surface to volume ratio of particle.

4.4.6 Morphology of Calcined Powder:

The particle size and its distribution, morphology of the calcined powder along with its agglomeration tendency were studied by TEM (Philips CM 200). The TEM sample was prepared done by dispersing a small amount of powder in acetone using 20 kHz, 500W ultrasonic energy for 30min. A drop of the well-dispersed suspension was deposited on to a carbon coated copper grid (400 mesh) followed by drying the grid for the evaporation of solvent. The powder was observed in bright field at an accelerating voltage of 150 KV.

4.4.7 Densification behaviour:

The nonisothermal sintering behaviour of HA-TZP composite was carried out by constant rate heating method. Green rectangular bars of HA-TZP composites were sintered till 1300^{o}C in ambient atmosphere at a heating rate of 5^{O}C/min in a dilatometer (NETZSCH DL 402C).

4.5 Sintering of HA and HA-TZP Composites:

4.5.1 Sintering in Air:

Sintering of green compacts was carried out `in a chamber furnace (45R5Y) by heating it from room temperature to 650^{0}C at a heating rate of 3^{0}C/minute with a holding time of 30 minute at 650^{0}C for binder removal. Thereafter, the heating was continued at the rate of 3^{0}C/minute till the final sintering temperature (1250^{0}C) was attained. A holding time of 4hours was provided at the peak sintering temperature. Following the sintering, the samples were furnace cooled to room temperature.

4.5.2 Hot Pressing

The HP experiment was carried out in a vacuum hot press (M/s Materials Research Furnace, Suncook, USA). The HA-TZP powders were filled in a high density graphite die (outer diameter 80 mm, internal diameter 40 mm and height 70 mm). The assembly of graphite die in the hot press is shown schematically in Fig. 4.4. A flexible graphite sheet was used to cover the internal surface of die, to avoid contact between powders and die wall. The samples were hot pressed in vacuum at 950^{O}C at a constant load of 30 MPa with a holding time of 30 minute as schematically represented in Fig. 4.5. An oil pressure of 1020 psi was generated to apply 30 MPa pressure on the sample. A W 5%Re – W 26%Re molybdenum sheathed thermocouple was placed near the graphite die connected to a programmable temperature controller to measure the temperature of the furnace chamber.

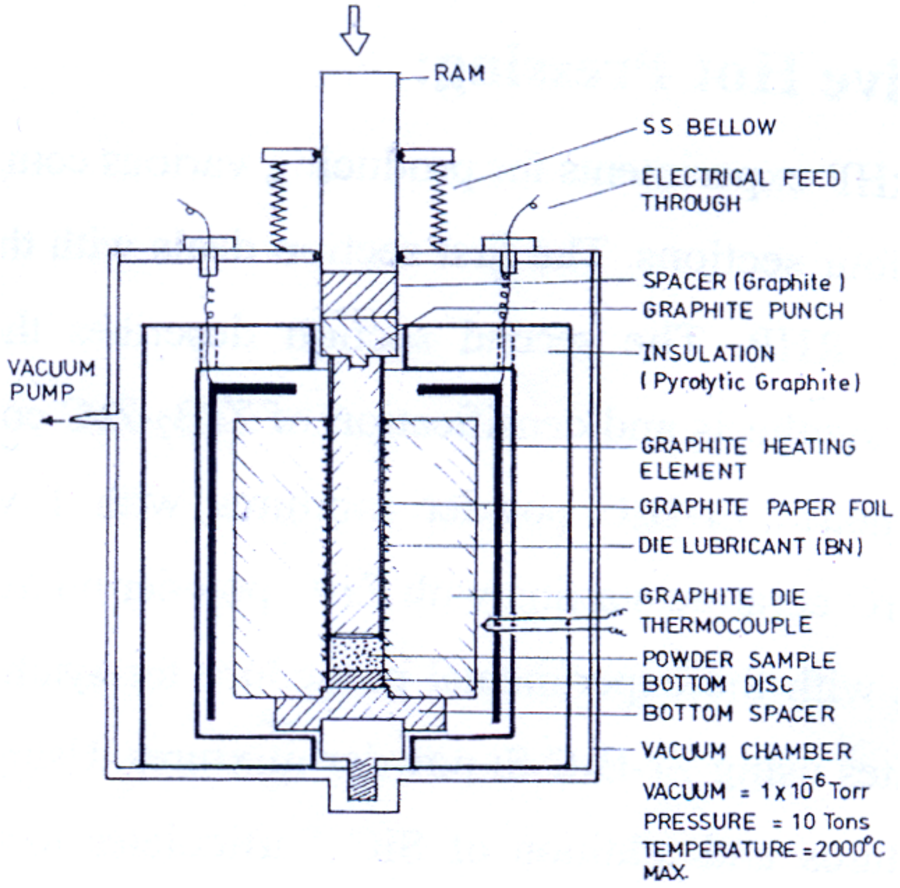

Fi g. 4.4. Schematic diagram of Hot Press

Pressure was applied from 850^{O}C onwards and the peak pressure was achieved at 950^{O}C. The heating rate was controlled by the vacuum level of the furnace chamber. Faster heating rate caused more degassing from the powder and die assembly and the vacuum level was reduced resulting in switching off the furnace power.

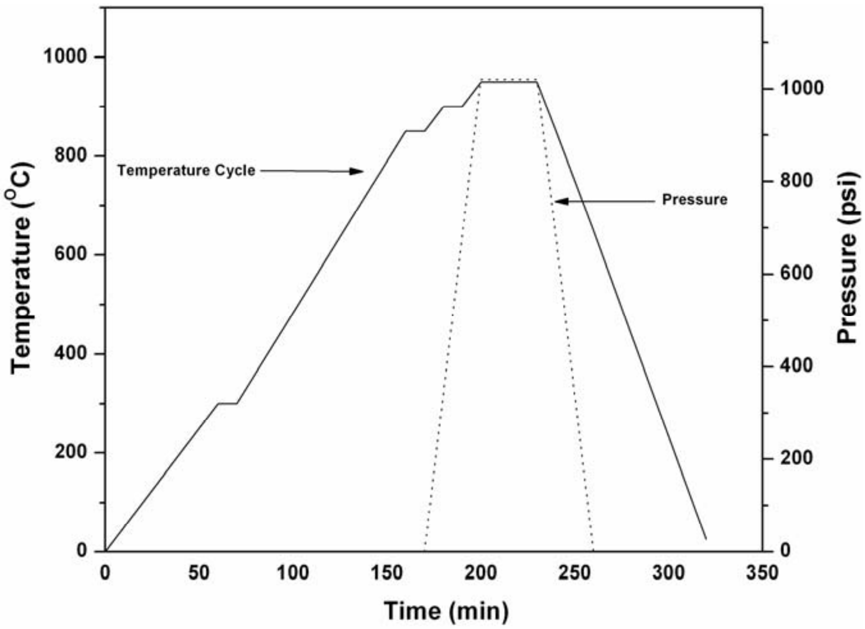

Fig. 4.5. Temperature and pressure sequence during hot pressing

4.6 Characterization of Sintered and Hot Pressed Samples:

The sintered pellets were studied for density and phase analysis along with strength, toughness, hardness and wear behavior as well as micro structural characterization SEM and FESEM.

4.6.1 Bulk Density and Apparent Porosity of Sintered and Hot Pressed Specimen:

The bulk density and apparent porosity of the sintered and hot pressed pellets were measured by Archimedes principle using kerosene as the immersion liquid. The dry weight of the specimen was measured and the soaked weight was taken after immersion of the specimen in liquid followed by evacuation so that kerosene fills up the entire open pores in the specimen. The vacuum was continued till the bubbles were coming out of the samples. Similarly, the suspended weight of the specimen was also measured while keeping the specimen suspended in the liquid.

The bulk density and the apparent porosity were calculated using the suspended and soaked weight.

$$Bulk\ Density = \left(\frac{W_d \times Density\ \ of\ Kerosene}{W_{sk} - W_{su}} \right) \times 100 \tag{4.11}$$

$$Apparent\ Porosity = \left(\frac{W_{sk} - W_d}{W_{sk} - W_{su}} \right) \times 100 \tag{4.12}$$

where W_d, W_{su} , W_{sk} represent dry weight, suspended weight and soaked weight of the sample respectively.

The relative sintered density of HA and HA-TZP composites were determined from the ratio of bulk density and the literature value of theoretical density for these compositions [4.8, 4.9].

4.6.2 Microstructure of Sintered Specimens:

Sample Preparation:

The sintered samples were gently polished with diamond paste on a glass plate. This was further polished on textmet cloth with lubricating oil. The polished samples were rinsed with water, acetone and cleaned in an ultrasonic bath for 10 minutes. The polished and clean samples were chemically etched for 5 minutes in 0.01M lactic acid solution. The etched samples were thoroughly washed with water and acetone to remove any traces of etchant present. Following this, the samples were dried and thermally etched for 20 minutes at 1100^{O}C. However, the hot pressed samples were thermally etched at 920^{O}C for 20 minutes.

SEM Imaging:

The polished and thermally etched samples were sputter coated with palladium-platinum for 2.5 minutes in order to make the surface conducting. The specimens were observed by SEM (JEOL- JSM 6480 LV) and FESEM (SIRION, high resolution FEI) both in BSE and SE mode at an accelerating voltage of 15KV and 10KV.

4.6.3 Mechanical Characterization:

Strength, toughness and hardness of sintered compacts were measured on rectangular samples (45x4x4 mm^3). All the six sides were polished and the edges were also chamfered. The fracture strength was measured in three point bent as well as in diametral compression. The diametral compression test was measured on cylindrical pellet (2-4 mm thickness and 10-12 mm dia.). The fracture toughness was measured by SENB method on notched and indented samples in three point bending. [4.10 - 4.15].

Flexural Strength:

The flexural strength was determined in three point bending in a Materials Testing Machine (H10KS, Tinus Olsen, U.K) using a span length of 40 mm for pressureless sintered and 25 mm for hot pressed sample at cross head speed of 0.2mm/sec. The edges of the rectangular bars were ground with 800grit SiC paper to obtain a parallel and smooth surface. The flexural strength was calculated from the following equation [4.10, 4.11].

$$\sigma_{flexural} = \left(\frac{3PL}{2WD^2} \right) \tag{4.14}$$

where P = maximum load; L = Span length; W = width of the sample; D = depth or thickness of the sample

Biaxial Flexural Strength:

The biaxial flexural strength was determined in a Materials Testing Machine (H10KS, Tinus Olsen, U.K) on circular pellets (10 mm diameter) using Brazilian Disc Test method. The samples were kept between the compression platen and were broken at a cross head speed of 0.2 mm/sec. The strength was calculated from the formula [4.12].

$$\sigma_{biaxial \quad flexural \quad strength} = \frac{2P}{\pi Dt} \tag{4.15 }$$

where, P is the breaking load, D is the pellet diameter and t its thickness.

Fracture Toughness:

The fracture toughness was determined by SENB method on notched and indented samples [4.13]. A notch depth of 0.3-0.5 of sample depth was made at the center of sample by a slow speed diamond saw (Buehler). A sharp crack was introduced at the notch tip by indenting the notched sample at 5N load. The fracture toughness K_{IC} was calculated from the following equation [4.14].

$$K_{IC} = \frac{3P\,L\,C^{1/2}}{2W\,D^{2}}\left[A_0 + A_1\left(\frac{C}{D}\right) + A_2\left(\frac{C}{D}\right)^2 + A_3\left(\frac{C}{D}\right)^3 + A_4\left(\frac{C}{D}\right)^4\right] \qquad (4.16)$$

where, P = breaking load, C= notch depth, W = width of the sample, L = span length and D = depth or thickness of the sample. A_0, A_1, A_2, A_3 and A_4 are the constants and their values are calculated as following:

$$A_0 = 1.9 + 0.0075(L/D)$$

$$A_1 = -3.39 + 0.08(L/D)$$

$$A_2 = 15.4 - 0.2175(L/D)$$

$$A_3 = -26.24 + 0.2815(L/D)$$

$$A_4 = 26.38 - 0.145(L/D)$$

Vickers Hardness:

The Vickers hardness was tested in a Semi Macro Hardness Tester (Leco, LV700). The polished samples were indented at three different loads, viz. 3, 5, 10 kgf for 10 seconds. Higher loads were avoided because they resulted in extensive cracking from the diagonal corner. A plot was made between half diagonal lengths of the indent against indentation load. The hardness was calculated from slope of the plot using the following relation. [4.15].

$$H_v = 0.47 \times \frac{P}{a^2} \qquad (4.17)$$

where, H_V is the Vickers hardness (GPa), P is applied load (N) and a is the half of the diagonal length (μm).

4.6.4 In-vitro Bioactivity Test of HA and HA-TZP Composite:

The *In-vivo* bioactivity test was carried out by soaking the sample in SBF (simulated body fluid) for 5 and 10 days respectively in an incubator maintained at $37.5^{O}C$. The reagent used for SBF preparation is given in Table 4.1 were NaCl (Merck, India, 99.5%), $NaHCO_3$ (Merck, India, 99.5%), KCl (Merck, India, 99.5%), $Na_2HPO_4 .2H_2O$ (Merck, India, 99.5%), $MgCl_2.6H_2O$ (Merck, India, 99%), $CaCl_2.H_2O$ (Merck, India, 99.5%), Na_2SO_4 (Merck, India, 99.5%), $(CH_2OH)_3CNH_2$ (Merck, India, 99.8%) and 1M HCl (Merck, India). 1000 ml SBF solution was prepared by dissolving the reagents in required amount individually and in the sequence mentioned to 700ml of deionized water (Table 4.1 , Fig. 4.6) taking care that a new reagent in the sequence was added only after the previous reagent has completely dissolved. The above solution was subsequently titrated with 1M HCl to a pH 7.4 at $37^{O}C$. The obtained solution could be stored in an air tight container at $5^{O}C$ for about a month [4.16].

Table 4.1 Composition of SBF solution

Order	Reagent	Amount (gm/lit)
1	NaCl	6.547
2	$NaHCO_3$	2.268
3	KCl	0.373
4	$Na_2HPO_4 . 2H_2O$	0.178
5	$MgCl_2 . 6H_2O$	0.305
6	$CaCl_2 . 2H_2O$	0.368
7	Na_2SO_4	0.071
8	$(CH_2OH)_3CNH_2$	6.057

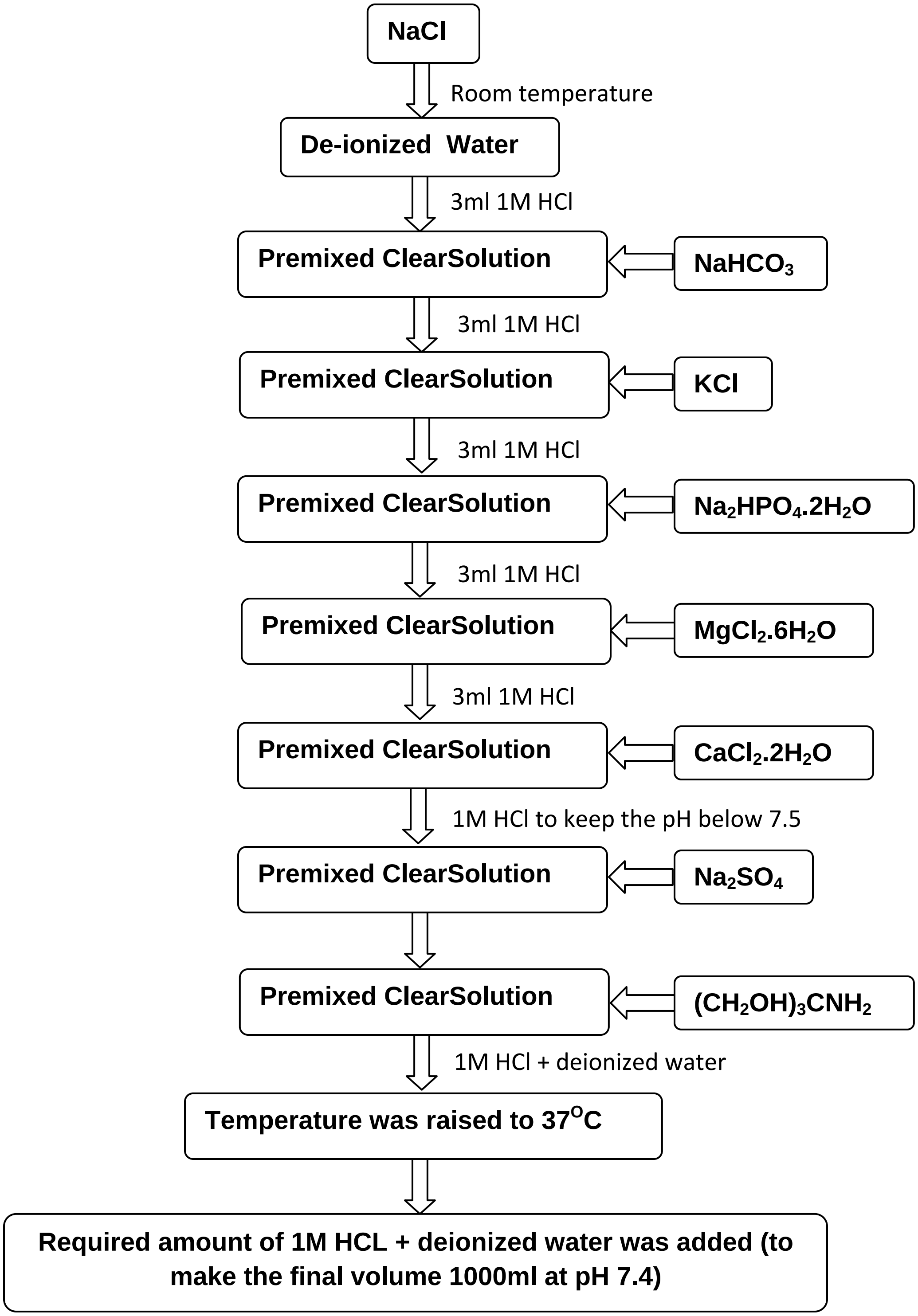

Fig.4.6. Flow diagram for SBF synthesis [4.15].

4.6.5 In-vitro Cytotoxicity Test of HA and HA-TZP Composite

The *in- vitro* cytotoxicity test was performed by indirect Agar Diffusion method on strips (3mm x 4mm x 1mm) of HA as well as HA-TZP composite (as per ISO 10993-5) after 24 hours of contact. Modified Eagle Medium (MEM), supplemented with Foetal Bovine Serum as the culture medium and L929 mouse fibroblast cells were used. Test samples, positive controls (stabilized PVC Disc) and negative controls (High Density Poly Ethylene (USP)) in triplicate were placed on 1.5% agar overlayed on subconfluent monolayer of L-929 mouse fibroblasts. Cells were incubated with test samples at 37 ± 1^{O}C for 24 to 26 hours. The cultured cells were incubated with neutral red solution (50 mg% in saline). Microscopic examination of cytotoxicity was done to study the cellular response around and under the samples. The cytotoxicity reactivity are graded as 0, 1, 2, 3 and 4 on the basis of zone of lysis around and under the sample, general morphology and vacuolization as given below.

Table 4.2 Grading of cytotoxicity reactivity

Grade	Reactivity	Description of reactivity zone
0	None	No detectable zone around or under specimen
1	Slight	Some malformed or degenerated cells under specimen
2	Mild	Zone limited to area under specimen
3	Moderate	Zone extending specimen size up to 0.33 cm
4	Severe	Zone extending farther than 0.33 cm beyond specimen

The quantitative evaluation of the sample was done by grading positive and negative control as 4 (severe cytotoxic) and 0 (none cytotoxic) respectively.

4.6.6 In-vitro Hemocompatibilty of HA and HA-TZP Composite

The In-vitro hemocompatibility test of HA as well as HA-TZP composite was carried out by collecting blood from human volunteer into an anticoagulant, ACD. Following this the test specimens were placed in polystyrene culture plates with phosphate buffered saline and agitated before being exposed to blood. 2 ml of blood was added to each plate, out of which 1 ml was immediately collected for analysis and another 1 ml was exposed to the material for 30 minutes. Simultaneously the solution was agitated at 75 ± 5 rpm using an Environ shaker thermo stated at 35 ± 2^0C (WPTRU012). As a reference four empty polystyrene culture dishes were also exposed with blood. Platelet poor plasma (PPP) was derived from the blood sample by centrifuging it at 4000 rpm for 15 minutes as per WPTRV006.

The percentage hemolysis was determined by the formula:

$$\% \text{ hemolysis} = (\text{Free Hb}/\text{Total Hb}) \times 100 \qquad (4.18)$$

where, Hb is the total hemoglobin in the whole blood samples (measured by automatic haematology analyser (Sysmex-K 4500) as per WPTRU015. Similarly, Free Hb is the measure of liberated free hemoglobin liberated into the plasma after exposure (measured using Diode array Spectophotometer as per WPTRV022).

References:

4.1 I. Smiciklas, A. Onjia and S. Raicevic, “Experimental design approach in the synthesis of hydroxyapatite by neutralization method”, Separation and Purification Technology, 44, 97-102 (2005).

4.2 N. Y. Mostafa, “Characterization, thermal stability and sintering of hydroxyapatite powders prepared by different routes”, Materials Chemistry and Physics, 94 (2-3), 333-341 (2005).

4.3 N. Rameshbabu, K. Prasad Rao and T. S. Sampath Kumar, “Acclerated microwave processing of nanocrystalline hydroxyapatite”, 40, 6319-6323 (2005).

4.4 D. K. Pattanayak, R. Dash, R.C. Prasad, B.T. Rao and T.R. Rama Mohan, “Synthesis and sintered properties evaluation of calcium phosphate ceramics”, Materials Science and Engineering C, 27, , 684-690 (2007).

4.5 R. R. Rao and T. S. Kannan, “Synthesis and sintering of hydroxyapatite-zirconia composites”, Materials Science and Engineering C, 20, 187-193 (2002).

4.6 V.V. Silva and F.S. Lameiras, “Synthesis and characterization of composite powders of partially stabilized zirconia and hydroxyapatite”, Materials Characterization, 45, 51-59 (2000).

4.7 V.V Silva, F. S. Lameiras and R. Z. Domingues, “Synthesis and characterization of calcia partially stabilized Zirconia – hydroxyapatite powders prepared by co-precipitation methods”, Ceramic international, 27, 615-620 (2001).

4.8 M. F. Ashby, “Criteria for selecting the components of composites”, Acta metall. mater., 41, , 1313-1335 (1993).

4.9 Z. Evis, M. Usta, I. Kutbay, “Improvement in sinterability and phase stability of hydroxyapatite and partially stabilized zirconia composites”, Journal of European Ceramic Society, 29, 621-628 (2009).

4.10 ASTM C1161-90, Standard test method for flexural strength of advanced ceramics at ambient temperature, Annual Book of ASTM Standards, Vol. 15.01. ASTM, pp. 327-333 (1991).

4.11 K. A. Khalil, S. W. Kim and H. Y. Kim, “Consolidated and mechanical properties of nano structured hydroxyapatite- (ZrO_2 + 3mol% Y_2O_3) bioceramics by high- frequency induction heat sintering”, Materials Science and Engineering A, 456, 368-372 (2007).

4.12 A.T. Procopio, A. Zavaliangos and J.C. Cunningham, “Analysis of the diametrical compression test and the applicability to plastically deforming materials”, J. Mat. Sc. 38, 3629-3639 (2003).

4.13 ASTM: C-1421-99, Standard test method for determination of fracture toughness of advanced ceramics at ambient temperature, pp.1-32 (1999).

4.14 D. R. Larson, J.A. Coppola, D.P.H. Hasselman and R.C. Bradt, “Fracture Toughness and spalling behavior of high-Al_2O_3 refractories”, J.Am.Ceram.Soc, 57, 417-421 (1974).

4.15 ASTM: C1327-99, Standard test method for Vickers indentation hardness of advanced ceramics, pp.1-8 (1999).

4.16 A.C. Tas, “Synthesis of biomimetic Ca-hydroxyapatite powders at $37^{O}C$ in synthetic body fluids”, Biomaterials, 21, 1429-1438 (2000).

Chapter V

Results and discussions-

Processing, Densification Behavior, Mechanical Properties of HA and HA-TZP Composites

Section A

Processing and Characterization of Hydroxyapatite

5.1 Preparation of HA powder by NP and RS Routes

HA powder was synthesized by two different routes; NP and RS as elaborately discoursed in the experimental section (Section 4.2). The following sections deal with the characterization of as synthesized HA powder and sintered pellets. On the basis of the observations made and the results obtained subsequently only one route was chosen for the preparation of HA-TZP composite.

5.1.1 Thermal Analysis of Dried HA Powder

The DSC/TG plot of the as precipitated powder prepared by NP route (Fig. 5.1) shows a total weight loss of about 12.1% with respect to the initial weight in the temperature range 100-1250°C. The powder recorded 9.5% weight loss between 100-400°C associated with a sharp endothermic peak in the DSC curve. This is attributed to the partial removal of physically absorbed water and excess lattice water. The removal of these OH^- groups affects the stochiometry as well as the crystallinity of HA. This transformation behaviour is consistent with FTIR result. The OH^- band at $3500 cm^{-1}$ becomes narrower with increasing calcination temperature. The removal of excess lattice water transforms poorly crystallized HA to well crystallized HA.

$$10\ Ca(NO_3)_2.4H_2O + 6\ (NH_4)_2HPO_4 + 8\ NH_4OH \longrightarrow Ca_{10}(PO_4)_6(OH)_2 + 20\ NH_4NO_3 + 46H_2O \quad (5.1)$$

A weight loss of 1.65% occurs in the temperature range 400-1250°C, which is associated with broad endothermic peak in the DSC curve, corresponds to the 1.75% weight loss required for the decomposition of stochiometric HA to β TCP or $Ca_3(PO_4)_2$ as per the chemical equation given below. This is in consistent with the XRD results.

$$Ca_{10}(PO_4)_6(OH)_2 \longrightarrow Ca_3(PO_4)_2 + CaO + H_2O. \quad (5.2)$$

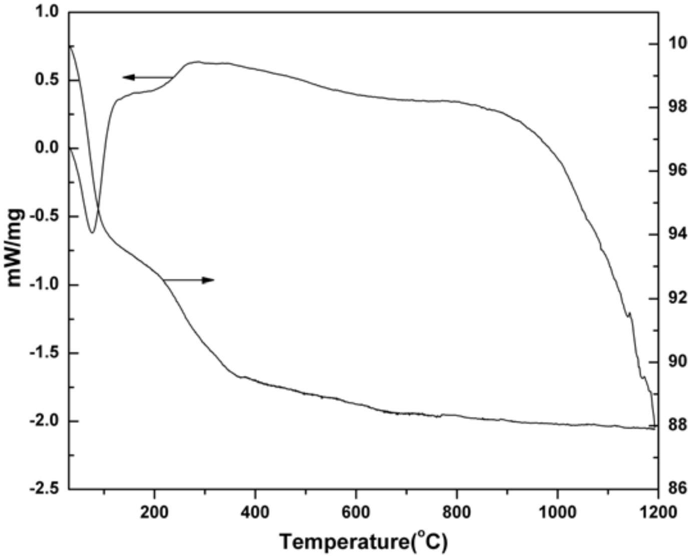

Fig.5.1. DSC/TG curve of HA powder synthesized by NP route

On the other hand the DSC/TG graph of the as precipitated powder by RS route (Fig. 5.2) shows only a small endothermic peak at around 100°C and no other distinguishable exothermic or endothermic peak could be observed up to 1250°C. The small endothermic peak at 100°C is due to the removal of free unbonded water. The absence of any other peak till 1250°C indicates the thermal stability of the powder [5.2]. The TG curve also shows a negligible weight loss throughout the entire range of temperature studied except for the loss around 100°C .The broad like exothermic peak around 350-400°C without any associated weight loss is due to crystallization of disordered HA from the amorphous powder.

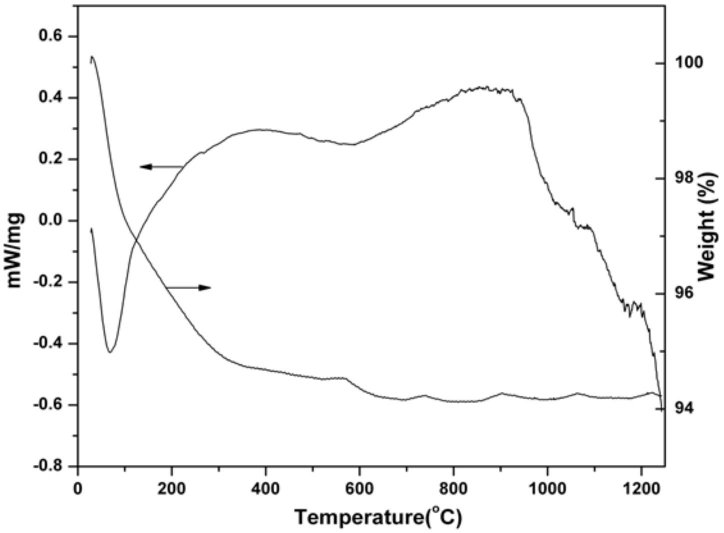

Fig.5.2 .DSC/TG curve of HA powder synthesized by RS route

Further, the DSC/TG curve of RS-HA powders shows a broad exothermic peak in the temperature range 800^{o}C-1000^{o}C. This exothermic peak is not associated with any weight loss. Therefore, the peak should correspond to phase changes/ordering in HA and/or ZrO_2. In order to validate the DSC curve, the position of the first three peaks of HA (or triplets) (d= 2.81A^{o}, 2.72 A^{o}, 2.78 A^{o} respectively) were monitored as a function of calcination temperature. The results are shown in Fig. 5.3, where the left hand pattern (Pattern A) shows the complete XRD profile of HA, and the right hand pattern (Pattern B) is the "zoomed in" pattern of the same in the 2θ range 30-35^{o}.

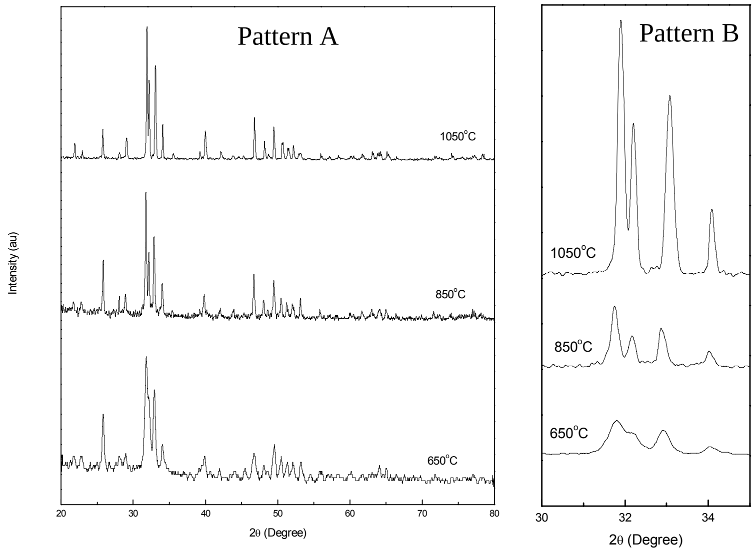

Fig.5.3. XRD pattern of HA powder calcined at 650^{0}C, 850^{0}C, 1050^{0}C/2 hours, and the expanded region of XRD pattern showing the peak shifting of HA.

It is clear from pattern B that at 650^{o}C the triplets of HA are not well separated and only 2 peaks (viz d = 2.81A^{o}, 2.72A^{o}) are distinguishable. With increase in calcination temperature to 850^{o}C, besides the above two, a third peak (as split peak) appears at d= 2.78A^{o}. Finally, at 1050^{o}C, all the three peaks of HA (d = 2.81A^{o}, 2.72 A^{o}, 2.78 A^{o} respectively) could be clearly distinguished. It could also be seen from the zoomed in pattern (pattern A), that the HA peak positions shift towards lower 'd' value and both the peak intensity as well as peak sharpness increase. Thus we can infer that at 650^{o}C, HA is poorly crystallized (disordered state) and it becomes perfectly crystalline at 1050^{o}C. This phase change from poorly crystallized HA to perfectly crystalline HA shows up as a broad exothermic peak in the temperature 800^{o}C-1000^{o}C. Further, the very small weight loss (1.98 %) during the heating of the as prepared powder suggests better crystallinity of the as prepared powder. The above observation suggests that HA synthesized by RS route is highly crystalline and is thermally stable up the 1250^{o}C.

5.1.2 FTIR Study of HA Powder:

The FTIR spectrum of (Fig. 5.4) calcined RS powder (850^{o}C/2 hour) shows a broad peak between 3750 and 2900 cm^{-1} which corresponds to the stretching vibration of hydrogen bonded O-H group of HA and water. A sharp peak at 3575 cm^{-1} indicates the free O-H group present at the surface of the crystalline HA. The small peak at 1636 cm^{-1} could be attributed to the bending vibration of water. In the RS-HA powders, absence of any strong band at 1430 and 870 cm^{-1} indicates that $CO_3{}^{2-}$ groups are not present at 850^{0}C. The three strong peaks around 1060 cm^{-1}, 570 and 606 cm^{-1} contributes to P-O vibrations. However, the FTIR (Fig. 5.4) of calcined (850^{o}C/2 hour) NP HA shows sharp peak at 1400 cm^{-1} and 1456 cm^{-1} respectively suggesting the presence of $CO_3{}^{2-}$ group .The remaining peaks in 1450-1700 cm^{-1} range correspond to Ca-O phase. The broad nature of the peak in the range 3750-2900 cm^{-1} and the absence of a sharp peak at 3575 cm^{-1} indicate that free O-H group are absent. The peak at 1060 cm^{-1} confirms the presence of β-TCP at 850^{o}C.The XRD graph also shows a small peak of β-TCP at 850^{o}C.

.

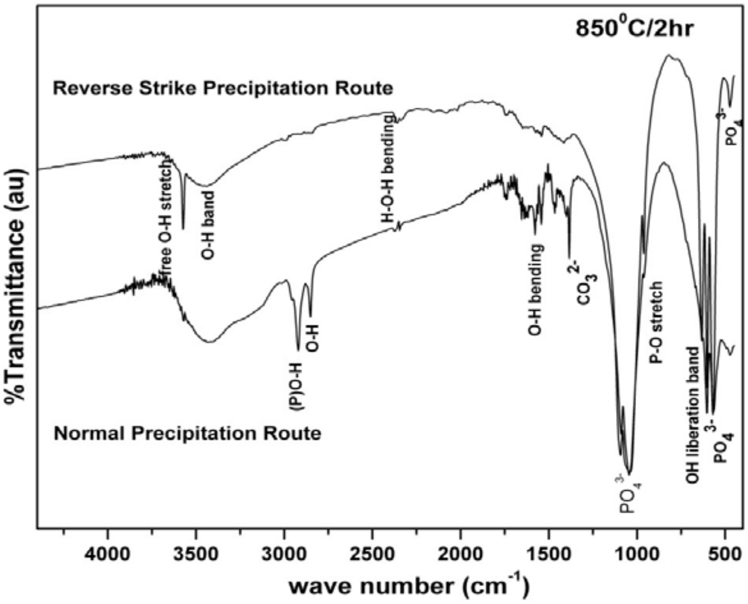

Fig.5.4. FTIR spectra of HA synthesized by NP and RS route

Figure 5.5 shows the FTIR analysis of HA powder prepared by RS route as function of calcination temperature. The decrease in peak broadness between 3750 and 2900 cm^{-1} with increase in calcination temperature indicates the removal of H_2O as shown in the Figure 5.5.

In the raw powder, a small peak at 1459 cm^{-1} corresponds to small amount of CO_3^{2-} present in the calcined powder. The peak disappears on calcining the raw powder at 850^0C. Such CO_3^{2-} peaks usually result from the interaction of atmospheric CO_2 with the trace impurities present in the starting material during powder synthesis in a highly alkaline medium [5.1]. The band at 570, 606 cm^{-1} corresponds to the bending mode of $(PO_4)^{3-}$ and the strong absorption peaks at 1060 cm^{-1} and 963 cm^{-1} respectively are due to the vibration of $(PO_4)^{3-}$ group. The peak at 630 cm^{-1} is attributed to the hydroxyl vibration mode. The triplet at 570, 606 and 630 cm^{-1} along with the absorption band at 472 cm^{-1} indicates that phase pure HA has been synthesized (Table 5.1). This is further confirmed by the XRD analysis where no additional peak other than HA were detected.

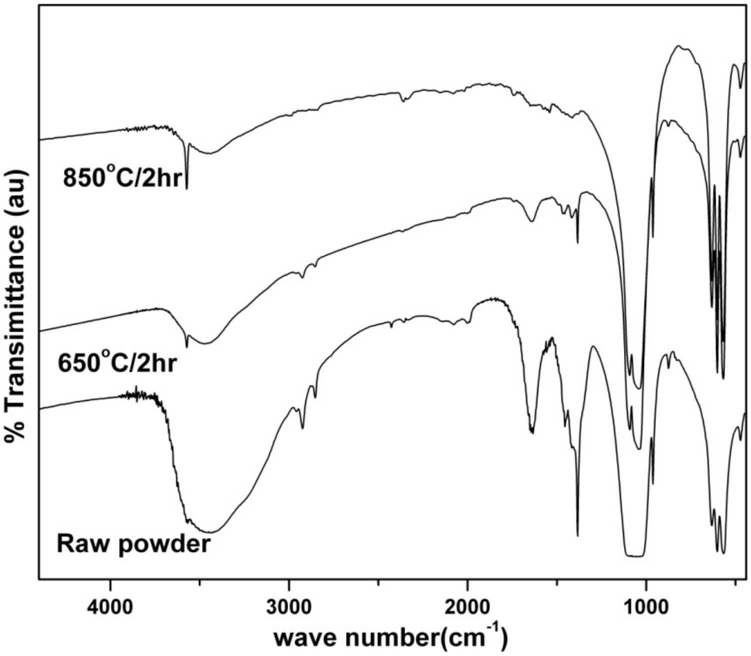

Fig.5.5. FTIR spectra of HA synthesized by RS route as function of calcination temperature

Table 5.1 FTIR spectra of powder prepared by RS route

Adsorption Peak (cm^{-1})	Nature of Peak	Identification
2900-3750	stretching vibration	O-H bonding
3575	sharp peak	free OH
2370	weak stretching	Cl^-
1459	weak peak	CO_3
1060, 963	strong band	P-O vibration
630	weak bending	O-H vibration
606, 570, 472	sharp peak	P-O bending

5.1.3 Particle Size Distribution and TEM Analysis of Calcined HA Prepared by both NP and RS route

Figure 5.6 and 5.7 shows the particle size distribution of the calcined (850^oC/2 hours) HA powder prepared by both the routes. The average agglomerate sizes (D_{50}) of HA powder prepared by RS route and NP route are 42.5μm and 3.61μm respectively. A wide particle size distribution could be seen for both the cases. The particle size of NP route in Fig. 5.7 shows a multimodal distribution and that of RS route shows monomodal type of distribution (Fig. 5.6). The differences in the particle size distribution for the two routes are due to the difference in precipitate behaviour of the powder. In the NP route while the reagents are in bulk volume the precipitant (NH_4OH) is available in localized area and in lesser volume. However, in RS route the precipitant is in large volume but the precursors is added in small drops. Thus the precursors are completely hydrolyzed and produce small particles which are highly agglomerated as revealed by the higher average agglomerate size of RS powder.

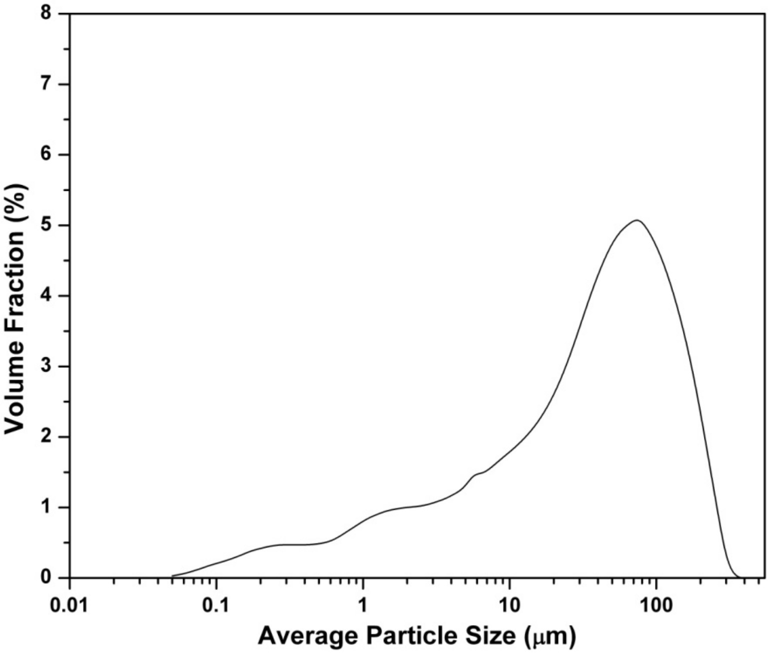

Fig.5.6. Particle size distribution of calcined HA (850°C/2hours) synthesized by RS route

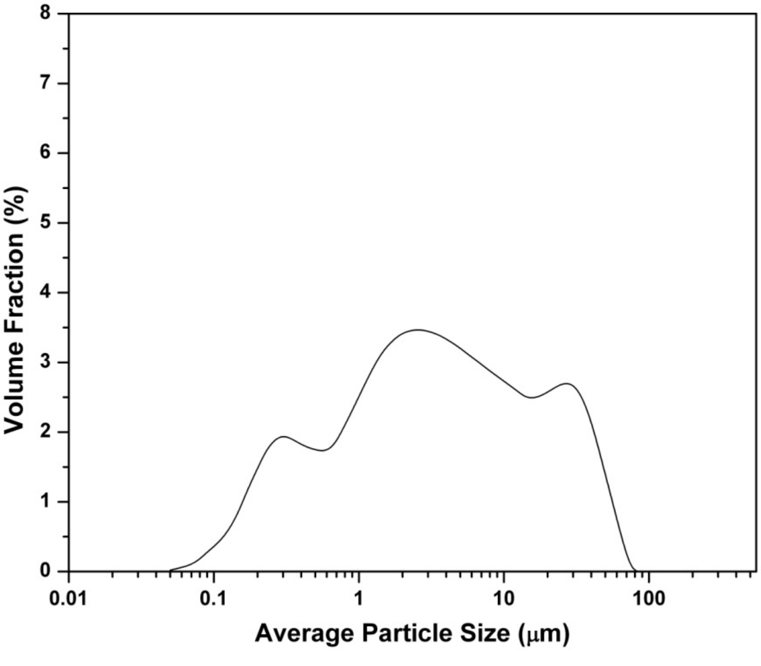

Fig.5.7. Particle size distribution of calcined HA (850°C/2hours) synthesized by NP route

Figure 5.8 and 5.9 shows the TEM micrograph of calcined (850^{O}C) HA powder prepared by RS and NP route respectively. Figure 5.8 shows that the as prepared particles have mixed morphology (i.e., both spherical and elongated morphology) and the powder appears to be less agglomerated. On the other hand, powder prepared by NP route (Fig. 5.9) shows agglomerated clusters with particle mostly in elongated shape.

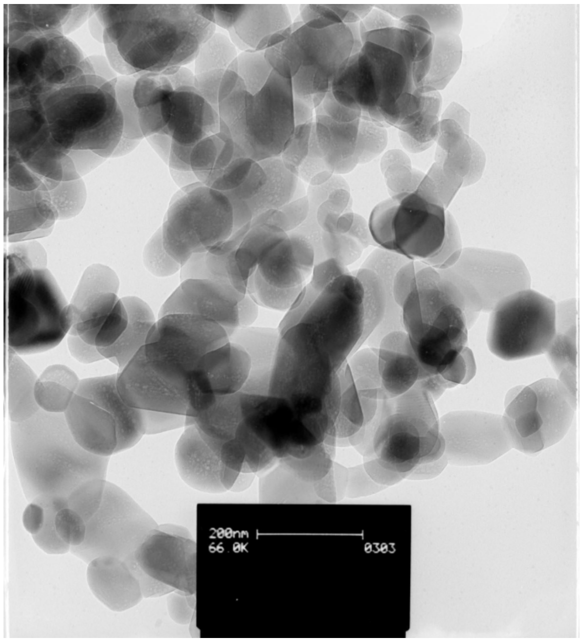

Fig.5.8. TEM micrograph of calcined (850^{O}C) HA Prepared by RS Route

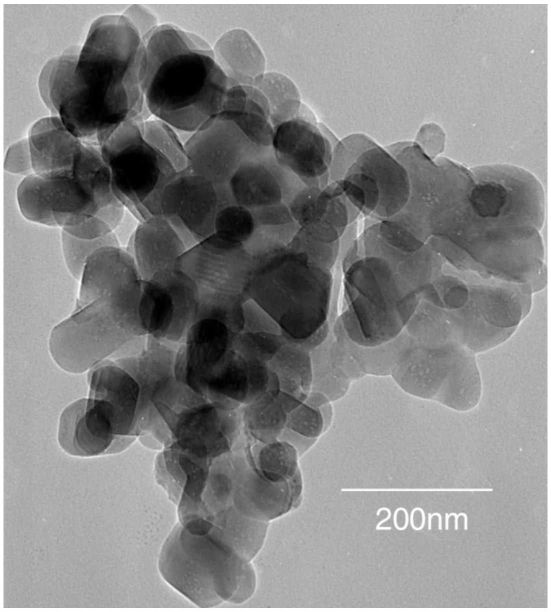

Fig.5.9. TEM micrograph of calcined (850^{O}C) HA prepared by NP Route

The higher surface area of HA produced by RS route compared to NP route could be attributed to the higher agglomeration of powder prepared by NP route as shown by the TEM images. Although Figure 5.8 and Figure 5.9 indicate little difference in particle size of the powder produced by RP and NP route the cause of the difference in sintered density in Figure 5.10 could be related to the difference in agglomeration behavior and particle size distribution of the powder produced by both the routes. While a uniform particle size distribution (mono modal type) was observed for powder produced by RS route (Figure 5.8), powder produced by NP route shows a non uniform (tri modal type) particle size distribution (Figure 5.9).

5.1.4 Relative Density of Sintered Compacts

The difference in the initial particle sizes between NP and RS route powders result in 7 % higher green density and 4 % higher sintered density of pellets prepared from RS powder in comparison to NP powder as shown in Fig. 5.10.

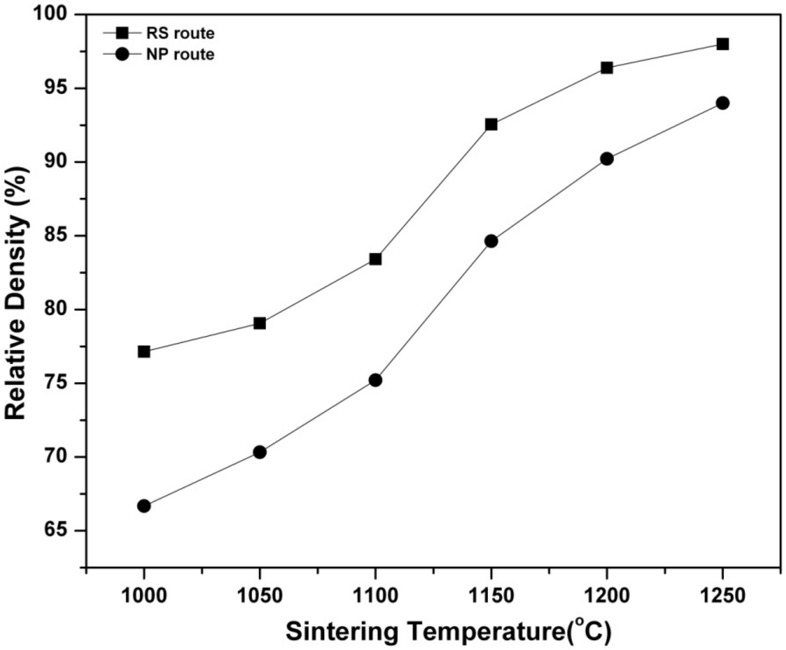

Fig.5.10. Relative sintered density of HA (synthesized by both RS route and NP route) pellets as a function of sintering temperature

5.1.5 XRD Analysis of Calcined Powder and Sintered Compacts

Figure 5.11 shows the XRD pattern of the powder prepared by RS route calcined between $650^{O}C$ – $950^{O}C$. The XRD pattern shows that RS powder has better crystallinity in comparison to NP powder. Considering the reflection from (002) plane of

HA, the crystallite size for this plane at temperature 650^{0}C, 750^{0}C, 850^{0}C and 950^{o}C are calculated as 23.49 nm, 24.52 nm, 26.07 nm, and 34.4 nm respectively.

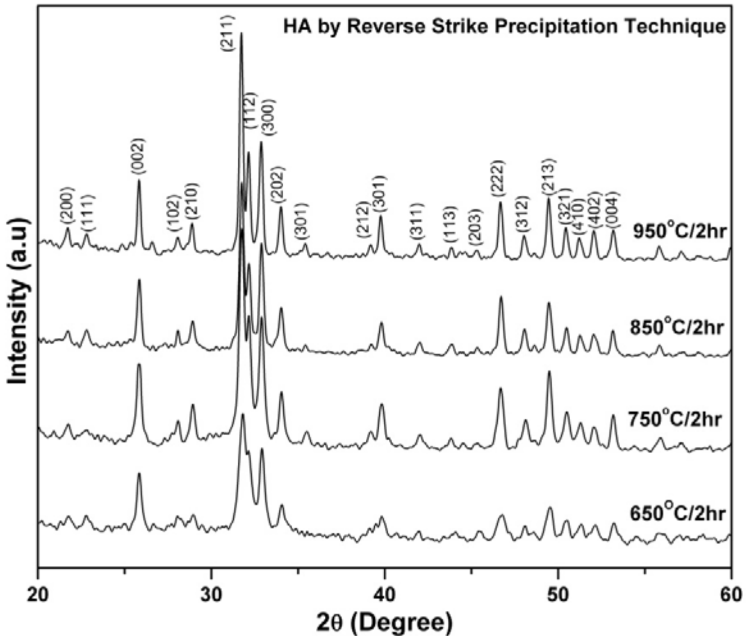

Fig.5.11. XRD pattern of HA powder (prepared by RS route) as a function of calcination temperature

A comparison of the XRD pattern of 850^{O}C calcined NP and RS route powder (Fig. 5.12) shows that a small amount of β-TCP is present in NP route powder. Therefore, NP route powder is less stable in comparison to RS route powder. Similarly at 1250^{O}C (Fig. 5.13), NP route powder show both β - TCP (d = 2.85 ^{o}A) and α - TCP (d = 2.9 ^{o}A) along with CaO (d =2.4 ^{o}A) while RS route powder show complete stability of HA phase. It has been reported that HA's decomposition to β and α - TCP and CaO is accelerated in non-stoichiometric HA. Thus NP HA powder is less stoichiometric in comparison to RS HA.

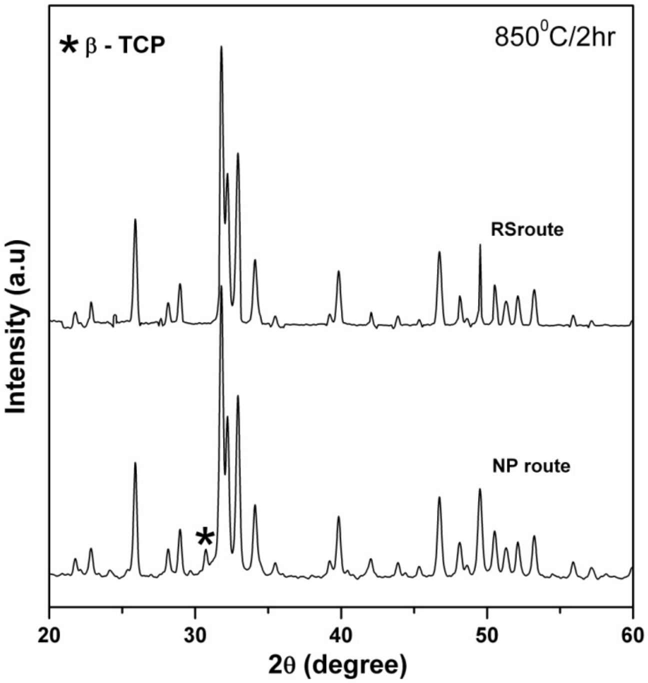

Fig.5.12. XRD pattern of HA powder (calcined at 850^0/2 hour) synthesized by both RS route and NP route

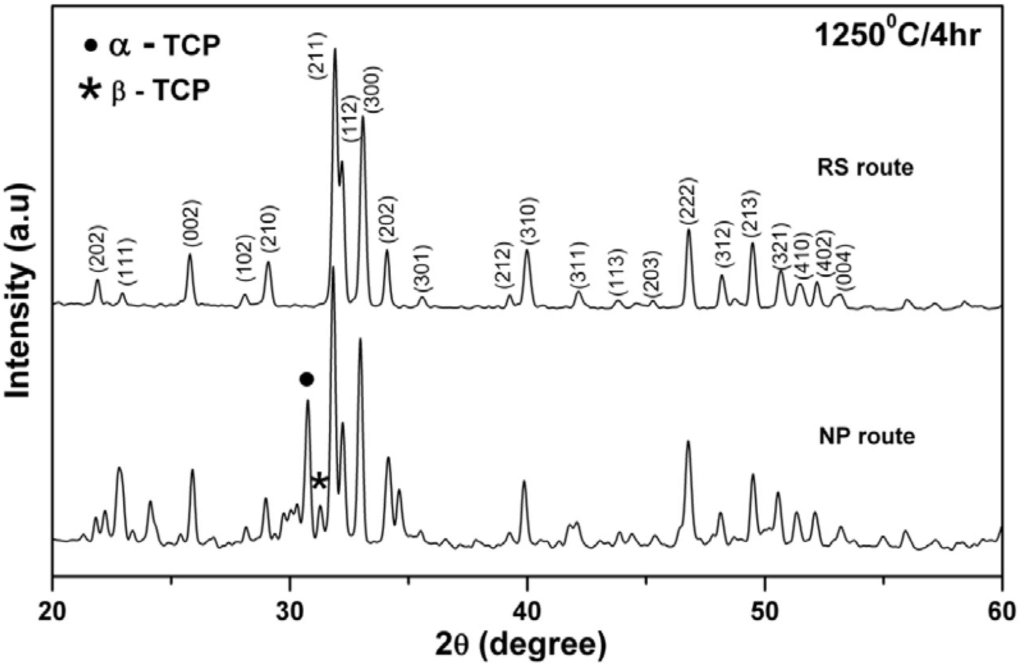

Fig.5.13. XRD pattern of sintered HA (1250^{0}C/4 hour) for both NP and RS route

5.1.6 Densification Behaviour of HA Prepared by RS and NP route

Figure 5.14 shows the linear shrinkage of HA pellets prepared by both the route. Though the sintering begins at almost same temperature (850°C) for both the samples but the final stage of sintering was achieved earlier for RS route samples owing to its faster shrinkage rate. However, in NP route samples, about 6 % porosity remains in the sintered sample. Thus NP route pellets require higher sintering temperature, thereby affecting the thermal stability of HA phase. On the other hand, pellets prepared from RS powder attain maximum relative density of 98 % at 1250°C/ 4 hours with no decomposition of HA phase.

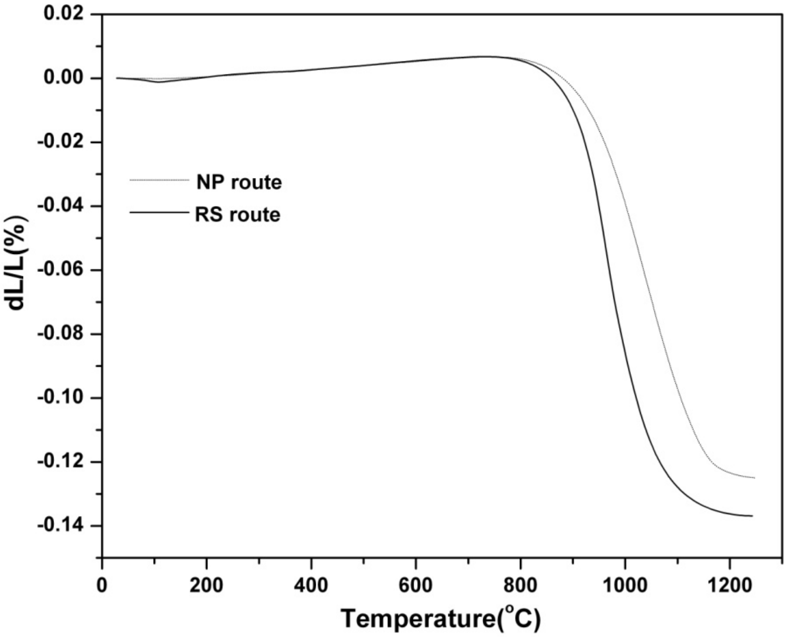

Fig.5.14. Non Isothermal densification curve of HA prepared by both RS route and NP route

5.2 Conclusions

The present section dealt with the properties of HA powder and sintered pellets prepared by both NP and RS precipitation route using $Ca(NO_3)_2.4H_2O$ and $(NH_4)_2HPO_4$ as the precursor. The section also emphasized the importance of powder processing in deciding the final phase, particle morphology, particle size and its distribution in the as prepared powder, calcined powder as well as sintered pellets. The FTIR spectra of the calcined RS powder showed all peaks corresponding to that of stoichiometric HA. XRD of calcined and sintered pellets showed that the RS-HA is more stoichiometric and phase stable. The RS-HA showed all peaks corresponding to that of HA but the NP- HA had partially decomposed to TCP. The particle size distribution of calcined powder was multimodal for NP and monomodal for RS route. The sintered density of RS - HA was higher than that of NP route at all the sintering temperatures.

On the basis of the above results and observations it was concluded that RS route is better suited for processing of stoichiometric and phase stable HA. Therefore, further processing of HA-TZP composite powder will be done by RS route only.

Section B

Processing and Characterization of HA-YTZP Composites

5.3 Preparation of HA-YTZP Composite by Reverse Strike (RS) PrecipitationRoute

The HA-YTZP composite powder containing various weight % of TZP 2, 5, 7.5 and 10 (henceforth referred to as HZ2, HZ5, HZ7 and HZ10 respectively) calcined at 850^{O}C (HZ8 composites) and prepared by RS route have been discussed elaborately in Section 4.3. The following sections deal with characterization of powder and sintered composites prepared by RS route.

5.3.1 Thermal Analysis of Dried Powder

Figure 5.15 shows the DSC/TG curve of the precipitated HZ2 powder. The nature of the curve and the total weight loss (4.74 %) is comparable with that of pure HA (5.78 %). This curve also shows one broad endothermic peak in the temperature range 30-100^{o}C with peak at about 70^{o}C along with a weight loss of 3.21 % corresponding to the loss of adsorbed water. The weight loss is lower than pure HA as the amount of HA is less by 2 %. Similarly, the second phase weight loss from 100^{o}C to 400^{o}C is also lower in HZ2 in comparison to pure HA (Section 5.1.1, Fig. 5.2). However, the broad exothermic peak of HZ2 in the range of 650^{0}C–1050^{0}C is at a lower temperature (~ 25^{O}C lower than that of HA) and the three peaks at 800^{O}C (d = 2.82), 850^{O}C (d = 2.81) and 910^{O}C (d = 2.817) are clearly observed.

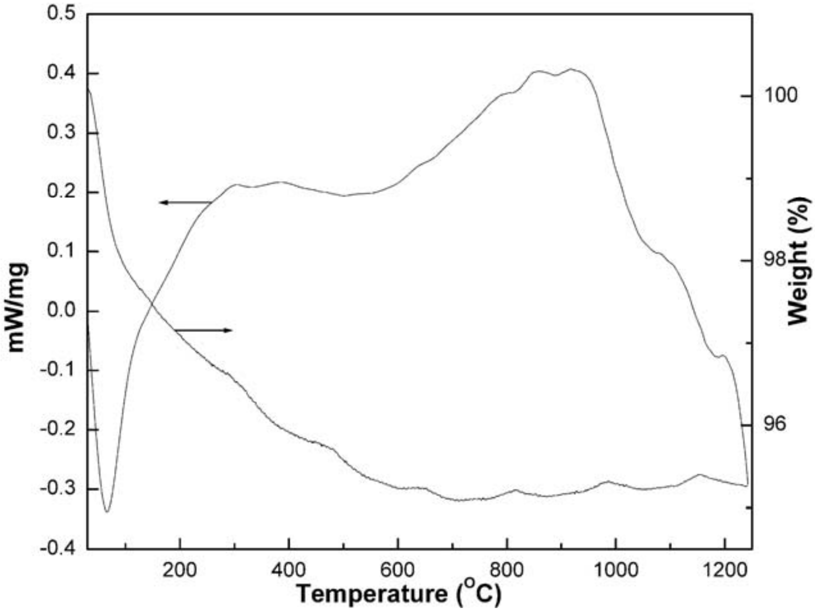

Fig.5.15. **DSC/TG pattern of HZ2 composite**

The percentage crystallinity of HA in HA and HA-TZP composites has been determined from the XRD pattern for the temperature range 650^0C-1050^0C [Table 5.2]. The Table shows that the addition of TZP reduces the crystallization temperature of HA in HZ2 and also improves the crystallization behaviour of HA. However, no significant change in either the crystallization behaviour or the crystallization temperature could be observed in HA with higher amount of TZP (viz.HZ5, HZ7 and HZ10) addition.

Table 5.2 Percentage crystallinity of HA

Temperature	**Crystalline HA Phase in (%)**				
	HA	**HZ2**	**HZ5**	**HZ7**	**HZ10**
650^0C	50.3	55.9	49.5	50.5	50
850^0C	71.8	78.1	70.85	71.8	71.73
1050^0C	94.8	98.2	90.83	92.3	92

Figure 5.16 shows the FTIR spectra of HZ2 powder calcined at 850^OC/2hour. Most of the peaks correspond to that of HA as described in Section 5.1.2, Fig. 5.4. Due to the weak nature of vibration and super imposition by PO_4^{3-} band and O-H bending, no peak for Zr-O (449 cm^{-1}) or Zr-OH (1643 cm^{-1}) could be observed.

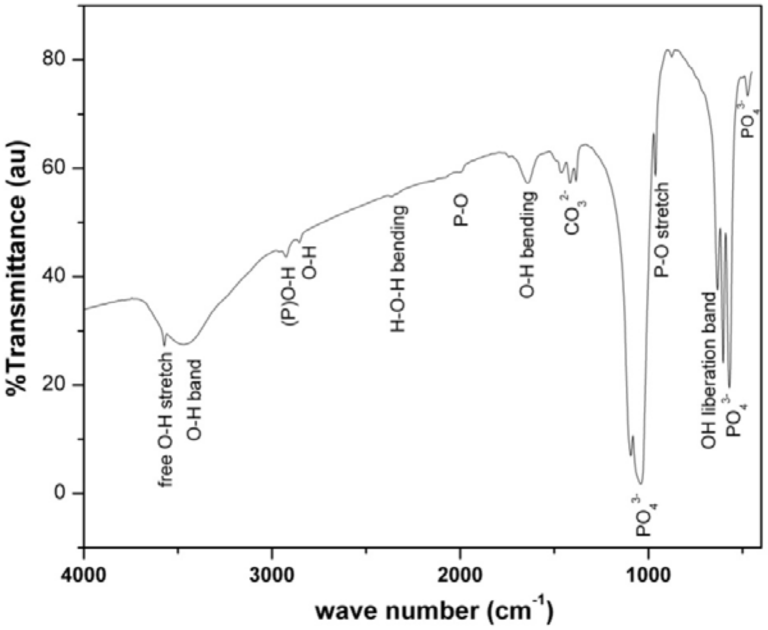

Fig.5.16. FTIR spectra of calcined HZ2 composite

5.3.2 Phase and Crystallite Size of Calcined HA and HA-TZP Powder

Figure 5.17 shows the XRD of calcined ($850^{O}C$) HA and HA-TZP composite powder (HZ2, HZ5, HZ7, HZ10). The XRD pattern of the calcined powder shows only HA and t-ZrO_2 peaks are present. No other phases like α-TCP, $CaZrO_3$ or m-ZrO_2 could be detected. The intensity of t-ZrO_2 (d = $2.95^{o}A$) increases with the increase in TZP content. Even at the highest TZP addition (HZ10), only HA and t- ZrO_2 could be detected. The intensity of HA and t-ZrO_2 peaks increase and the peaks also become sharper with the increase in calcination temperature indicating that crystallite size increases on calcination at higher temperature. With the increase in calcination temperature from $650^{o}C$ to $850^{o}C$, the crystallite size of HA (in the HA–TZP composite) increases from 24 nm to 34 nm and that of TZP from 12 nm to 26 nm

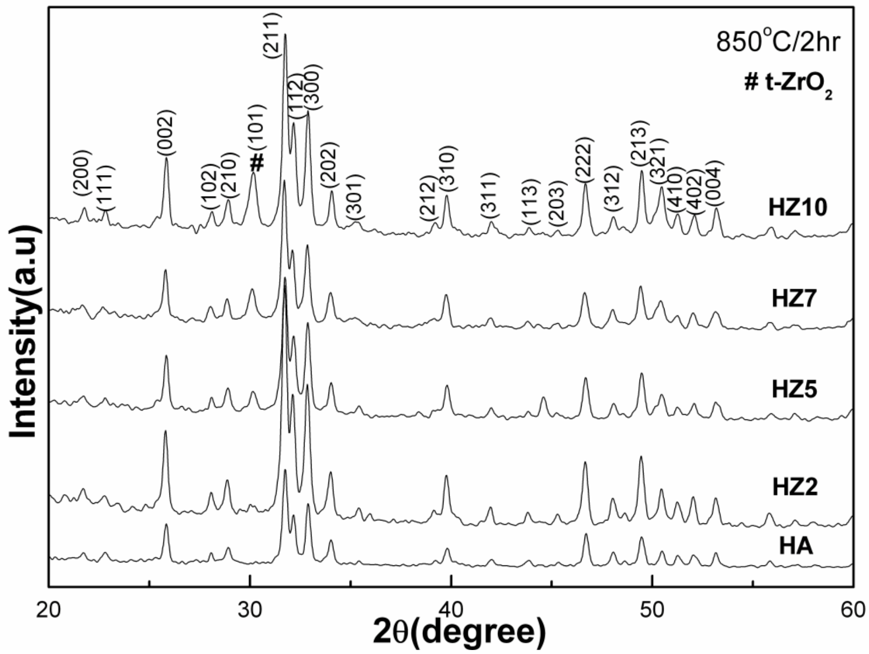

Fig.5.17. Phase evolution of calcined HA-TZP powder as a function of TZP content

5.3.3 Particle Size Distribution and TEM Study of Calcined Powder

Figure 5.18 shows the particle size distribution of calcined HZ2 composite. Similar to HA (Section 5.1.3), the distribution spans over a wider particle size range. The fine fraction (< 10μm) is 20 volume % and the coarse fraction (> 80μm) is 80%. The mean particle size (d_{50}) is 40.45 μm. In comparison to pure HA (Fig. 5.6), Fig 5.18 shows a small hump in the range of (0.1 μm -1μm). This could be attributed to the small amount of fine

TZP (2 wt%) powder present in the composite, which further improves the fineness of HA-TZP composite powder.

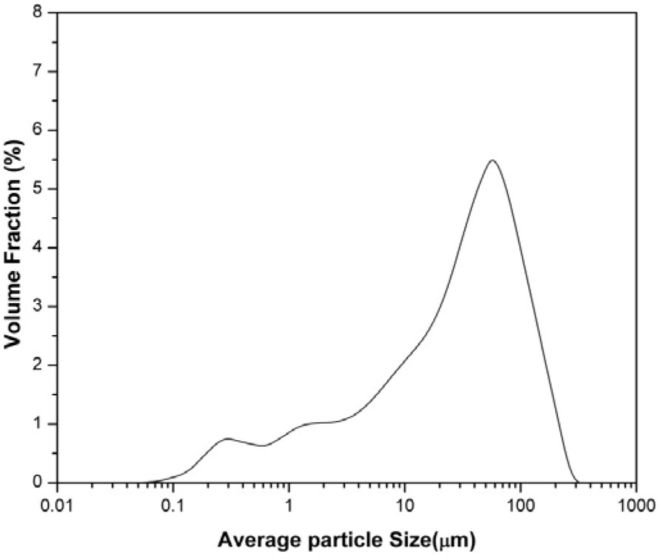

Fig.5.18. Particle size distribution of HZ2 powder calcined at 850°C/2hour

Figure 5.19 shows the dark field TEM photographs of calcined HZ2 (850^{o}C) powder. The TZP are dark colored spherical particles embedded in light colored HA matrix. The micrographs also reveal that nano TZP (<50nm) are uniformly distributed in the HA matrix. This uniform distribution of TZP in HA matrix result from the narrow particle size distribution of TZP particles.

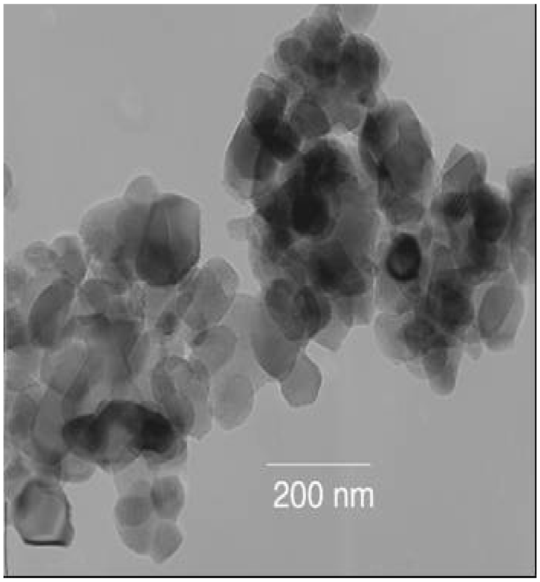

Fig.5.19. TEM photograph of calcined HZ2 powder (850°C/2hours)

5.3.4 Densification Behaviour of HA and HA-TZP Composites

Figure 5.20(a) shows the non isothermal densification behaviour of HA and HZ2, HZ5, HZ7 and HZ10 green compacts up to 1250^{o}C. Except for HZ10, the shrinkage of all other samples starts around 900^{o}C. In HZ10 samples, the shrinkage start around 1000^{o}C and it was not complete even till 1250^{O}C. Similarly in HZ5 and HZ7 sample also although the densification started at a lower temperature (~ 900^{o}C), it did not reach the final stage till 1250^{o}C. This implies that both HZ7 and HZ10 composite require higher sintering temperature for significant densification. However, both in HA and HZ2 samples, the densification reaches the final stage by 1250^{O}C and therefore, these two samples achieve high sintered density at 1250^{O}C. The densification behaviour of HZ5 samples lie in between these two extremes and the slope change in densification curve at around 1200^{o}C shows that in HZ5 the final stage densification has started but the process remained incomplete and sintering at higher temperature would be required for further densification of HZ5 composites. All these variations in densification behaviour could be attributed to TZP addition. With increasing TZP content, the densification shifts to a higher temperature. Further, a comparison of the densification curve of HA and HZ2 reveals that although the shrinkage in HZ2 starts at higher temperature (870^{O}C) than HA (840^{O}C), the shrinkage in HZ2 is higher than HA and the densification completes at a lower temperature than HA. Thus HZ2, have a higher rate of densification compared to HA and it is postulated that small addition of TZP acts to help in completing the densification at a lower temperature without affecting the phase composition.

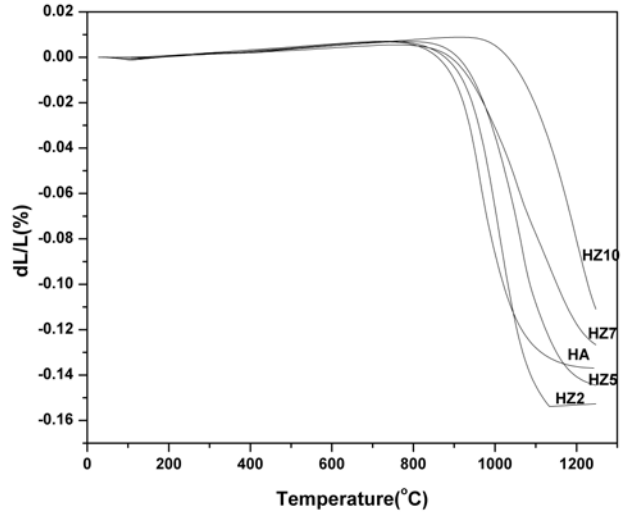

Fig.5.20(a). Nonisothermal densification curve of HA and HA–TZP composites

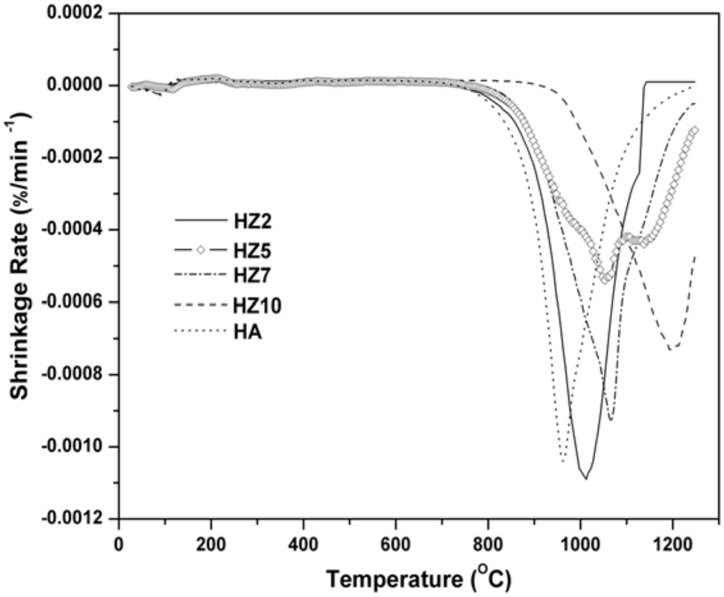

Fig.5.20(b). Shrinkage rate curve of HA and HA–TZP composites

The derivative plot of Fig 5.20(a) is shown in Fig 5.20(b). The plot shows that the densification rate for HZ2 is higher than that of HA, thereby confirming that at low TZP addition the densification of HA is enhanced. The interesting feature of the derivative densification plot (Fig 5.20(b)) is the densification behaviour of HZ5. The densification rate curve has three steps corresponding the densification –cum decomposition of HA to TCP and $CaZrO_3$. The number of steps decreases for HZ7 and is not distinct for HZ10. The plot implies that densification of HZ5 will be incomplete.

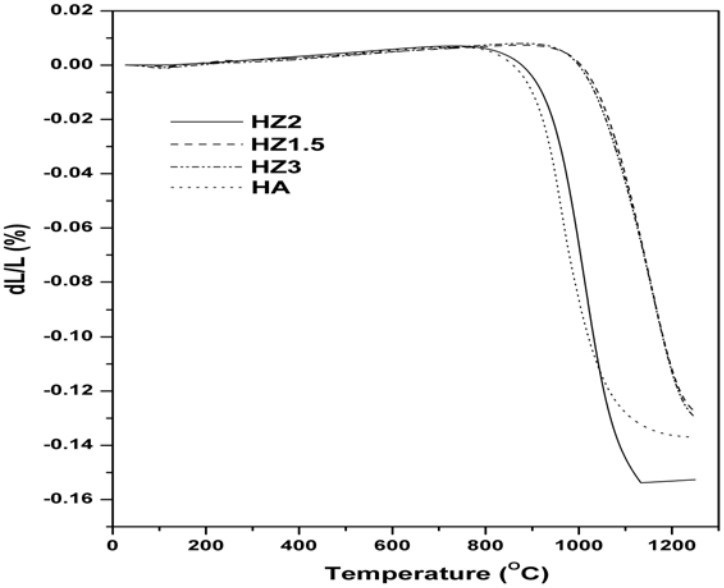

Fig.5.20(c). Nonisothermal densification curve of HA, HZ2, HZ1.5 and HZ3 composites

It need to be pointed out that Fig 5.20(c) shows that the dilatometric densification behaviour of HA -2 wt% TZP composite is even higher than HA. This is in contrast to other HA-TZP compositions, viz. HA- 5wt% TZP, HA-7.5 wt% TZP and HA- 10wt% TZP composites. In all these the densification is slower than HA and in some cases, the final stage of densification did not even start. Thus, TZP addition appears to restrict the densification behaviour of HA-TZP composites except for HA- 2 wt% TZP composition. In order to investigate this behaviour the densification behaviour of two other HA-TZP composites (viz. HA-1.5 wt% TZP and HA- 3wt% TZP) were studied. It was surprising that latter two composites show that the onset of densification shifts to higher temperature in comparison to HA. Thus both HA-1.5 wt% TZP (HZ1.5) and HA-3 wt% TZP (HZ3) composites had reduced densification in comparison to HA. This behaviour could not be explained properly in the present study due to the lack of detailed TEM study. It is proposed that this will form the future study.

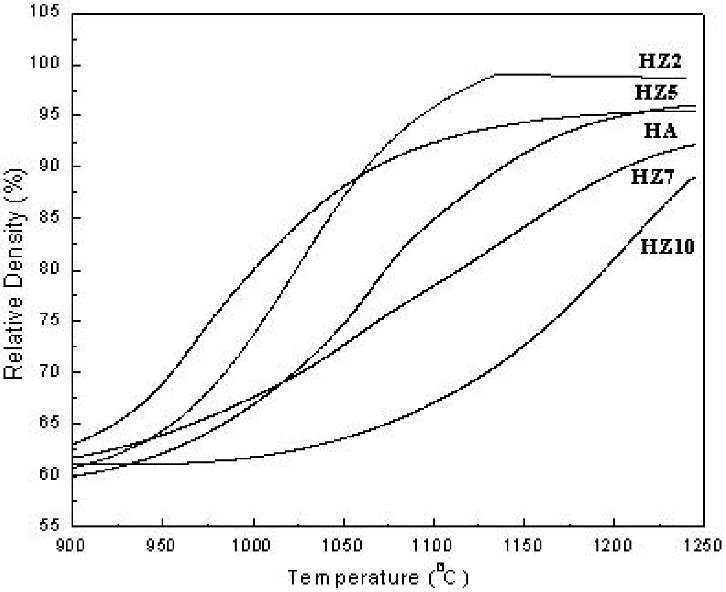

Fig.5.21. Relative Sintered Density of HA-TZP composite as function of sintering temperature

Figure 5.21 shows the plot of relative sintered density vs sintering temperature for HA as well as HA-TZP samples. The Figure shows that only for HA and HZ2 samples all the three stages of sintering (viz. initial, intermediate and final) could be clearly observed and in both of them the density has reached the plateau region. However, for

HZ5 and HZ7, although the final stage has started the final density has not been achieved at 1250°C and the final stage density still has the rising trend. However, in HZ10 samples, the density graph could show only the initial stage of densification and this composition would require further higher temperature to attain final density. This trend in densification is following the trend observed in other studied involving HA–TZP, where the retarded densification was observed with TZP addition [5.3, 5.4]

5.3.5 XRD and Phase Analysis of Sintered Composites

Figure 5.22 shows the XRD pattern of the sintered samples of HA and HZ2 to HZ10. It is observed that HA is stable till 1250°C and no other phases (e.g. β-TCP, $CaZrO_3$) could be detected. Similarly in HZ2 samples, only HA and t-ZrO_2 could be detected and identified. However, in HZ5 and HZ7 samples, beside HA and t-ZrO_2, small amount of $CaZrO_3$ ($d = 2.84$ A°) and β-TCP ($d = 2.90$ A°) could also be seen. $CaZrO_3$ and β-TCP forms according to the reactions given below [5.5]:

$$\text{t-ZrO}_2 + \text{CaO} \rightarrow \text{CaZrO}_3 \qquad (5.3)$$

However, this removal of CaO from HA takes place through a series of steps. Usually this decomposition reaction of HA initiates with the removal of structural water from it as per the reaction given below (Eqn. 5.4) [5.6, 5.7]. This reaction makes the HA nonstoichiometric, which triggers the decomposition to tricalcium phosphate and tetracalcium phosphate (TTCP) (Eqn. 5.5) [5.8].

$$\text{Ca}_{10}(\text{PO}_4)_6(\text{OH})_2 \rightarrow \text{Ca}_{10}(\text{PO}_4)_6(\text{OH})_{2-2x}\text{O}_x + x\text{H}_2\text{O} \qquad (5.4)$$

$$\text{Ca}_{10}(\text{PO}_4)_6(\text{OH})_{2-2x}\text{O}_x \rightarrow 2\text{Ca}_3(\text{PO}_4)_2 + \text{Ca}_4[\text{O}(\text{PO}_4)_2] + (1-x)\text{H}_2\text{O} \qquad (5.5)$$

The absence of TTCP phase in the XRD pattern of all the sintered HA-TZP composite suggests that TTCP formed reacts with TZP to form TCP and $CaZrO_3$, according to equation 5.6.

$$\text{Ca}_4[\text{O}(\text{PO}_4)_2] + \text{t-ZrO}_2 \rightarrow \text{Ca}_3(\text{PO}_4)_2 + \text{CaZrO}_3 \qquad (5.6)$$

or

$$\text{Ca}_{10}(\text{PO}_4)_6(\text{OH})_2 + \text{t-ZrO}_2 \rightarrow 3\text{Ca}_3(\text{PO}_4)_2 + \text{CaZrO}_3 + \text{H}_2\text{O} \qquad (5.7)$$

Hence, the addition of TZP not only hastens the decomposition of HA by transforming

HA to TTCP and/or TCP but also results in the formation of $CaZrO_3$. This process continues till an identical chemical potential is attained for Ca ion in both HA and TZP. However, HA can still maintain its apatite structure till a crucial amout of Ca is shifted to ZrO_2 particles The amount of TCP in HZ5 composition was much higher in comparison to TCP amount in HZ other compositions. Higher TCP fraction implies that HA decomposition is probably due to the Ca-deficient HA for this composition. A small peak of β-TCP was also identified in HZ10 samples, although no $CaZrO_3$ peak could be observed. Thus it is seen that progressive addition of TZP to HA, accelerates the partial decomposition of HA to TCP due to the consumption of CaO from HA along with the formation of $CaZrO_3$, which reduced retention of t-ZrO_2 and HA in HA-TZP composite.

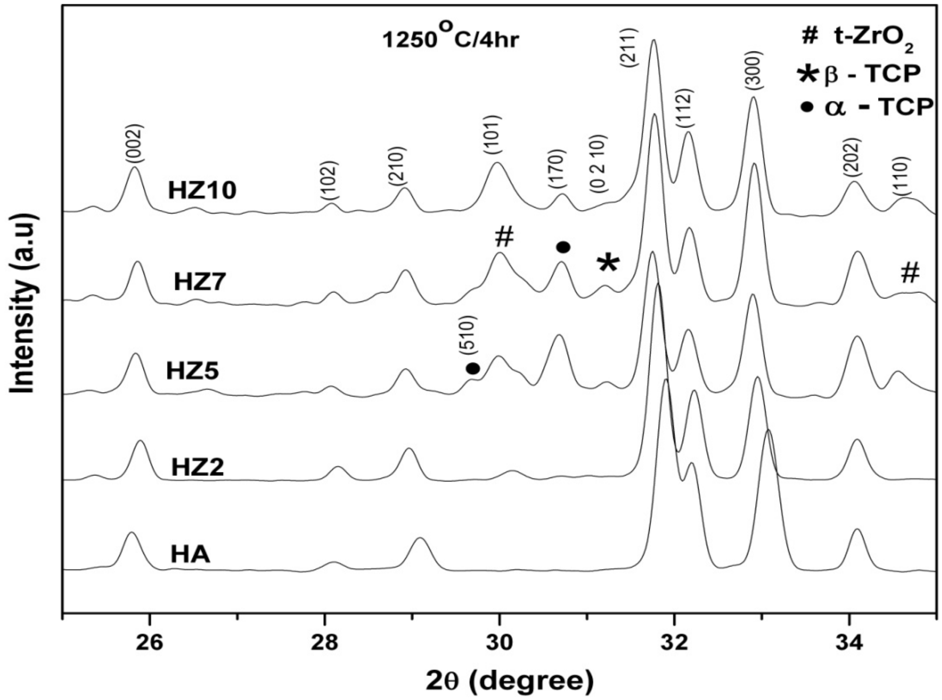

Fig.5.22. XRD pattern of HA, HA–TZP composites sintered at 1250^{0}C/4 hrs.

Table 5.3 shows the relative x-ray intensity of various phases present in sintered HA and HA-TZP composite [5.9]. This shows that the optimized phase composition (having both HA and TZP) was obtained only for HZ2 along with no decomposition of HA to TCP or formation of $CaZrO_3$ on TZP addition. However, with further addition of TZP (HZ5 and HZ7 composites), both β-TCP as well as α-TCP could also be seen, along with HA and t-ZrO_2. For HA-10 wt% TZP composition, the fraction of both β-TCP and α-TCP is relatively low. Lower amount of TCP formation at higher TZP addition viz. HZ10 could be attributed to the decreased contact between HA and TZP particulate, which might have resulted due to the decreased density of the composites [5.10 - 5.12].

Table 5.3 Relative X- ray intensity (%) of various phases in sintered HA, HA-TZP composites

	Phases in Sintered Pellets			
	HA	**TZP**	**β-TCP**	**α-TCP**
HA	**100**	**—**	**—**	**—**
HZ2	**96.50**	**3.50**	**—**	**—**
HZ5	**64.9**	**11.3**	**6.2**	**17.6**
HZ7	**71.2**	**12.7**	**5.1**	**11**
HZ10	**79**	**14.50**	**Tr.**	**6.5**

5.3.6 Relative Density of Sintered Compacts

Figure 5.23 Shows the relative sintered ($1250^{O}C$/4 hour) density of sintered HA-TZP composite as a function of TZP content. The figure shows that near theoretical density (> 99%) could be achieved in HZ2 composite and this density value are even higher than that of pure HA (98%). However, further addition of TZP i.e. HZ5 composite brings down the relative sintered density to around 96%. This decreasing trend in density further continued also at HZ7 and HZ10 composites with relative density coming down to 92% and 90% respectively. Ahn et.al reported that the bulk density of TZP may be playing a retarding role in bringing down the overall density of the composite [5.13]. Besides the different shrinkage behavior of HA and TZP grains may also lead to void formation at the interface of HA and TZP thereby reducing the density of the composite [5.14]. The various mechanisms which may define the enhanced densification at 2 wt% TZP addition are:

(i) Dissolution of ZrO_2 in HA matrix, leading to the formation of a glassy phase. [5.10].

(ii)TZP acting as phase impurity in HA matrix thereby inhibiting the grain boundary mobility and increasing the pore mobility [5.15].

Out of these two, the first mechanism may involve liquid phase sintering but since we did not observe any liquid phase sintering behaviour hence the second mechanism may be applicable for this system.

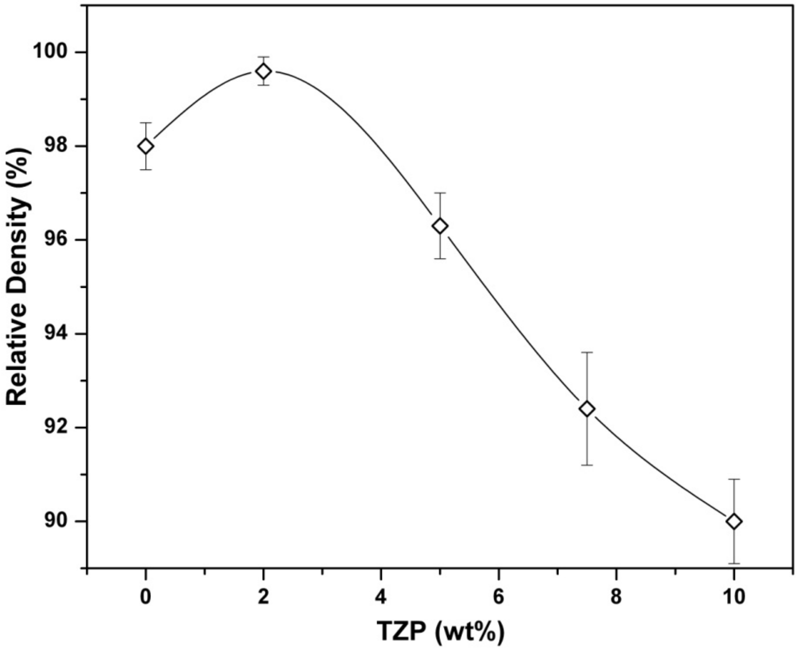

Fig.5.23. Relative sintered density of HA, HA–TZP composites sintered at 1250^{0}C/4 hours.

5.3.7 Flexural Strength, Biaxial Fexural Strength, Fracture Toughness and Hardness of Sintered HA and HA-TZP Composite

Figure.5.24 shows three point bending strength of sintered HA and HA-TZP (HZ2, HZ5, HZ7 and HZ10) composites as a function of TZP content. The curve shows that HA has a bending strength of about 35 MPa which increases sharply to 72 MPa for HZ2 composition. This sharp rise in strength for HZ2 composites is due to some phenomenon beyond the normal densification effect and can be related to the extremely fine grain size of HA observed in this sample. This type of sharp increase in strength has also been observed by Ahn. et. al while working in similar systems [5.13]. From the literature it is found that for a comparable grain size (0.84 μm), the observed strength was 90 MPa [5.16]. Using that correlation the predicted strength for HZ2 should be 82 MPa, the difference between the predicted and observed strength may be due to the presence of a few extremely large HA grains in this sample. At higher TZP addition, the bending strength drops to about 30 MPa for HZ5 and to 40 MPa for HZ7. Thereafter, the drop in strength is very less for HZ10 (37 MPa). Although, this drop in strength for HZ5 to HZ10 samples could be attributed to the residual porosity present due to incomplete sintering, the strength and density variation does not follow the well known relation $\sigma = \sigma_0 \exp(-bp)$.

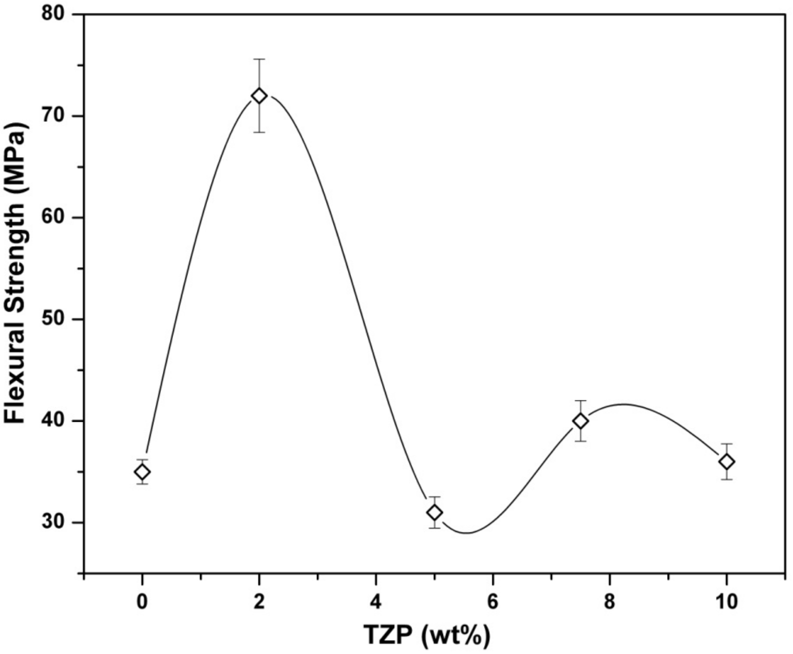

Fig.5.24. Flexural strength of HA-TZP composite as a function of TZP content

A similar trend in biaxial flexural strength (Fig. 5.25) was also observed with a sharp increase in strength from 13 MPa for pure HA to 34 MPa for HZ2 composite. Further addition of TZP (HZ5, HZ7, HZ10) shows a sharp fall in strength value. In HZ5, the strength value drops down to around 11 MPa, a value very close to that of HA strength. Thus, beyond 2 wt % TZP, further addition of TZP does not contribute to any significant improvement in strength value. This could be attributed to the increase in residual porosity with an increase in TZP content, resulting from incomplete densification of the composite. The incomplete densification arises from a higher sintering temperature (1400^0C) required for complete densification of TZP as compared to that of sintering temperature (1250^0C) of HA-TZP composite. The low fracture strength can also be correlated to the grain size. The grain size of HA in all the cases are more than 2 μm.

This large grain size of non cubic HA creates large thermal expansion anisotropy stress in the material [5.14] and makes the matrix susceptible to microcracking, because non cubic ceramics are thermally anisotropic with different thermal expansion along different crysatallographic directions. Particularly in case of polycrystalline ceramics such as TZP, a sufficiently large local internal stress are generated around grains with anisotropic α (coeffficient of thermal expansion) value to cause grain boundary fracture on cooling or leads to even grain microcracking [5.17]. The resultant microcracks reduce the fracture strength of the composites. The strength has also grain size dependence in accordance with Hall- Petch relation. The theoretical fracture strength of HA was calculated following the data of Yasuda et.al [5.16]. The calculated fracture strength is 48 MPa while the observed fracture strength is 35 MPa. The difference in the calculated and observed strength is probably due to the microcracks present in the composite (as discussed above). The microcracks act as strength controlling flaws and limit the strength increase. However, the same microcracks offer resistance to crack propagation and increase toughness. However, in such case the peak in strength and toughness occur at different compositions. These kind of strengthening and toughening behaviors have been observed for other zirconia containing systems [5.18]. Another interesting aspect of microstructural feature of HA-3Y-TZP system needs to be mentioned. In all the compositions of HA -3Y-TZP, most of the bright TZP grains appear to be distributed on the surface of HA grains and it is difficult to find the TZP at the grain boundaries. This apparent anamoly in the microstructure can be understood on careful observation of the microstructure itself. Many TZP grains have been pulled out during the cutting and polishing of the samples. It can be noticed that these pullout voids have been located at the grain boundaries. In some cases the pulled out TZP grains have also formed agglomerates with other TZP grains. This type of grain pullout have also been observed in other composite systems involving one soft and the other hard grain [5.19].

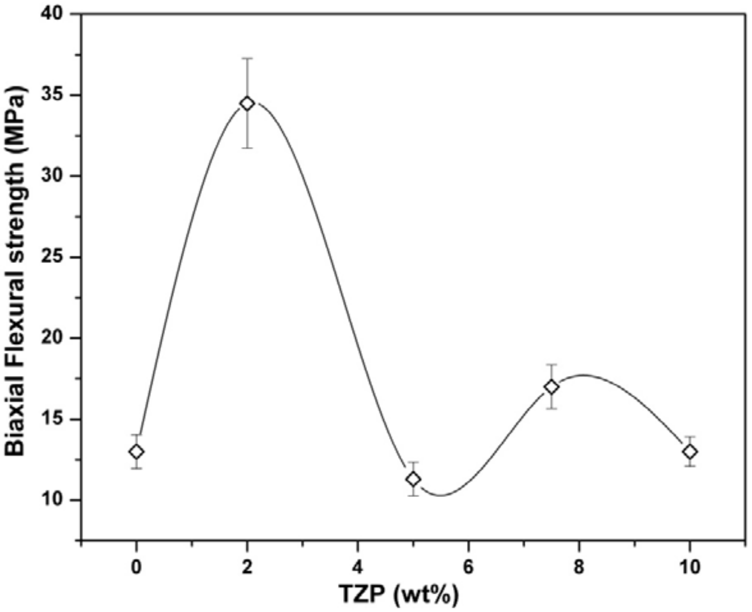

Fig.5.25. Bi axial flexural strength of HA-TZP composite as a function of TZP content

Table 5.4 Nominal flaw size as a function of TZP content in HA-TZP composites

	Y^2C (μm)
HZ2	120
HZ5	970
HZ7	500
HZ10	530

The nominal flaw size was calculated using the equation $K_{IC} = Y\sigma_f(c^{1/2})$. Table 5.4 shows that in case of HZ8 (TZP calcined at 850^{O}C) composites, the estimated flaw size is minimum for HZ2 and maximum for HZ5. If the strength is controlled by size of the largest flaw, then highest strength will be for HZ2 composite and lowest for HZ5. The measured strength is highest for HZ2 (72 MPa) and lowest for HZ5 (30 MPa) composites. Thus in HZ8 series composite, strength appear to be controlled by the size of processing flaw. Since HZ7 and HZ10 have same flaw size (500 μm and 530 μm respectively) and their strength values are also comparable (σ_f = 40 MPA and 37 MPa). It may also be mentioned that the calculated flaw size for HA is 344 μm which is lower than HZ5 composites. Therefore, the strength of HZ5 is even lower than HA. XRD pattern has revealed that α-TCP is highest for HZ5 composition which forms from β-TCP during the sintering process. The volume change associated with β-α TCP probably has generated large flaws. Thus the large flaw size causes lower strength of HZ5 composition. However, it is observed that these flaws did not affect the toughness. Figure.5.26 shows the fracture toughness (K_{IC}) of HA-TZP composites as a function of TZP content. The Figure show that the K_{IC} increases from the base value of 0.65 MPam^{½} for HA to 0.80 MPam^{½} for HZ2 and further increases to 0.97 MPam^{½} for HZ5. With further addition of TZP (HZ7 and HZ10) the toughness increases and particularly at HZ10, the toughness is significantly higher (30%) than that of HA. Thus with the addition of TZP to HA, there is a considerable improvement in K_{IC} of HA-TZP composite. The K_{IC} variation trend suggest that microcrack toughening can be dominant toughening mechanism (as no evidence of stress induced t-m TZP transformation could be observed on the fractured surface) in these composites. The large difference in CTE value of HA, TZP and TCP phases (along with the associated β - α TCP transformations) generates residual stresses at HA-TZP interface and produce microcrack/micro size flaws which help to increase toughness. It is also possible that incomplete densification at higher TZP addition (HZ5, HZ7 and HZ10) restrict the extent of K_{IC} increment. It is expected that complete pore removal as well as prevention of phase decomposition and TCP phase formation can help to further increase K_{IC}.

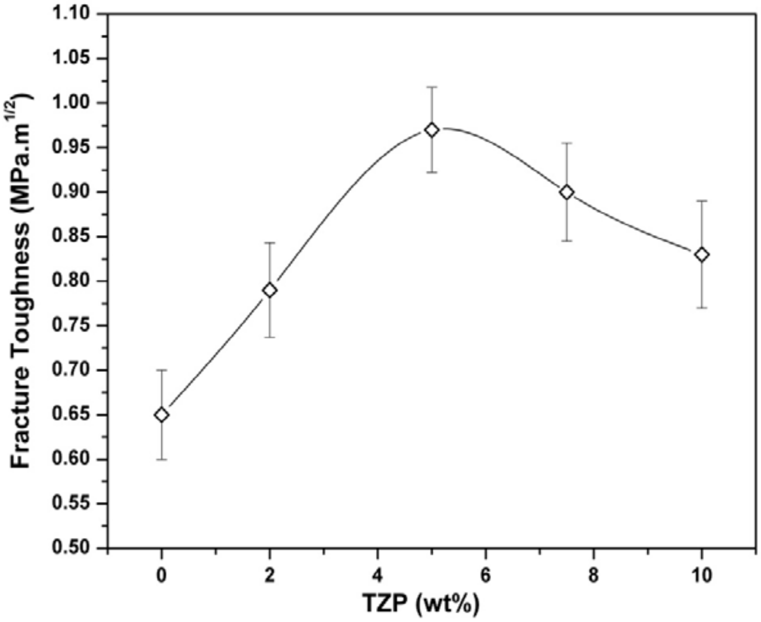

Fig.5.26. Fracture Toughness of HA-TZP composite as a function of TZP content

Figure.5.27 shows the variation of Vickers hardness for the composites as a function of TZP content. The curve shows a decrease in hardness with TZP addition. A maximum hardness of 3.83 GPa was found for HZ2 and a lowest of 2.43 GPa for HZ10 composites. The results are correlated with the increase in residual porosity at higher TZP content.

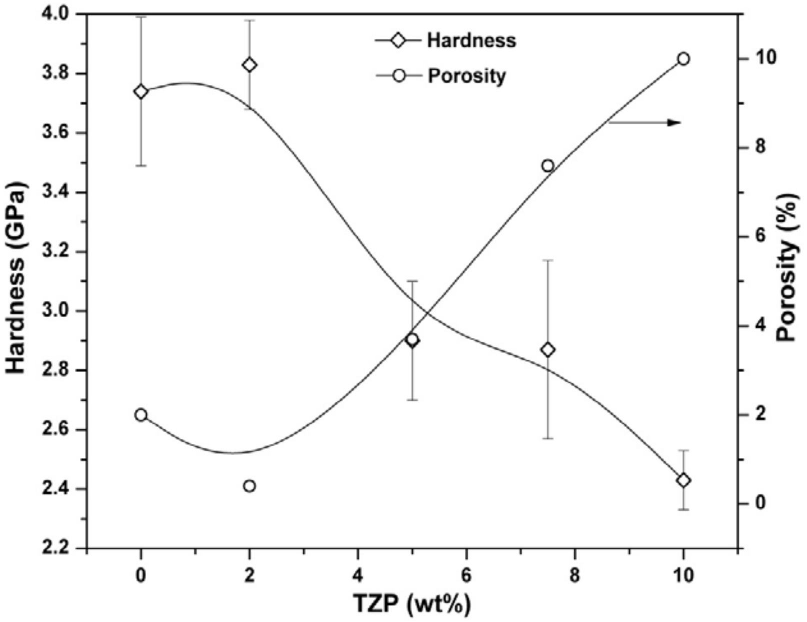

Fig.5.27. Vickers Hardness of HA-TZP composite as a function of TZP content

5.3.8 Microstructure and Grain Size of Sintered HA, HA-TZP Composites

Figure 5.28(a) to 5.28(e) shows the microstructure (SE Mode) of sintered HA [Fig. 5.28(a)] and HA-TZP composite [Fig. 5.28(b - e)]. HA microstructure shows presence of small pores at the grain boundary. In HZ2, (Fig 5.28(b)) due to very small amount of TZP, the TZP distribution could not be properly observed. In the remaining composites, the bright spots are TZP grain clusters, while the HA grains are darker. The TZP cluster size increases at higher TZP fraction. The grain size of HA changes on increasing TZP content as shown in Table 5.5. This is in agreement with the reported literature comment that TZP addition affects grain growth of HA [5.11, 5.20]. Some of HA grains are very large while other HA grains are smaller. This is particularly true for HZ2 composite where the average grain size is 1μm and a few very large grains (~ 5μm) are seen near lower right corner of the image. It is further observed that in HZ2, all the three type of grain sizes (finer, coarser and average) are smaller than HA as well as other HZ compositions. This shows that at 2 wt% TZP addition, some additional grain pinning mechanism is operative. With increase in TZP content, the grain size becomes increasingly uniform and at the highest wt % of TZP addition, i.e. HZ10, the difference in grain size is very less and the TZP dispersion is nearly uniform in HA matrix. However, it should also be mentioned that although a good dispersion of TZP could be achieved in HA -TZP composite, compositions containing higher TZP amount could not be sintered to near theoretical density. This causes a reduction in strength at higher TZP addition.

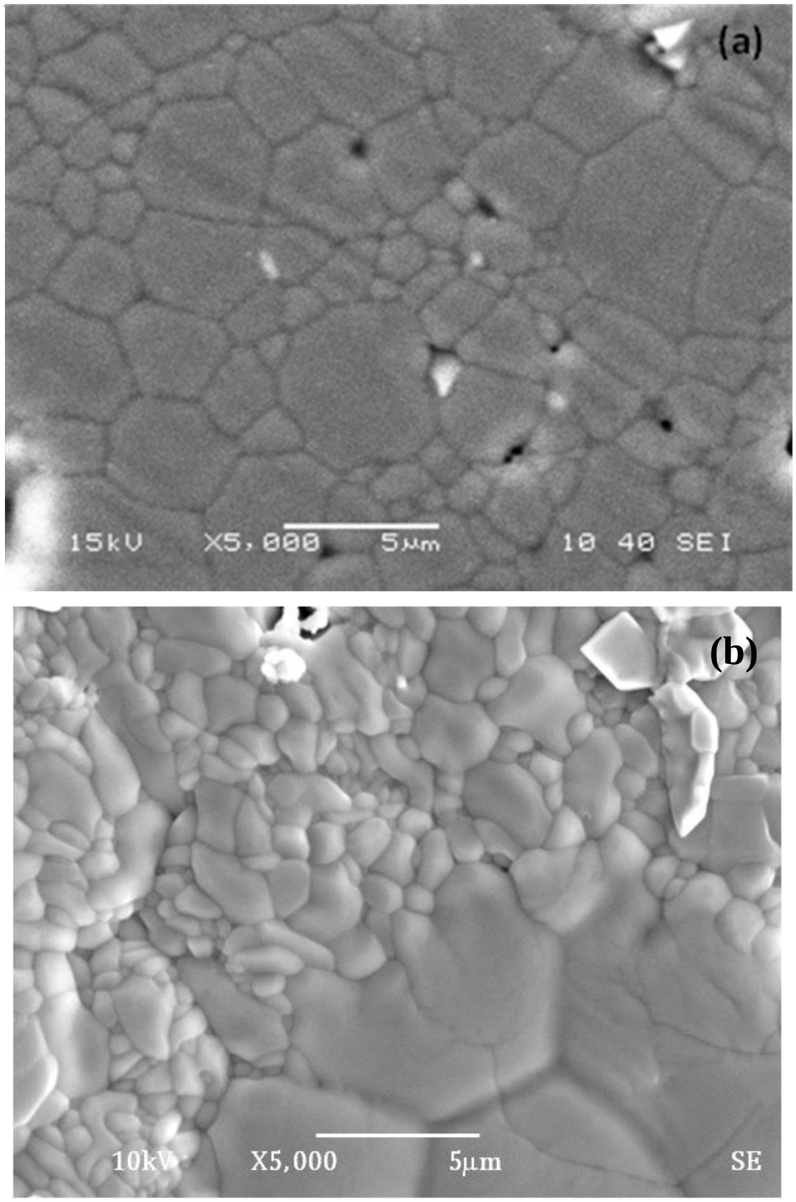

Fig.5.28. SEM image of HA, HA-TZP composites sintered at 1250^{O}C/4 hours (a) HA, (b) HZ2

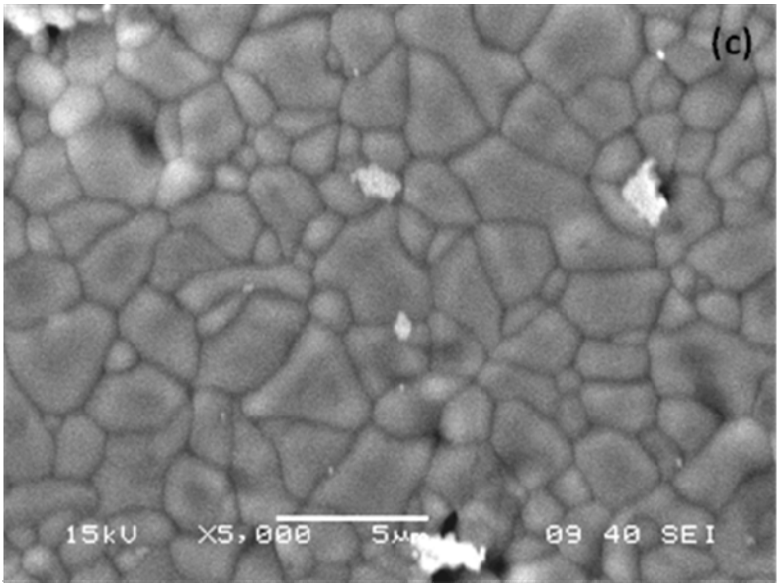
(c)
15kV X5,000 5μm 09 40 SEI

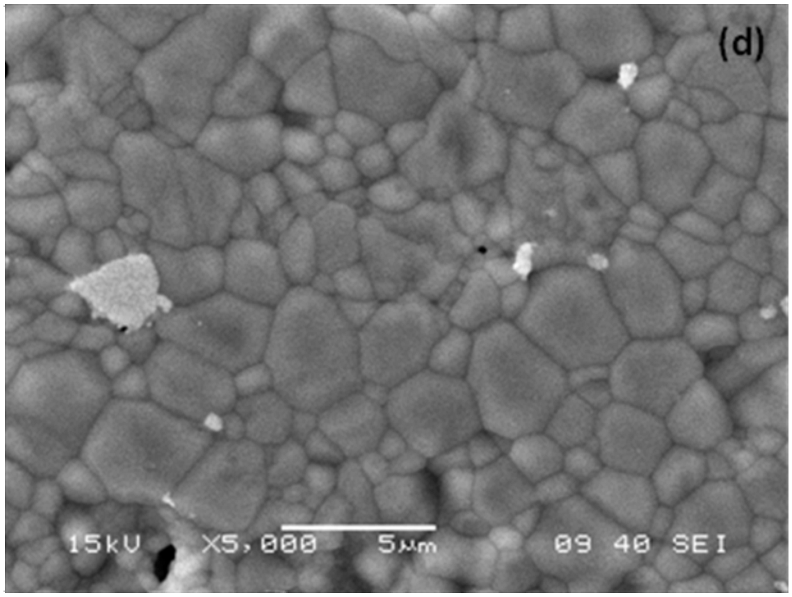
(d)
15kV X5,000 5μm 09 40 SEI

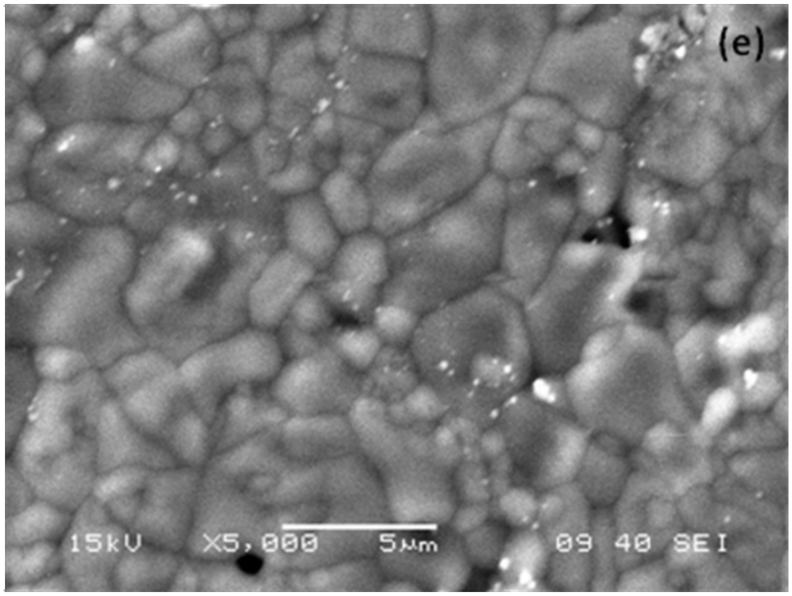

Fig.5.28. SEM image of HA, HA-TZP composites sintered at 1250^{O}C/4 hours (c)HZ5, (d) HZ7 and (e) HZ10

Table 5.5 shows the grain size distribution of HA, HZ2, HZ5, HZ7 and HZ10 composites. The microstructure of pure HA (Fig. 5.28 (a)) has a mixed grain size. The larger grains of HA are in 3-4 µm range, while the smaller grains are in the range 0.5 – 1.5 µm. Fig. 5.28 (b) shows that although the microstructure of HZ2 composite has a dense microstructure, the grain size distribution is peculiar with very fine HA grains in the range of 0-1µm and coarse grains in the range 6 - 7 µm. However, the number density of coarse grains in this case is comparatively less. The microstructure of HZ5 (Fig. 5.28(c)) and HZ7 (Fig. 5.28(d)) shows the effect of TZP addition, with the average grain size of HA shifting towards lower grain size value. In these samples, although a few large grains (~ 4 µm) are present, many small grains (0.5-1 µm) could also be seen. The microstructure is further refined in HZ10 composite (Fig. 5.28(e)) which shows a bimodal type distribution with a mixture of coarse grains (~ 3 µm) and fine grains (0.5 - 1 µm).

Table 5.5 Grain size distribution of HA, HA-TZP composite sintered at 1250^{O}C/4 hours

Grain Size (μm)	HA		HZ2		HZ5		HZ7		HZ10	
	Coarse	Fine	Coarse	Fine	Coarse	Fine	Coarse	Fine	Coarse	Fine
Average	3.63 ± 1.15	1.13 ± 0.3	2.12 ± 0.75	0.49 ± 0.18	2.90 ± 1.05	0.8 ± 0.41	2.70 ± 1.09	0.79 ± 0.39	1.97 ± 0.45	0.62 ± 0.24
Mean	2.48 ± 1.49		1 ± 0.88		1.70 ± 1.12		1.50 ± 1.17		0.99 ± 0.57	

5.4 Conclusions

HA –TZP composites (HZ2, HZ5, HZ7 and HZ10) were prepared by RS route. DSC/TG study revealed that addition of TZP to HA lower the decomposition weight loss and promotes low temperature crystallization of HA. TEM micrographs of calcined powders show spherical particles of TZP dispersed in cuboidal/ spherical HA grains. The sintered density of HA increases for HZ2 composite and attains almost theoretical density but it reduces with further addition of TZP. XRD revealed that in the sintered HZ2 composite, only HA and t-ZrO_2 is present. At higher TZP content (HZ5, HZ7 and HZ10), both β-TCP as well as α-TCP could also be seen along with HA and t-ZrO_2. The bending strength of HA (35 MPa) increases to 70 MPa for HZ2 followed by a decrease at higher TZP content. SEM microstructures show that the HA grain size distribution is multimodal, however, the average grain size of HA decreases with TZP addition. The decrease in strength at higher TZP addition could be due to a number of factors like poor densification of the composite at higher TZP loading, generation of microcracks due to TEA stresses at the HA-TZP interface as well due to the β – α TCP phase transformation. Based on the above observations, it is anticipated that an improvement in density of HA-TZP composite (by varying the processing parameters) particularly at higher weight % of TZP (HZ5, HZ7 and HZ10) is expected to improve the final mechanical properties of the composite.

Section C

Effect of TZP Calcination Temperature

5.5 Effect of TZP Calcination Temperature on the Density, Phase and Mechanical Properties of HA-TZP Composite

The previous section discussed the processing and characterization of HA-TZP composite prepared by RS route. It was observed that beyond 5 weight % TZP addition, the relative sintered density was low (typically around 90%). The reduction of relative sintered density with TZP addition could be related with the TZP calcination temperature. It has been reported by Wu et al [5.11] that TZP calcination temperature has a far reaching effect not only on the densification behavior but also on the mechanical properties of HA-TZP composite. This section, therefore, discusses the effect of TZP calcination temperature on the densification behavior, strength, toughness, hardness, phase composition and microstructure of HA-TZP composite prepared by RS route. The composite prepared with 850^{O}C/2hours calcined TZP (HZ8) are termed as H2Z8, H5Z8, H7Z8 and H10Z8 for 2, 5, 7.5 and 10 weight % TZP additions to HA respectively. In all the above four compositions the composite powder (i.e. precipitated amorphous HA- calcined TZP composites powder) has been recalcined at 850^{O}C/2 hours for crystallization of HA. Similarly for the HA-TZP composites prepared with 1200^{O}C calcined TZP (HZ12), the nomenclature are H2Z12, H5Z12, H7Z12 and H10Z12 for 2, 5, 7.5 and 10 weight % TZP addition to HA, the other processing conditions remaining same as before.

5.5.1 TEM Image of Calcined Powder

Figure 5.29 shows the dark field TEM photograph of H10Z12 powder. The HA particles are brighter and TZP particles are dark. It is observed that most of the HA particles are elongated bright particles, while TZP (5-10 nm) are very small spherical particles. The dark spherical spots are found to be uniformly distributed on the surface of HA particles.

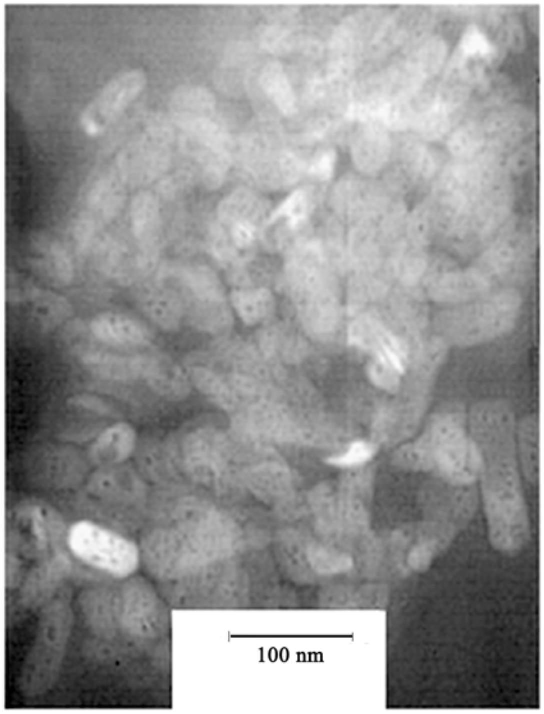

Fig.5.29. TEM image of H10Z12 powder calcined at 850^{O}C/2hour

5.5.2 Phase Analysis of Calcined HA-TZP Powder

Figure 5.30(a) shows the XRD pattern of calcined (850^{0}C) HZ12 series of composite powder. The XRD pattern shows that HA and TZP are the only phases present at the calcination temperature. A comparison of this XRD pattern with that of 850^{O}C calcined TZP powder (Fig. 5.30(b)) reveals that a higher TZP calcination temperature results in a larger TZP crystallite size 43.5 nm at 1200^{0}C as against 22.5 nm at 850^{0}C. However, the larger crystallite of TZP did not initiate any unwanted reaction between HA and TZP at least during the calcination stage.

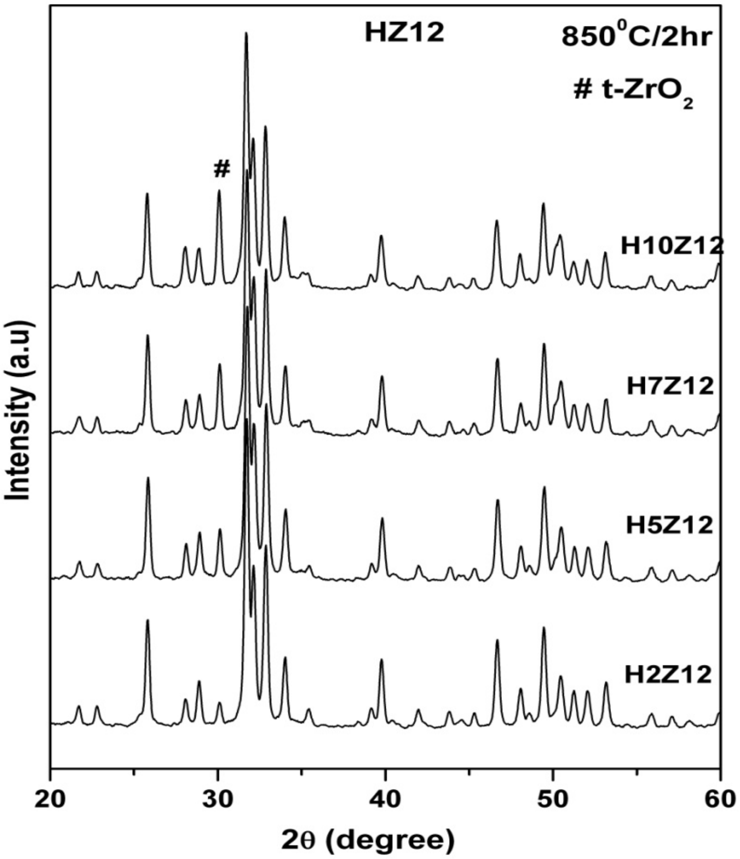

Fig. 5.30 (a). Phase evolution of calcined HZ12 powder as a function of TZP content

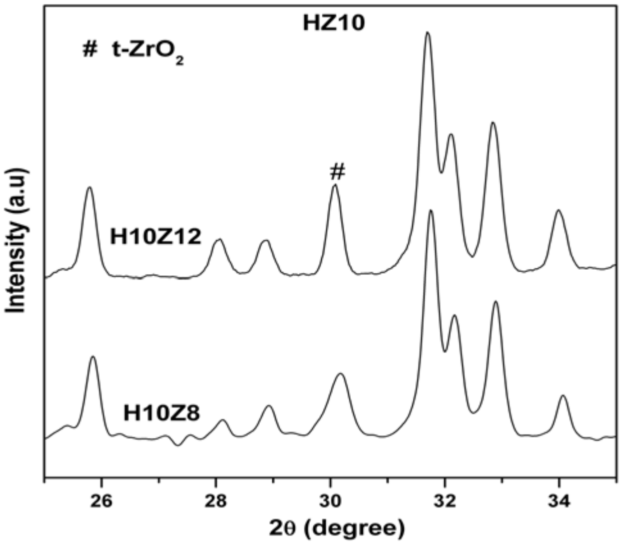

Fig. 5.30 (b). XRD pattern of H10Z8 and H10Z12 powder calcined at 850^{O}C

5.5.3 Relative Density of Sintered Compacts

Figure 5.31 shows the variation of relative sintered density of HA-TZP composites with TZP content. High sintered density (>99%) was obtained for HZ2 composite irrespective of TZP calcination temperature (i.e. 850^{O}C or 1200^{O}C). The sintered density reduces to lower value for HZ5 composition. The drop in density is higher and steeper for H5Z8 batch (curve a) in comparison to H5Z12 batch (curve b) [5.21]. In the 850^{O}C calcined TZP, the fine crystallites (12.5 nm) are agglomerated (agglomerate strength = 34.8 MPa) due to the high surface energy of fine crystallites. The presence of fine TZP agglomerates in the green compacts causes faster and localized sintering of TZP agglomerates. The sintered TZP grain cluster shrink away from HA matrix causing crack like residual voids [5.22]. The presence of voids retards the overall composite densification and poor sintered density results due to incomplete densification. However, increasing the TZP calcination temperature to 1200^{O}C, raises the TZP crystallite size leading to larger TZP particle size. The large TZP particles have lower agglomeration tendency (agglomerate strength = 29.3 MPa) and thus, effective particle packing is achieved. The differential shrinkage of the HA-TZP composites containing large TZP particles is minimized and both HA and TZP sinters nearly at the same rate. Thus in the HZ12 series, the reduction in the differential sintering of TZP grains results in a more homogeneous microstructure and higher sintered density for HA –TZP composites.

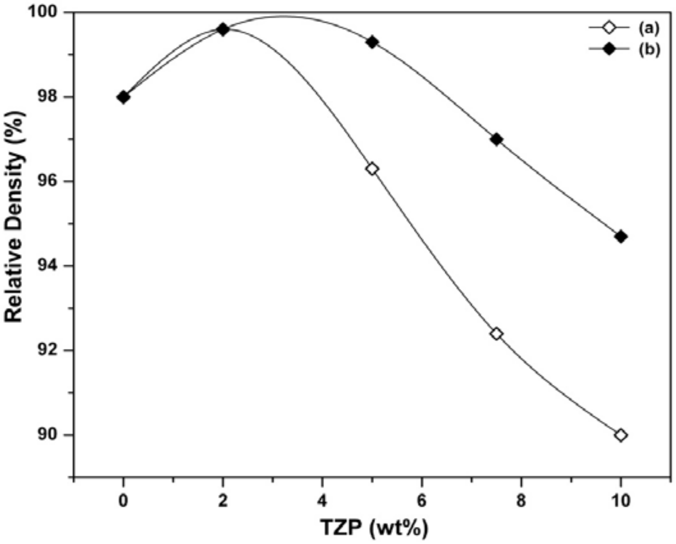

Fig.5.31. Relative sintered density of (a)HZ8 and (b)HZ12 composites as a function of TZP content

5.5.4 XRD and Phase Analysis of Sintered HZ8 and HZ12 Specimens

The X-ray diffraction pattern of H10Z12 sintered composites (1250^{O}C) is shown in Fig. 5.32 [5.21]. This figure shows that HA and t- ZrO_2 are the major phases present but it also contains substantial fraction of α-TCP as well as trace $CaZrO_3$. The above phase composition confirms that partial decomposition of HA–TZP composite takes place on sintering at 1250^{0}C. The decomposition effect was more pronounced for the H10Z12 batch. In this case, almost all the TZP has reacted with CaO (originating from decomposed HA) to produce $CaZrO_3$ (Fig. 5.32). A higher crystallinity of TZP in H10Z12 series although reduces the TZP agglomeration tendency and increases sintered density, but at the same time, larger crystallites and softer agglomerates cause more intimate contact between HA and TZP particles. Thus a higher TZP calcination temperature initiates an increased reaction between HA and TZP resulting in a higher degree of decomposition of TZP and results in lesser amount of HA and TZP retention in the sintered composite. Similar results were also observed for H7Z12 composite Fig. 5.33.

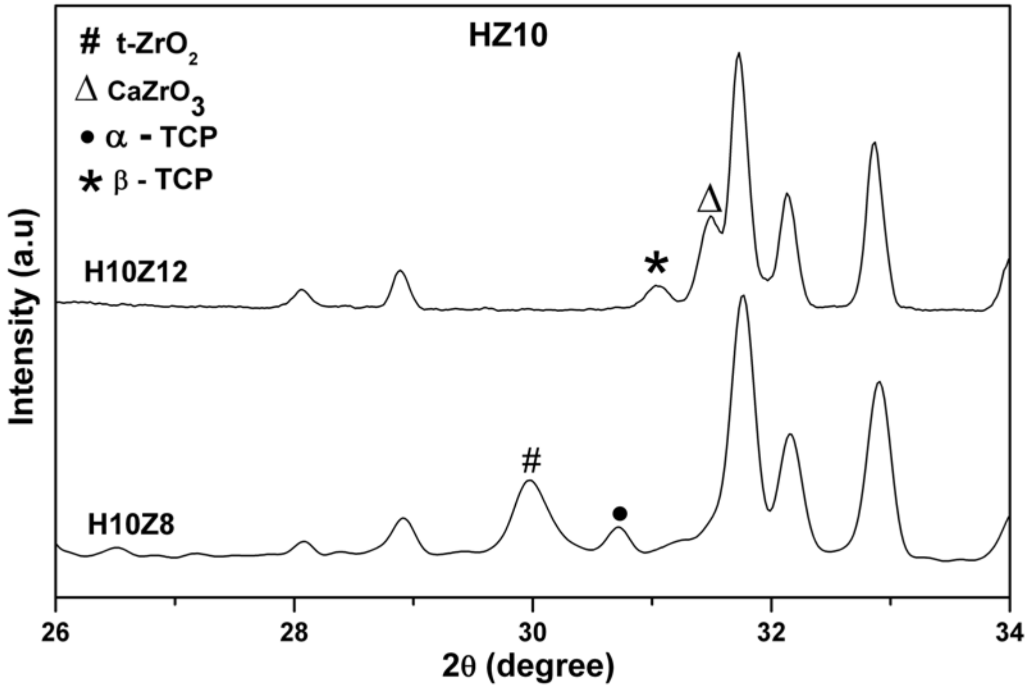

Fig.5.32. XRD pattern of HZ10 composites

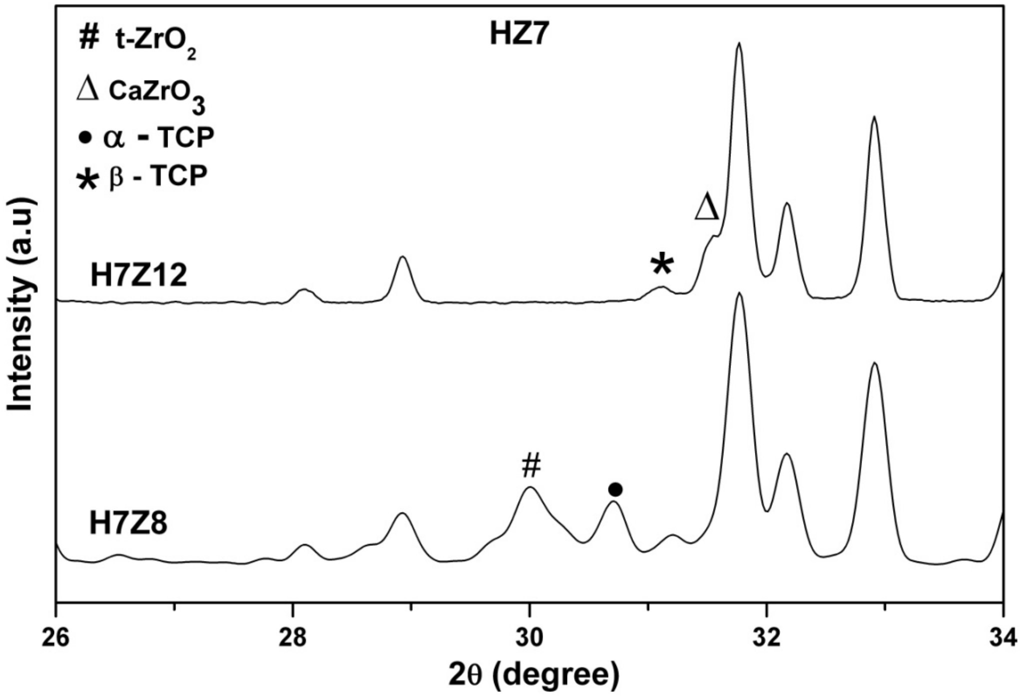

Fig.5.33. XRD pattern of HZ7 composites

5.5.5 Microstructure and Grain Size of Sintered HA, HA-TZP Composite

The effect of TZP calcination temperature on the microstructure of sintered HZ10 composite is shown in Fig. 5.34(a) and (b). The dark grains represent HA and the lighter ones are TZP. The microstructure shows that the HA grain size has increased sharply with the mean grain size being shifted from ~ 1 μm for H10Z8 composite (Fig. 5.34(a)) to ~ 6-7 μm for H10Z12 composites (Fig. 5.34(b)). Similarly, the microstructure of sintered H2Z12 (Fig. 5.34(c)), H5Z12 (Fig. 5.34(d)) and H7Z12 (Fig. 5.34(e)) specimens also show substantial increase in mean grain size (Table 5.6) with respect to their HZ8 counterparts (Table 5.5). Thus, the above observations suggest that an increase in TZP calcination temperature causes rapid grain growth of HA grain irrespective of TZP fraction in the composites. The standard deviation of grain size distribution indicate that the grain size distribution have become progressively more uniform, with less wider gap between the coarser and finer grain size (Table 5.6). It is found that unlike HZ8 composite, TZP is uniformly distributed on the HA matrix. The grain size of pure HA has a bimodal distribution with large grains ~ 3-4 μm and smaller grains ~ 1-1.5 μm (as discussed in section 5.3.8, Table 5.5). Similarly the microstructure of sintered H2Z8 composite (section 5.3.8), also shows a bimodal HA grain size distribution (Table 5.5). The larger HA grains are in the range of 6-7 μm, and the smaller grains are in the range of 0.5-1 μm, the few large bright regions correspond to distributed TZP clusters (grain size < 0.5μm) in the HA matrix. Figure 5.34 (b-e) reveals a dense microstructure for HZ12 composites showing very low residual porosity.

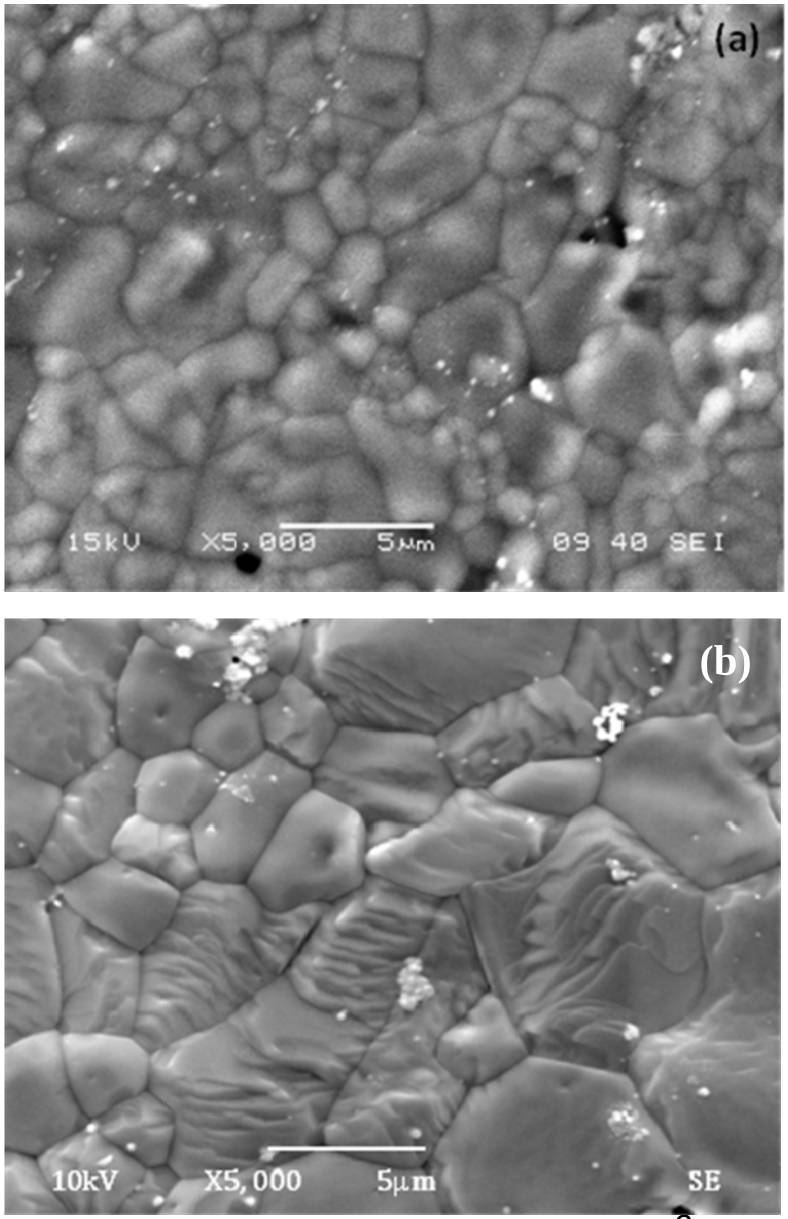

Fig.5.34. SEM image of HA-TZP composites sintered at 1250^{O}C/4 hours (a) H10Z8, (b) H10Z12

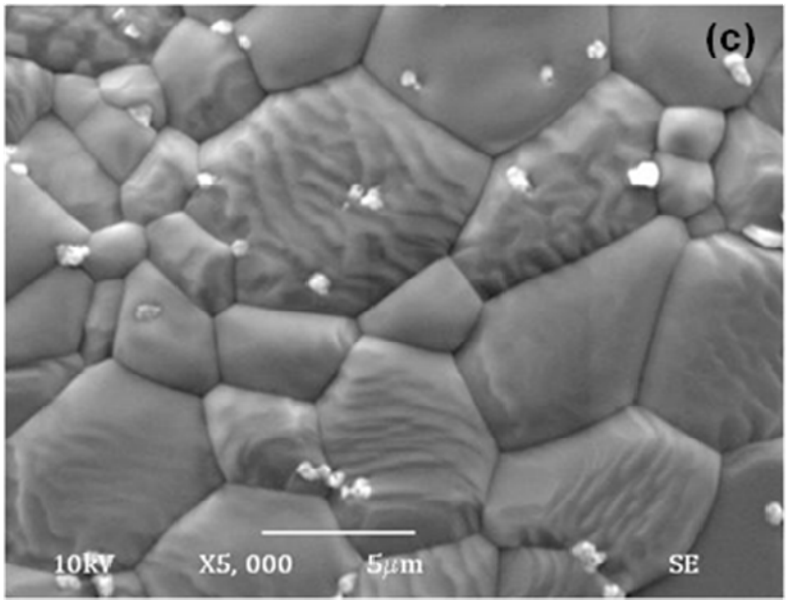
(c)
10KV
X5, 000
5μm
SE

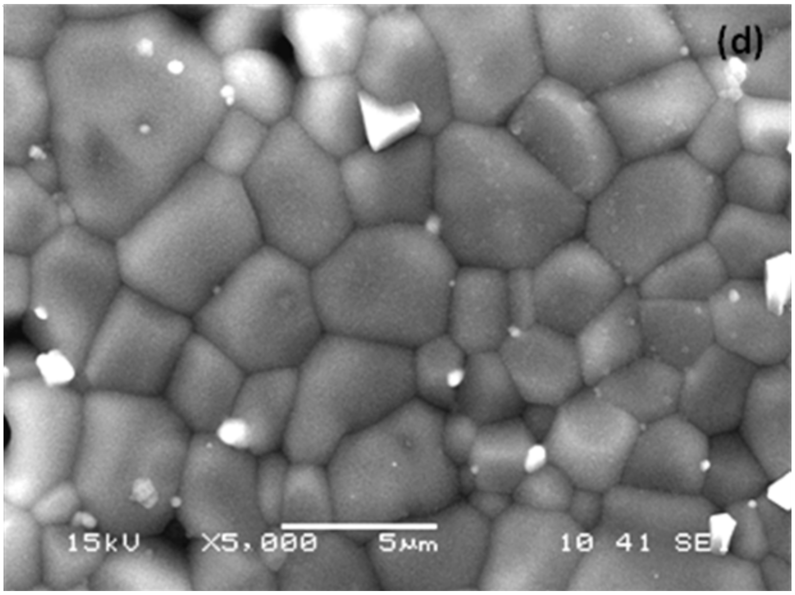
(d)
15kV
X5,000
5μm
10 41 SE

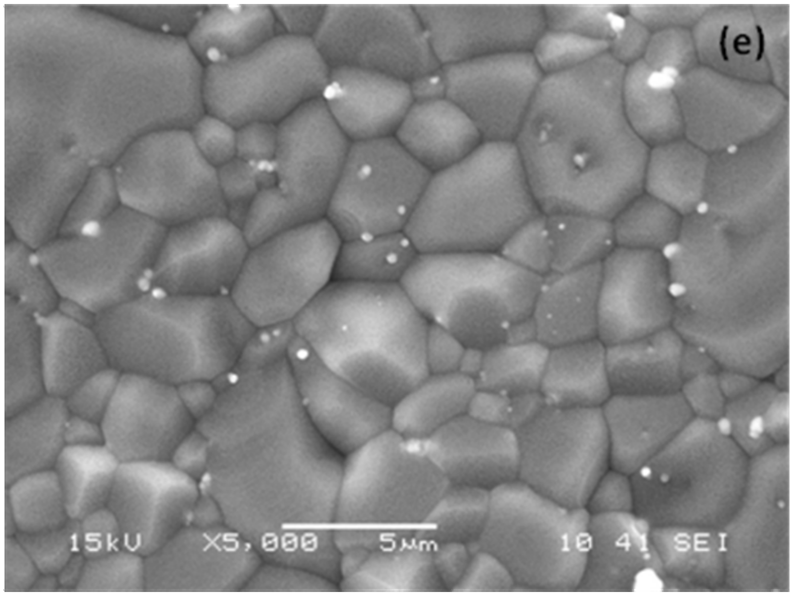

Fig.5.34. SEM image of HA-TZP composites sintered at 1250^{O}C/4 hours (c) H2Z12, (d) H5Z12, and (e) H7Z12

Table 5.6 Grain size of HA, HZ12 composite sintered at 1250^{O}C/4 hours

Composition	**Mean grain Size of HA (μm)**
HA	2.48 ± 1.49
H2Z12	5.03± 1.81
H5Z12	2.99 ± 0.93
H7Z12	3.52 ± 1.06
H10Z12	6.25 ± 2.02

5.5.6 Densification Behaviour and Phase Analysis of H10Z8, H10Z12 Composite

Figure 5.35(a) shows the dilatometric sintering behavior for H10Z8 (a) and H10Z12 (b) batch. While H10Z8 sample shows single stage shrinkage behaviour till 1250^{0}C, H10Z12 composite shows double stage shrinkage behavior with slope change at 850^{0}C and 1100^{0}C. The slope change corresponds to the change in the densification rate. It has already been stated that the XRD of H10Z12 shows that during sintering, HA and

TZP reacts to form TCP and $CaZrO_3$. The slope change corresponds to the onset temperature of above. Samples of H10Z12 composites were heated in a separate experiment to 850^{O}C, 900^{O}C and 950^{O}C respectively and phases were analyzed by XRD (insertion, Fig. 5.35(a)). The XRD corroborates the fact that the decomposition of HA to TCP and the subsequent conversion of TZP to $CaZrO_3$ on its interaction with TCP takes place simultaneously until an equilibrium of calcium ion is established (section 5.3.5). The XRD at 850^{O}C (Fig c) shows no peaks of TCP or $CaZrO_3$, whereas, the XRD at 900^{O}C (Fig d) shows only small amount of $CaZrO_3$ along with HA and TZP (without TCP), this could be due to the decomposition temperature of HA and formation of $CaZrO_3$. However, at 950^{O}C (Fig e), a small peak of β-TCP was also observed along with HA and $CaZrO_3$ (without TZP). Thus, at this temperature, the conversion of TZP to $CaZrO_3$ is almost complete with the presence of excess TCP.

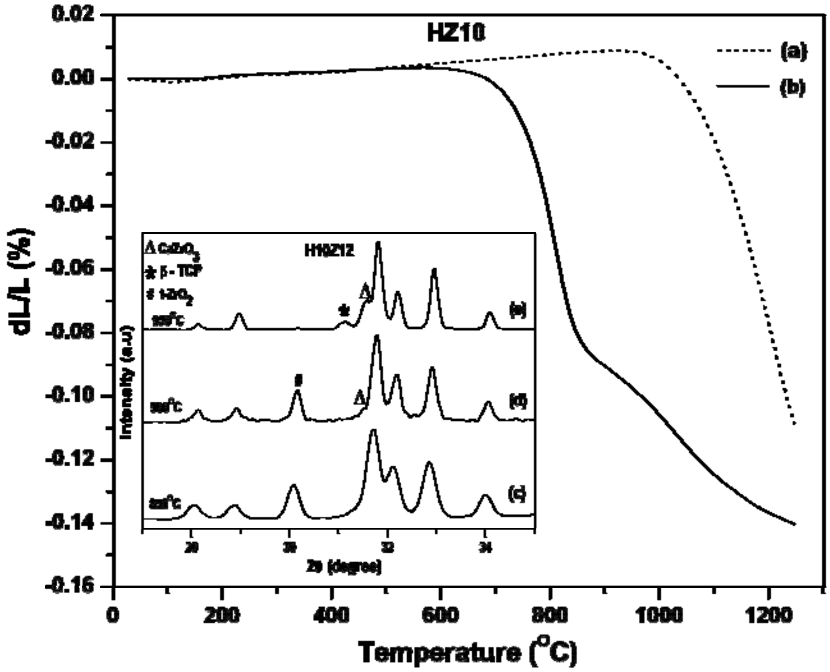

Fig.5.35(a). Non isothermal densification curve of HA-TZP composite (H10Z12)

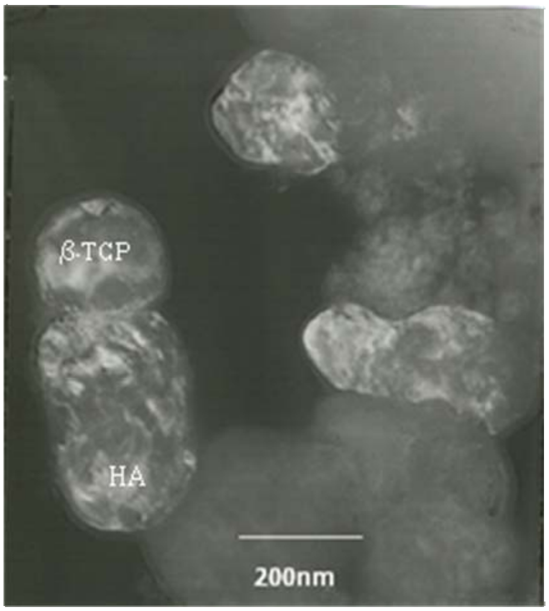

Fig.5.35(b). TEM image of H10Z12 composite calcined at $1000^{O}C$/2hours

TEM micrograph (Fig. 5.35(b)) of H10Z12 composite powder calcined at $1000^{O}C$, also show similar type of decomposition behaviour. The micrograph shows decomposition on the surface of HA particles. [5.23]

Detailed XRD analysis of pure HA and H10Z12 composite were carried out for visualizing the possible reaction product and reaction steps when HA reacts with TZP during sintering of HA-TZP composites. Figure 5.36 shows the consolidated XRD pattern of H10Z12 composite sintered at $1100^{O}C$ and $1250^{O}C$ respectively. For the sake of comparison phase analysis of pure HA was also considered (Fig. 5.36, bottom figure). It is seen that pure HA did not undergo any decomposition to either TCP or CaO till $1250^{O}C$. However, in HZ12, $CaZrO_3$ and β- TCP could be observed at $1100^{0}C$. The peaks became stronger and sharper at $1250^{0}C$. It is further observed from the XRD pattern that at $1100^{0}C$, the d- spacing of HA in HZ12 composite shifts to a higher value (d= 2.82 A^{o}) with respect to pure HA (d = 2.81A^{o}). Thus, in presence of TZP, HA decompose to produce Ca-deficient HA, TCP and free CaO. The resulting free CaO reacts with TZP to form $CaZrO_3$. It is also possible that some CaO may dissolve in TZP lattice thereby changing it to cubic ZrO_2.

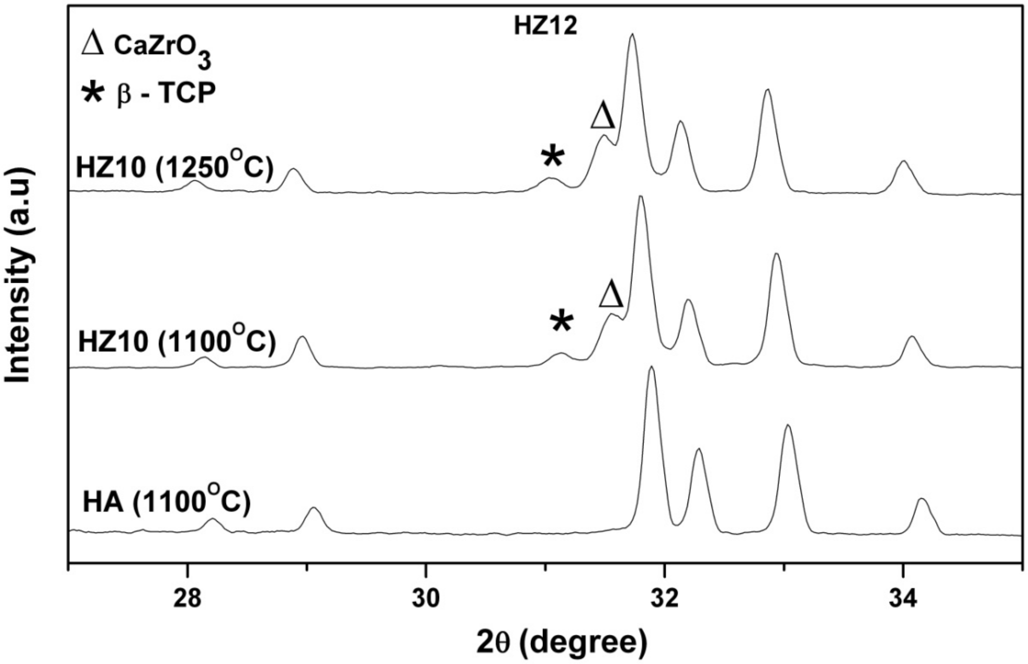

Fig.5.36. XRD pattern of HA and H10Z12 composites

5.5.7 Flexural Strength, Fracture Toughness and Hardness of Sintered HA and HA-TZP Composites

Flexural strength

Figure 5.37 shows the three point bending strength of HA-TZP composites as a function of TZP content. Curve (a) is for HZ8 series and curve (b) is for HZ12 series. The detail of curve (a) has been discussed in section 5.3.7 (Fig. 5.24). The sharp rise in strength at 2 weight % TZP composition is due to some phenomenon over and above the normal densification effect. This type of sharp increase in strength and hardness has also been observed by others [5.13] while working in similar systems. However, it is interesting to note that when TZP is calcined at 1200^{O}C (curve b) the strength behaviour changes dramatically. The bending strength increases more gradually with TZP content, from 35 MPa (pure HA) to 46 MPa at 2 wt % TZP addition. Thereafter, strength does not change appreciably between 2 to 7.5 wt% TZP compositions. Finally, at 10 wt% TZP addition, the strength increases sharply to 65 MPa.

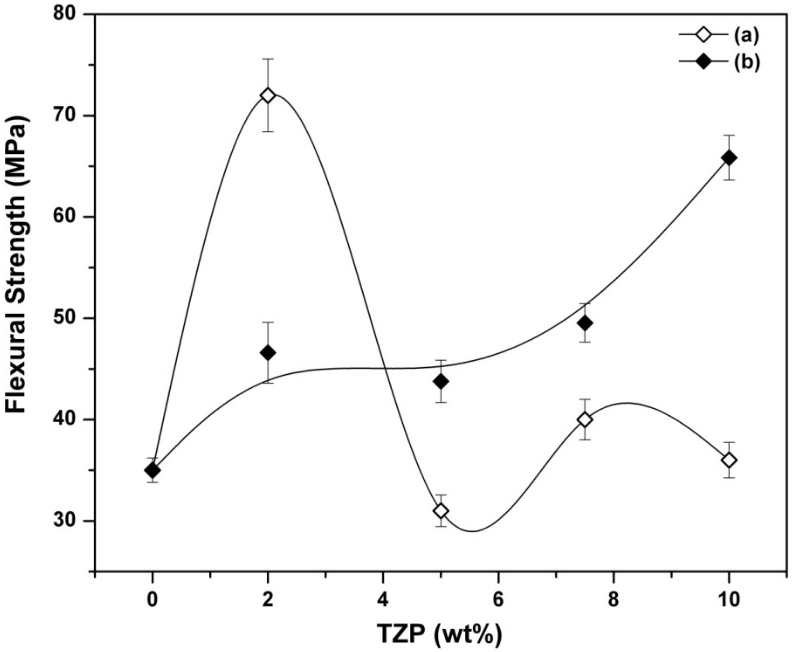

Fig.5.37. Flexural strength of HZ8 and HZ12 composite as a function of TZP content

The XRD pattern of sintered HA- TZP (HZ12 series) shows that maximum $CaZrO_3$ is observed at 10 wt% TZP addition (Table 5.7). Thus it appears that $CaZrO_3$ helps to strengthen composites.

Table 5.7 Relative X-ray intensity (%) of $CaZrO_3$ in HZ12 composites as a function of TZP content

Composition	**$CaZrO_3$ (%)**
HZ2	trace
HZ5	trace
HZ7	9.5
HZ10	14.59

Fracture toughness

Figure 5.38 shows the fracture toughness of HA-TZP composites as a function of TZP content. As mentioned previously, curve (a) refers to HZ8 series and curve (b) relates to HZ12 series composites. In the HZ8 series, the fracture toughness increases with TZP content, reaches a peak at H5Z8 composition and thereafter decreases for H7Z8 and

H10Z8 composites. Curve (b) (HZ12 series) on the other hand shows that the toughness increases from its base value (0.65 MPam^{½}) to 1.09 MPam^{½} at H2Z12 composition and thereafter essentially remains constant between H5Z12 and H7Z12. However, the toughness further increases to 1.6 MPam^{½} at H10Z12 composition.

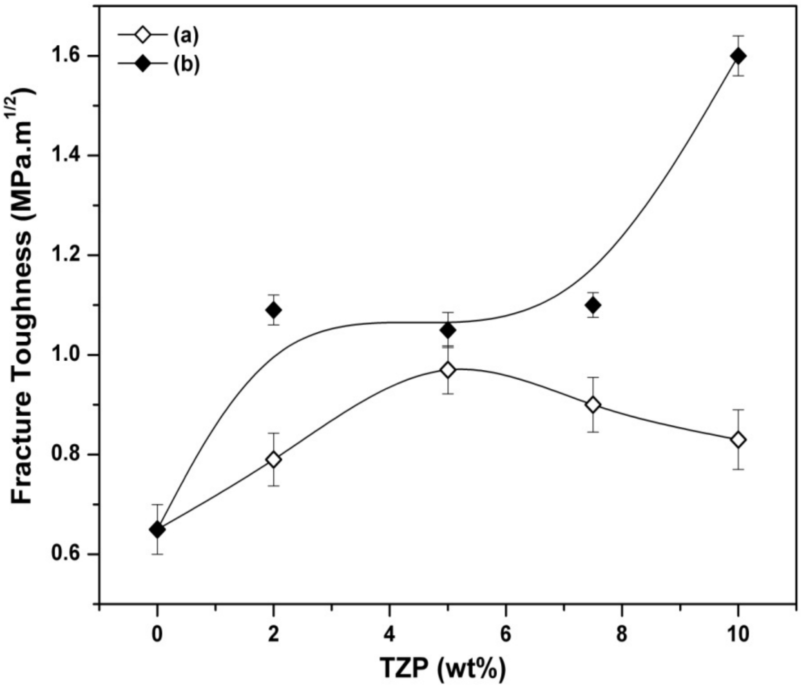

Fig.5.38. Fracture toughness of HZ8 and HZ12 composite as a function TZP content.

According to the established transformation toughening theories [5.24], low elastic modulus of HA will not permit the stress induced transformation of t-ZrO_2. Thus, transformation toughening is not expected to be major cause for toughness enhancement. In order to understand the possible toughening mechanism, the nominal flaw size was calculated using the equation $K_{IC} = Y\sigma_f(c^{1/2})$. The nominal flaw size value for the cases (a) and (b) are tabulated below (Table 5.8).

Table 5.8 Nominal flaw size as a function of TZP content in HA-TZP composites

	Y^2C (μm)	
	HZ8 (Curve a)	**HZ12 (Curve b)**
HZ2	120	540
HZ5	970	570
HZ7	500	490
HZ10	530	590

Table 5.8 shows that in case of HZ8 composites, the estimated flaw size is minimum for H2Z8 and maximum for H5Z8. If the strength is controlled by size of the largest flaw then highest strength will be for H2Z8 composite and lowest for H5Z8. The measured strength is highest for H2Z8 (72 MPa) and lowest for H5Z8 (30 MPa) composites. Thus in HZ8 series composite, strength appear to be controlled by processing flaw size. Since H7Z8 and H10Z8 have same flaw size (500 μm and 530 μm respectively) and their strength values are also comparable. On the other hand the fracture toughness trend suggests that microcrack toughening may be contributing to toughness. The trend in K_{IC} is very similar to that obtained by Swain et.al [5.18]. In case of (b), i.e. when $1200^{O}C$ calcined TZP is introduced in HA matrix, the computed flaw size remains almost constant for 2, 5 and 7.5 wt% TZP addition and increases (although by small magnitude) for 10 wt% TZP addition. Thus it appears in this case, the strength and toughness are not flaw controlled and as indicated earlier, the presence of another phase ($CaZrO_3$) appears to be responsible for the strength and toughness improvement at higher TZP addition.

In an attempt to understand the possible toughening mechanism, Figure 5.39(a) shows the XRD graph of HA-10 wt% TZP compact (HZ12) sintered at $1000^{0}C$, followed by XRD of the same pellet sintered at $1250^{0}C$/4hour. For comparison another pellet of same composition was sintered at $1250^{0}C$ for 4 hours. Figure 5.39(b). The XRD of the ground powder shows the presence of α-TCP along with β-TCP phase in case of powder, where as the pellet shows only β-TCP along with $CaZrO_3$. It could be concluded from the above observation that owing to the increased density of the composite (which in turn increases the matrix constraint) the transformation of β-TCP to α-TCP (associated with a volume change) is suppressed. However, this may cause an increase in the strain in the matrix surrounding the β –TCP grains and may lead to the generation of microcracks under crack opening condition. Thus, this transformation near crack zone may lead to micro crack toughening effect.

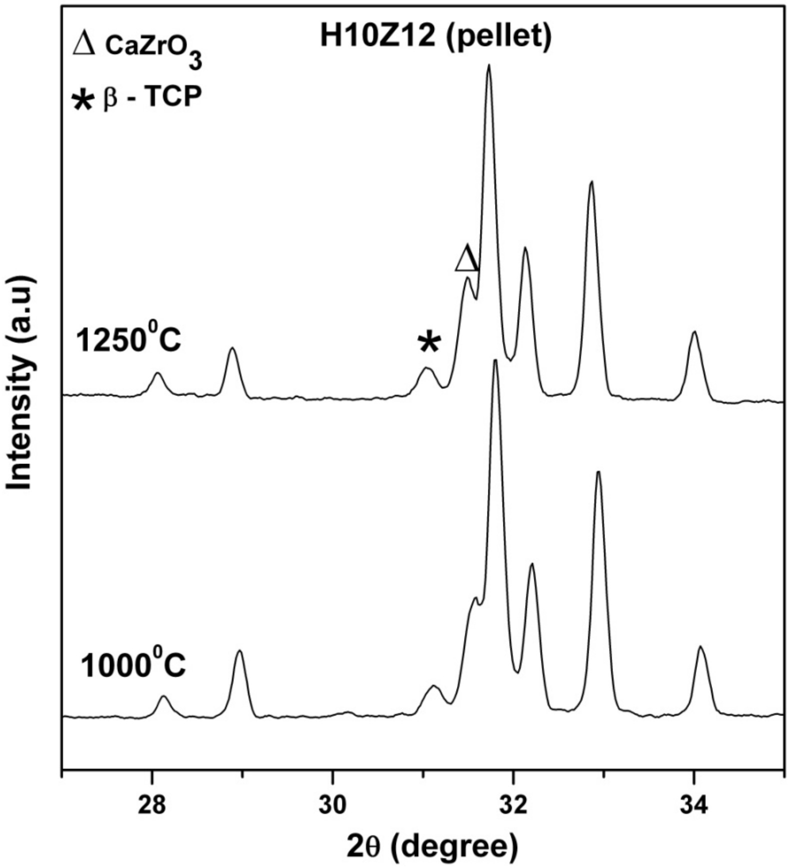

Fig.5.39(a). XRD pattern of H10Z12 composite sintered at 1000^{O}C and 1200^{O}C

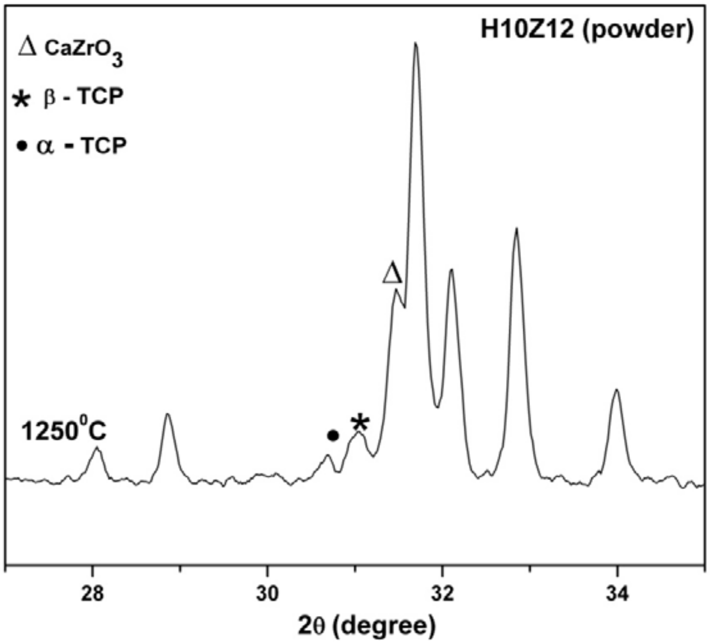

Fig.5.39(b). XRD pattern of crushed powder of sintered H10Z12 composite

Vickers Hardness

Figure 5.40 shows the variation of Vickers hardness for the two types of composites (HZ8 and HZ12 series). While the former shows a decrease in hardness with TZP addition, the latter shows an increasing trend. The results reflect the change in the sintered density pattern of these two composites.

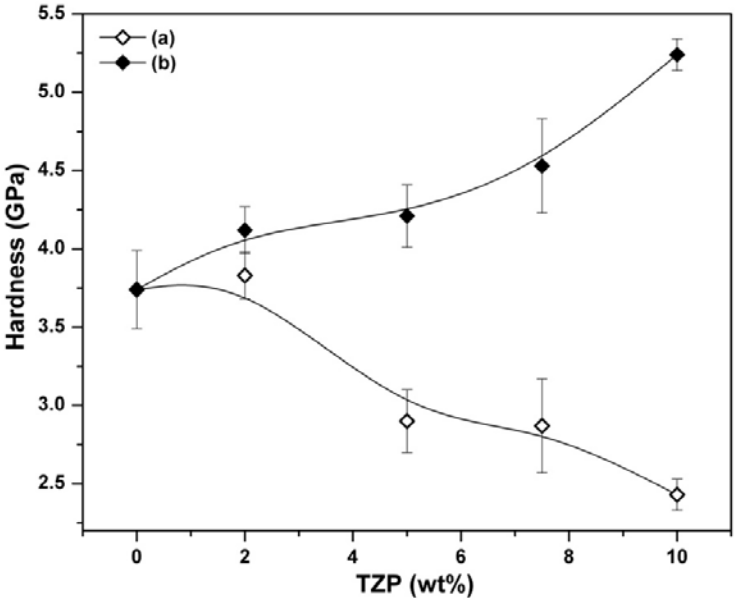

Fig.5.40. Vickers Hardness of HZ8 and HZ12 composite as a function of TZP content

5.6 Conclusions

In the present section, the effect of TZP calcination temperature on HA and TZP phase retention, density and mechanical property was evaluated by introducing TZP calcined at two different temperatures, viz. 850^{O}C and 1200^{O}C for the two different sets of HA-TZP composites (HZ2, HZ5, HZ7 and HZ10). An increase in the calcination temperature of TZP from 850^{O}C -1200^{O}C resulted in density increase for all compositions. The mechanical properties, viz. strength, fracture toughness and hardness show a remarkable improvement H10Z12 composite especially in case of HZ12 batch. However, the use of a higher TZP calcination temperature (HZ12 series) also showed a reduction in HA and TZP phase retention along with the formation of $CaZrO_3$ and TCP. The higher amount of $CaZrO_3$ and TCP was formed due to the combined effect of HA decomposition and the reaction between TZP and HA, initiated by the increased contact between particulate components (i.e. HA and TZP) with improvement in density. Thus these deleterious reaction between HA and TZP could be effectively suppressed or avoided by using a faster and low temperature sintering technique such as hot pressing.

Section D

Phase, Density, Microstructure and Mechanical Properties of Hot Pressed HA-TZP Composites

5.7 Hot Pressing of HA-TZP Composites (both HZ8 and HZ12 series)

Hot Pressing is among one of the widely used method for overcoming the decomposition of HA to TCP as well as to minimize the interaction between HA and TZP (and thereby reduce decomposition of both HA and TZP). Simultaneous application of temperature and pressure during hot pressing permits higher densification of HA – TZP composites at a lower temperature with shorter soaking time. Thus the process permits densification to be completed without either measurable decomposition of HA or reaction between HA and TZP. The hot pressed composite had ≥ 98% relative sintered density as well as optimized phase compositions.

5.7.1 Optimization of Hot Pressing Schedule

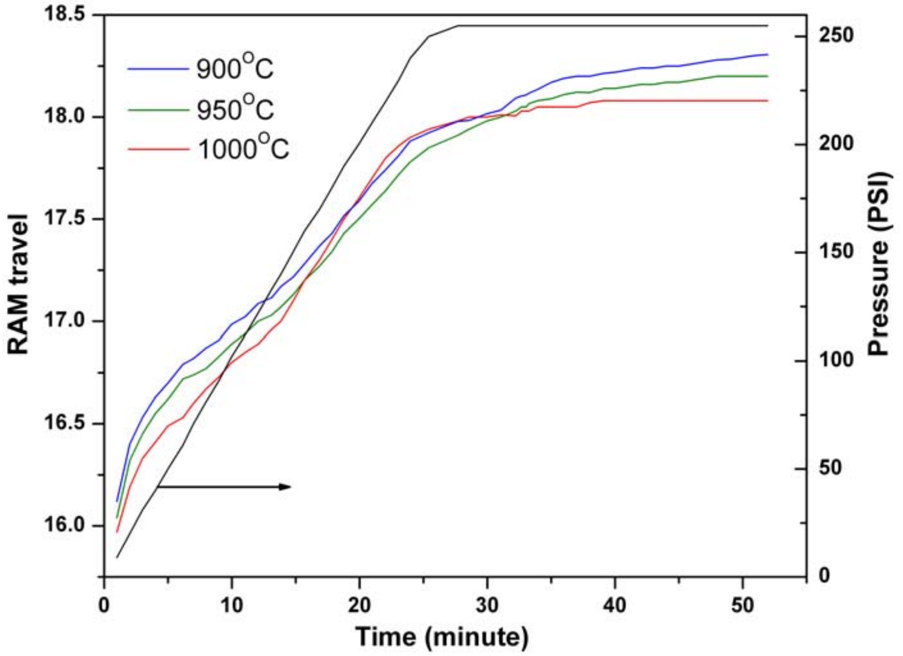

Fig.5.41. Hot pressing of H10Z12 composite at 900^{O}C, 950^{O}C and 1000^{O}C for optimization of hot pressing conditions

The optimization of hot pressing schedule was done by hot pressing H10Z12 (dia = 20mm) composite at three different temperatures (900^{O}C, 950^{O}C, 1000^{O}C) and 30MPa load respectively and monitoring the RAM movement in each case. Figure 5.41 shows the RAM movement as a function of time. The figure reveals that at 1000^{O}C, the densification is almost complete with no significant RAM movement with soaking time.

Whereas, at 950^{O}C there is still some RAM movement, this justifies the 30 minute soaking time required at this temperature for complete densification. However, further reducing the hot pressing temperature to 900^{O}C requires a longer soaking time for complete densification.

5.7.2 Relative Sintered Density of Hot Pressed Compacts

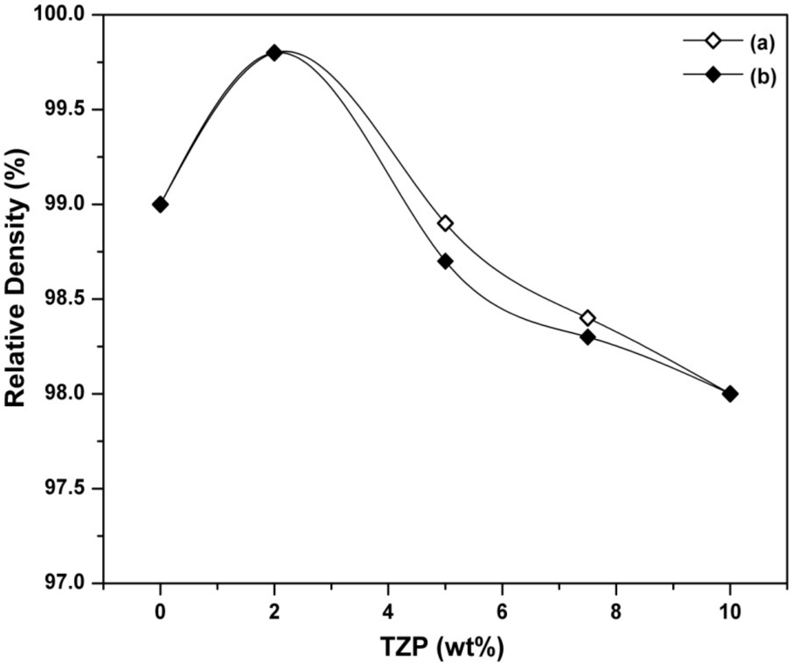

Fig.5.42. Density of hot pressed HA-TZP composite (a) HZ8 (b) HZ12

Figure 5.42 shows the variation in relative sintered density of the hot pressed HA-TZP composites as a function of TZP content. The Figure reveals that the highest sintered density of (>99.5%) is achieved for HZ2 composite, irrespective of TZP calcination temperature (850 or 1200^{O}C). At higher TZP content, the density decreased gradually with minimum density (98%) being recorded for HZ10 composite. The effect of TZP calcination temperature on final density of the hot pressed compact is found to be minimal. The slightly lower density of HZ12 series composite is due to the higher crystallite size of TZP for HZ12 series.

5.7.3 XRD and Phase Analysis of Hot Pressed Specimens

Figure.5.43 shows the XRD of hot pressed HA-TZP composite. Figure 5.43(a) refers to HZ8 series and Fig. 5.43(b) corresponds to HZ12 series. No $CaZrO_3$ peak or in trace amount could be observed in hot pressed HZ8 and HZ12 composites and the phase decomposition of HA was also suppressed. This feature is distinctly different from the pressureless sintered HZ8 and HZ12 series where significant amount of reaction products such as TCP and/or $CaZrO_3$ was observed as a result of higher interaction between HA and TZP components. Another interesting observation of hot pressed composite was the complete absence of β-TCP phase in all the compositions of HZ12 series. But some amount of β-TCP phase was observed in all but one (H2Z8) compositions of the hot pressed HZ8 series composites. Thus the results establish the advantages of using hot pressing for densification of HA-TZP composites.

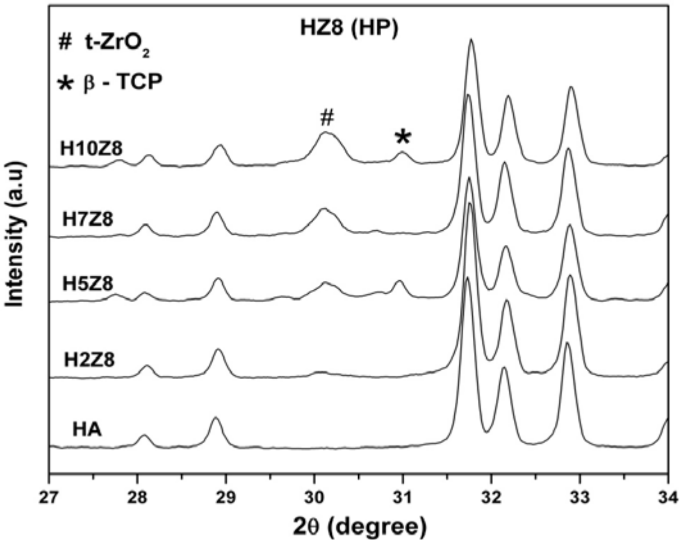

Fig.5.43(a). XRD pattern of hot pressed HZ8 composite

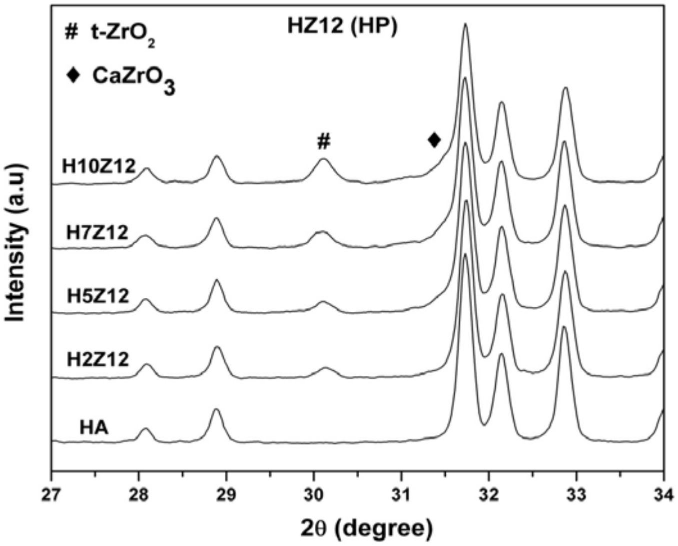

Fig.5.43(b). XRD pattern of hot pressed HZ12 composite

Figure 5.43(c) and 5.43(d) shows comparison in the XRD pattern of hot pressed H10Z8 and H10Z12 composite with their counterpart (air sintered) respectively. In case of H10Z12 composite (Figure 5.43(d)) hot pressing not only avoided the decomposition of HA to TCP due to its low densification temperature but has also reduced the interaction between HA and TZP phase remarkably, thus helping in retaining the TZP phase.

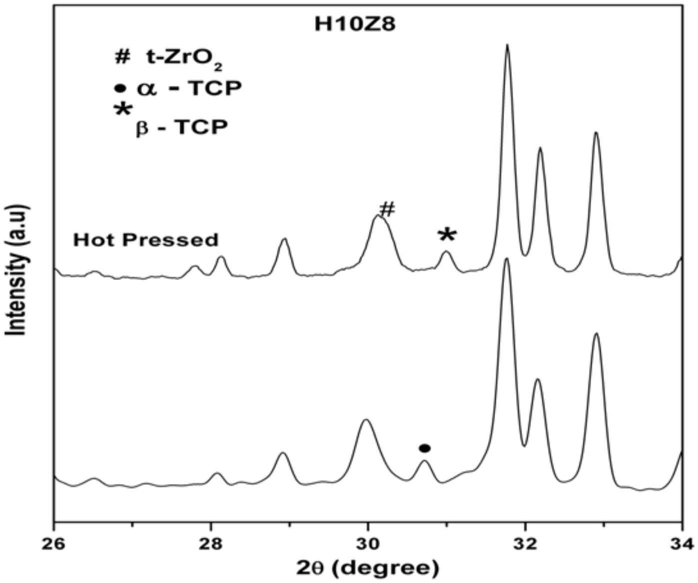

Fig.5.43(c). XRD pattern of hot pressed and air sintered H10Z8 composite

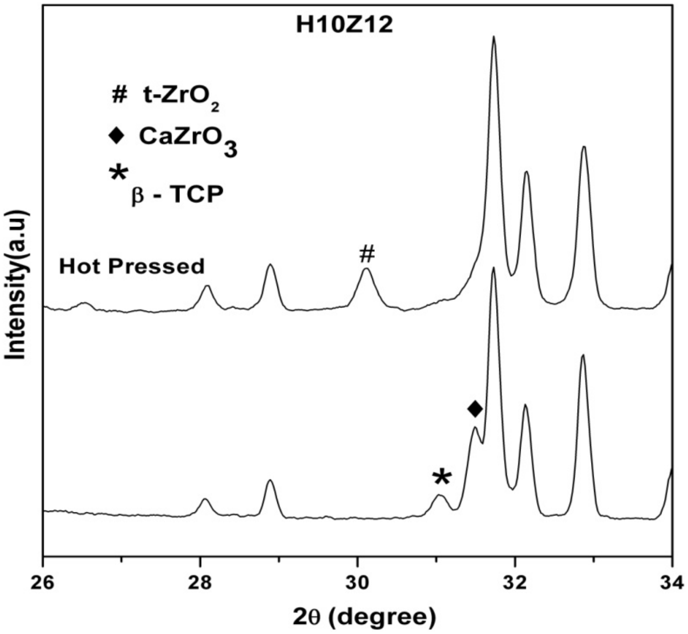

Fig.5.43(d). XRD pattern of hot pressed and air sintered H10Z12 composite

5.7.4 Microstructural Analysis and Grain Size Distribution of Hot Pressed H10Z12 Composite

Figure 5.44 shows the microstructure of hot pressed H10Z12 composite. The average grain size of HA been reduced from around 1.5 μm (for H10Z8 composite) and 10 μm (for H10Z12 composite) to around 0.2μm for hot pressed sample.

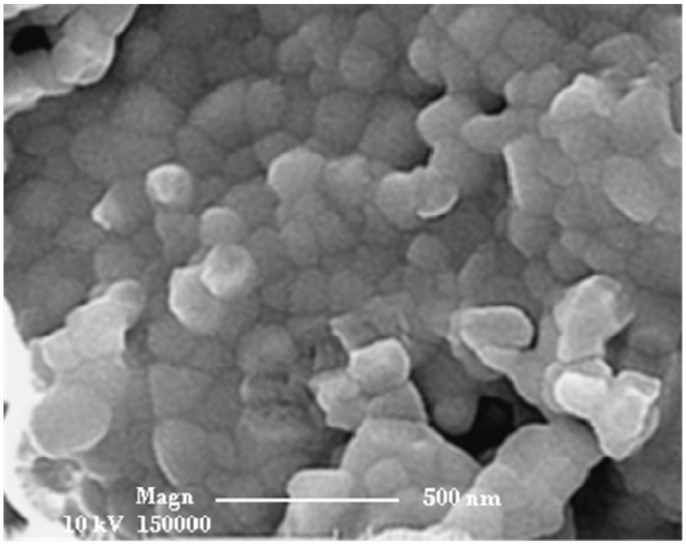

Fig.5.44. FESEM microstructure of hot pressed H10Z12 composite (950^0C for 30 minutes)

The grain size distribution is nearly monomodal as shown in Fig 5.45. So hot pressing not only helps in reducing the grain size but also the grain size distribution span.

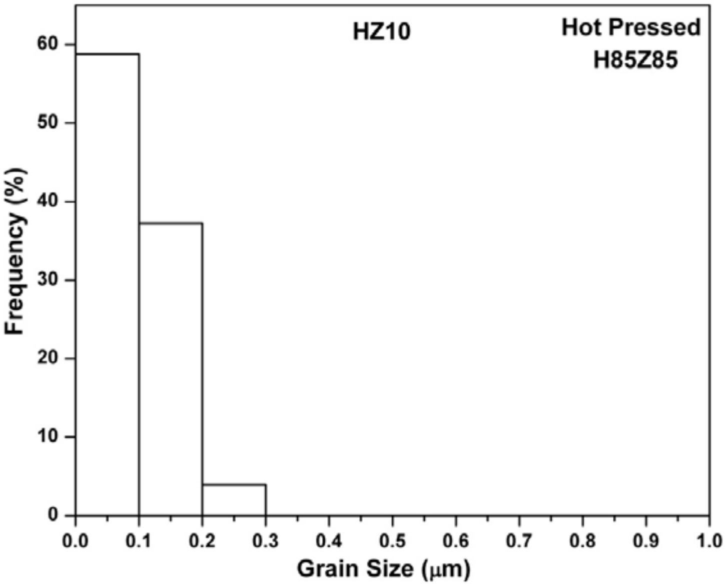

Fig.5.45. Grain size distribution of HA in hot pressed H10Z12 composite

5.7.5 Flexural Strength, Fracture Toughness and Hardness of Sintered HA and HA-TZP Composites

Flexural strength

The significant effect of hot pressing on the density and subsequently on the final mechanical property of the hot pressed composite was found to be interesting. Figure 5.46 shows the flexural strength of hot pressed composites as a function of TZP content for 850^{O}C (HZ8) and 1200^{O}C calcined (HZ12) TZP powder. Maximum strength of 120 MPa was obtained for 2 wt% TZP (H2Z8 composite) addition and further addition of TZP resulted in the reduction of strength value. Similar strength and hardness trend has also been observed by others [5.13] for HA-TZP based systems. However, all the compositions for HZ12 series show a lower strength value as compared to HZ8 series with maximum strength of 93 MPa being recorded for H2Z12 composition. This effect may be due to the lower grain size of HZ8 series as compared to HZ12 series. But at this moment, SEM pictures of HZ8 series of composites are not available with us to prove this point. However, H10Z12 microstructure shows residual porosity in the sample which might have caused lower strength of HZ12 series.

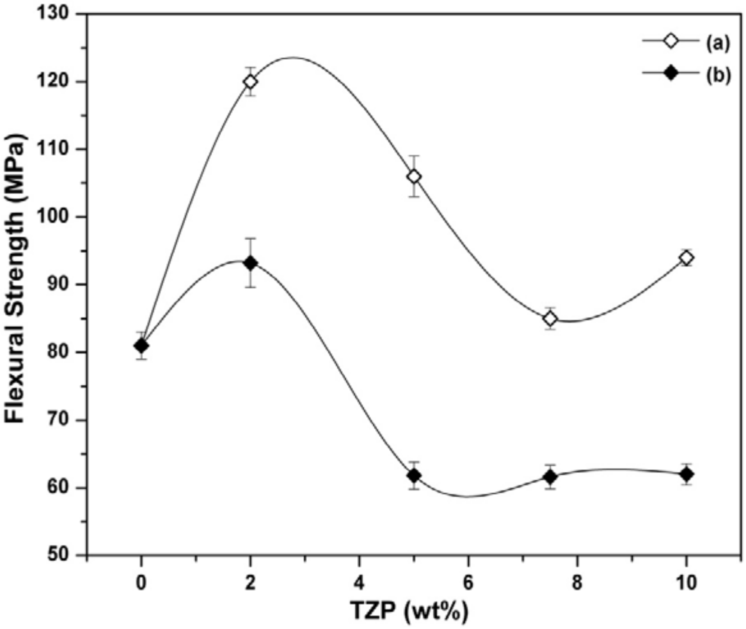

Fig.5.46. Flexural strength of hot pressed HA-TZP composite (a) HZ8 and (b) HZ12 batch

Fracture Toughness

Figure 5.47 shows the fracture toughness of hot pressed HA – TZP composites as a function of TZP content for different calcination temperature of TZP. For HZ8 batch, the trend of toughness variation was similar to that of strength variation. However, for all the hot pressed compositions, the toughness increment was considerably above that obtained for hot pressed HA. The toughness shows a peak at 2 wt% TZP compositions. On the other hand for HZ12 batch, the toughness, gradually increases for all the compositions and reaches a maximum value (1.5 MPa√m) at 10 weight % TZP addition.

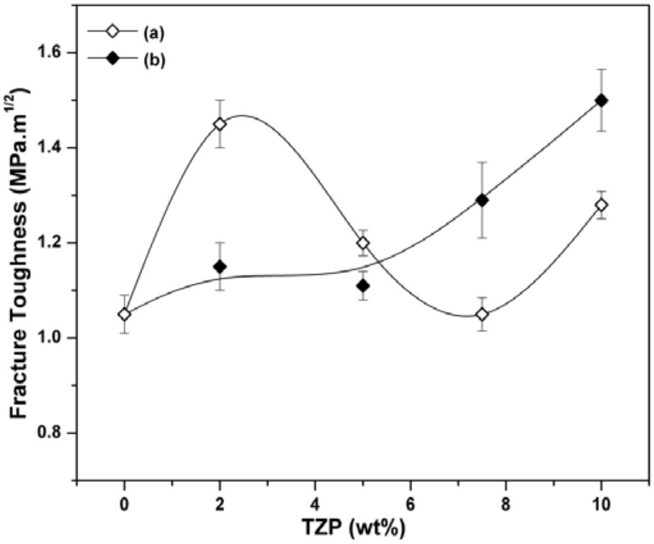

Fig.5.47. Fracture Toughness of hot pressed HA-TZP composite (a) HZ8 and (b) HZ12 batch

Hardness

The Vickers hardness for HZ8 batch (Fig. 5.48) show similar trend to fracture toughness and strength with peak hardness value (5.8 GPa) being recorded at 2 weight% TZP addition followed by a sharp fall at HZ5 composition, attributed to the sharp decrease in density. However, it shows an increasing trend with further TZP addition. Bulk property of TZP may be playing a major role here. For HZ12 batch, the hardness virtually remains constant around 4.75 GPa. The hardness variation of HZ8 samples may be attributed to the presence of varying amount of β-TCP. In HZ12 samples no β-TCP is found but $CaZrO_3$ is observed thus we feel that this particular phase combination is responsible for the nearly constant hardness of HZ12 samples.

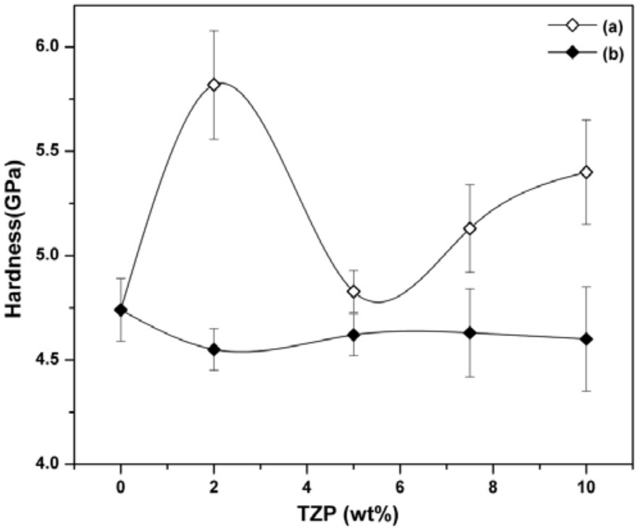

.Fig.5.48. Vickers hardness of hot pressed HA-TZP composite (a) HZ8 and (b) HZ12 batch

The mechanical properties of both pressureless sintered and hot pressed HA and HA-TZP composite prepared by RS route are correlated to the actual mechanical properties of human cortical and cancellous bone (Table 5.9).

Table 5.9 Correlation of mechanical property with actual mechanical property of human cortical bone.

Mechanical Property	Literature value		Present work			
	Cortical Bone	Cancellous Bone	HA	HA (Hot pressed)	HA-TZP	HA-TZP (Hot pressed)
Flexural Strength (MPa)	50-150	10-20	13	80	72 (H2Z8)	120 (H2Z8)
Fracture Toughness ($MPam^{1/2}$)	2-12	-	0.65	1.05	1.6 (H10Z12)	1.5 (H10Z12)
Hardness (GPa)	0.43 ± 0.13	0.46 ± 0.08	3.74	4.75	5.24 (H10Z12)	5.8 (H2Z8)

From the Table, it is seen that the addition of 2 weight % TZP increases the flexural strength of HA-TZP composites close to that of natural bone. The toughness also increases but it compares well with the lower limit of the toughness value of cortical bone. However, the hardness is much higher than the natural bone. So, it can be said that the addition of TZP to HA improves all the mechanical properties of the composite and it is comparable or better than natural bone.

5.8 Conclusions

The reactions between HA and TZP could be effectively suppressed or avoided by using a faster and low temperature sintering technique such as hot pressing. A density of > 98% was observed for all the hot pressed compacts. Increase in composite density along with retention of HA and TZP phase has significant effect on the mechanical properties of the composite. The maximum flexural strength (120 MPa) and hardness (5.8GPa) obtained for HZ2 composite containing TZP calcined at $850^{O}C$ (H2Z8) was significantly higher than any other HA-TZP composition studied here. The toughness value is maximum (1.5 MPa√m) for HZ10 composite containing TZP calcined at $1200^{O}C$ (H10Z12). In addition to this a sharp decrease in HA grain size (200nm) was noticed for hot pressed compacts.

References

5.1. A. Balamurugan, J. Michel and J. Faure, "Synthesis and structural analysis of sol gel derived stoichiometric monophase hydroxyapatite", Ceramics-Silikaty., 50, 27-31 (2006).

5.2. R. Murugan and S. Ramakrishna, "Effect of zirconia on the formation of calcium phosphate bioceramics under microwave irradiation", Materials letters., 58, 230 – 234 (2003).

5.3. A. O. Keskin, F. C. Sahin and O. Yucel, "Sintering and mechanical properties of hydroxyapatite-zirconia composite ceramics", Key Engineering Materials, 206-213, 1629-1632 (2002).

5.4. Y. Genc, F. N. Oktar, E. Z. Erkmen, G. Goller, D. Toycan and H. Haybat, "Sintering effect on mechanical properties of enamel derived and synthetic hydroxyapatite-zirconia composites", Key Engineering Materials, 264-268, 1961-1964 (2004).

5.5. H. W. Kim, Y. J. Noh, Y. H. Koh, H. E. Kim and H. M. Kim, " Effect of CaF_2 on densification and properties of hydroxyapatite-zirconia composites for biomedical applications", Biomaterials, 23, 4113-4121 (2002).

5.6. E. Adolfsson and Z. Shen, "Densification of zirconia-hydroxyapatite ceramics without phase changes", Key Engineering Materials, 309-311, 1141-1144 (2006).

5.7. E. Adolfsson, M. Nygren and L. Hermansson, "Decomposition mechanism in aluminium oxide-apatite systems", Journal of American Ceramic Society, 82, 2909 (1999).

5.8. R. B. Heimann and T. A. Vu, "Effect of CaO on thermal decomposition during sintering of composite hydroxyapatite-zirconia mixture for monolithic bioceramic implants", Journal of Materials Science Letters, 16, 437-439 (1997).

5.9. R. Kumar, K. H. Prakash, P. Cheang and K. A. Khor, "Microstructure and mechanical properties of spark sintered zirconia-hydroxyapatite nano - composite powders, Acta Materialia, 53, 2327- 2335 (2005).

5.10. Z. Evis, "Reactions in hydroxylapatite-zirconia composites", Ceramics international, 33, 987-991 (2007).

5.11. J. M. Wu and T. S. Yeh, "Sintering of hydroxylapatite-zirconia composite materials", Journal of Materials Science, 23, 3771-3777 (1988).

5.12. R. R. Rao and T. S. Kannan, “Synthesis and sintering of hydroxyapatite-zirconia composites”, Materials Science and Engineering C, 20, 187-193 (2002).

5.13. E.S. Ahn, N.J. Gleason and J.Y. Ying, “The effect of zirconia reinforcing agents on the microstructure and mechanical properties of hydroxyapatite - based nanocomposites”, J. Am. Ceram. Soc, 88, 3374-3379 (2005).

5.14. T. P. Hoepfner and E. D. Case, “An estimate of the critical grain size for microcracks induced in hydroxyapatite by thermal expansion anisotropy”, Materials Letters, 58, 489-492 (2004).

5.15 M. R. Towler, I. R. Gibson, “The effect of low level of zirconia addition on the mechanical properties of hydroxyapatite”,, Journal of Materials Science letters, 20, 1719- 1722 (2001).

5.16. H. Y. Yasuda, S. Mahara, Y. Umakoshi, S. Imazato and S. Ebisu, “Microstructure and mechanical property of synthesized hydroxyapatite prepared by colloidal process”, Biomaterials, 21, 2045-2049 (2000).

5.17 Ceramic Microstructures, W. E. Lee, chapter 2, , page 67-121, Chapman & Hall,1994.

5.18. M. V. Swain, “Inelastic deformation of Mg-PSZ and its significance for strength–toughness relationship of zirconia-toughened ceramics”, Acta Metall., 33, 2083-91(1985).

5.19. W. E. Lee and M. Rainforth in Ceramic Microstructures: Property Control Through Processing, pp 225-227, 1st ed, Chapman &Hall, 1994, London.

5.20. W. Pyda, A. Slosarczyk, M. Haberko, Z. Paszkiewicz, A. R. Kmita and A. Pyda, “Effect of chemical composition and morphology of zirconia particles on properties of HAp-zirconia particulate composites”, Key Engineering Materials, 206-213, 1567-1570 (2002).

5.21. Y. Nayak, R.P. Rana, S.K. Pratihar and S. Bhattacharyya, “J. Mater. Sci.: Mater. Med, 19, 2437 (2008).

5.22. F.F. Lange, “Powder processing science and technology for increased reliability”, Journal of American Ceramic. Society, 72, 3 (1989).

5.23. M. Tamai, K. Sakamoto, S. Yamaguchi and A. Nakahira, “Transmission electron microscopy study on the migration of calcium ions in Ca-deficient hydroxyapatite during thermal decomposition”, Journal of the Ceramic Society of Japan, 113, 131-134 (2005).

5.24. A. G. Evans, N. Burlingame, M. Drory and W. M. Kriven, “Martensitic transformations in zirconia particle size effects and toughening”, Acta Metall., 29, 447-456 (1981).

Chapter VI

Results and discussions-

In Vitro Tests of HA and HA-TZP Composites

6.1 Biological Evaluation of Sintered HA-TZP Composites *In Vitro*

Several results have demonstrated that those materials which are able to form apatite on their surface in vitro in simulated body fluid (SBF) also shows apatite forming ability in vivo (within the living body) which helps to form a bond with the tissue through this apatite layer. Although there are certain materials which bonds directly to bone without formation of any intermediate apatite layer (e.g. A/W glass ceramic). Thus the utility of SBF treatment lies in getting qualitative idea about the in vivo bone bioactivity of material. This helps in reducing both the number and duration of animal experiment [6.1, 6.2]. However, there are also certain materials such as the natural abalone shell which although shows apatite formation on its surface in an SBF but lacks bone bonding ability in vivo [6.3]. This may be due to any toxic effect or anti body reactions induced by the substance present in the material. Thus, the bio-compatibility of the implant material with the host tissue must be cautiously evaluated by an in vitro cytotoxicity test before going for any animal experiment. Invitro cytotoxicity test determines if the material is toxic in contact with reference to a particular cell line (such as L929 mouse fibroblasts). It has also been reported that a particular material may be compatible to bone tissue but the same material may not be compatible to direct blood contact. Hence, the need for a blood compatibility test is also necessary. One such test is being termed as in vitro hemocompatibility test in which the blood compatibility of a given material is being tested.

6.1.1 Bioactivity Test

Figure 6.1(a) shows the SEM micrograph of sintered HA after SBF treatment for 5 days. The microstructure shows the formation of distinct Ca-P precipitate on its surface [6.4]. Similar result was also observed for HZ5 (Fig. 6.1(b)) and HZ10 composite (Fig. 6.1(c)) (HZ8) after 5 days of aging in SBF. Thus, TZP addition to HA did not produce any adverse effect on the bioactivity of the composite. After 10 days of SBF treatment, distinct morphological changes of Ca-P precipitate were observed (Fig. 6.1(d)). The precipitates were present in large quantity and were visible even at low magnification as compared to that of five days SBF treated samples (Fig. 6.1(c)). The precipitate morphology changed from fluffy and flower type to globular type. The apatite formation on the surface of composite was confirmed by EDS spot analysis of a number of such globules, which confirmed the presence of Ca and P. Thus, the SBF study demonstrated the increased precipitation of Ca-P with soaking time.

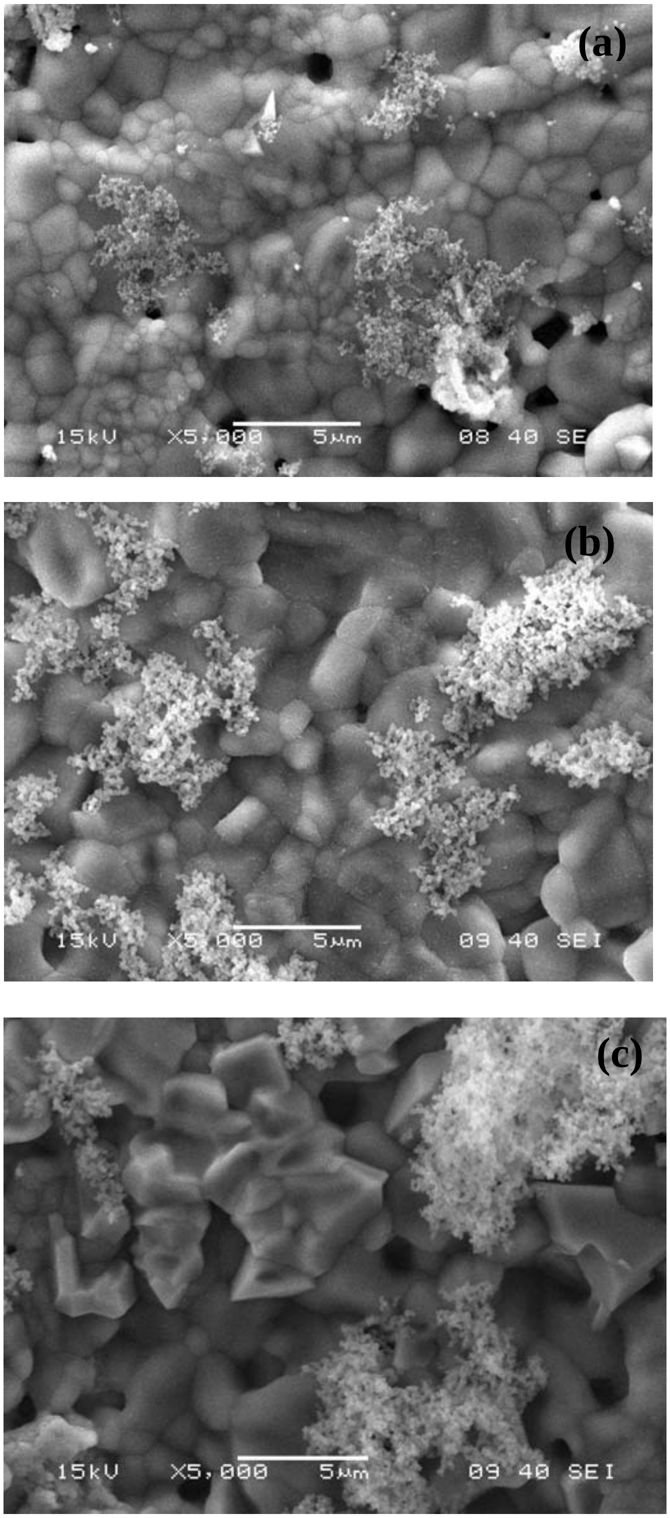

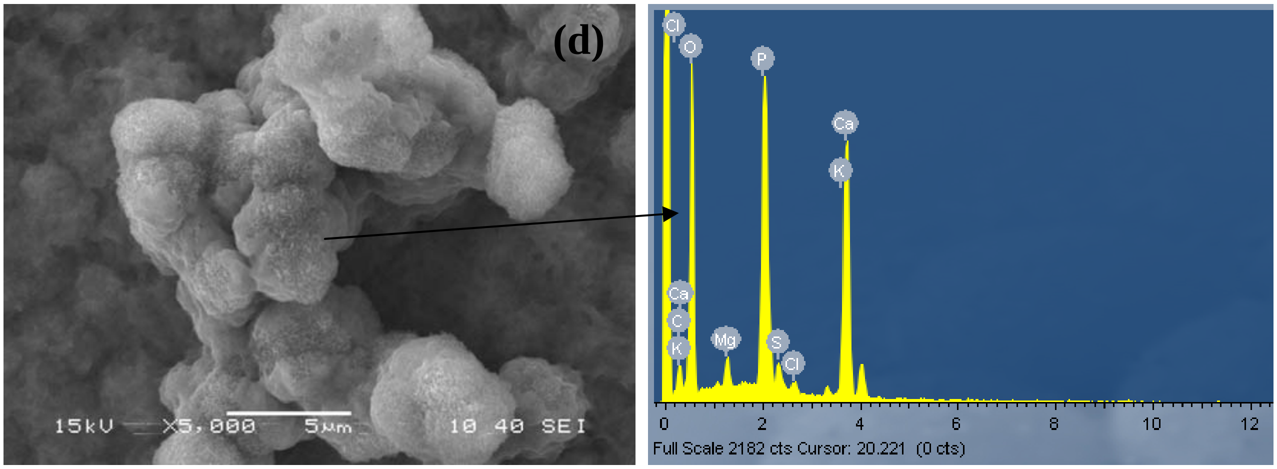

Fig.6.1. SEM of (a) HA, (b) H5Z8 and (c) H10Z8 composite soaked in SBF for 5days (d) H10Z8 composite soaked in SBF for 10 days with EDS analysis.

Figure 6.2(a) and (b) shows the microstructure of 5 days SBF treated HZ12 composites. Figure 6.2(a) is for H5Z12 and 6.2(b) for H10Z12 composite. The microstructure in this case shows near high surface coverage by Ca-P layer. The relative amount and morphology of the apatite did not vary much with the variation of TZP amount. However, in the 10 days SBF treated H5Z12 and H10Z12 samples (Figure 6.2(c) and (d) respectively), quite high amount of Ca-P deposition was observed. The Ca-P deposition in this case was visible even at a lower magnification (200X) (Fig 12(a)). All the compositions of HA-TZP composite showed reasonably good bioactivity (measured in terms of Ca-P precipitate formation) with high surface coverage after 10 days (measured with respect to pure HA). It is thought that the improved bioactivity of HZ12 series composite was due to the presence of TCP in the sintered composite. The bioactivity results thus confirm that the incorporation of TZP does not affect the bioactivity. However, a more thorough study on the detailed physiological aspects of this material needs to be evaluated.

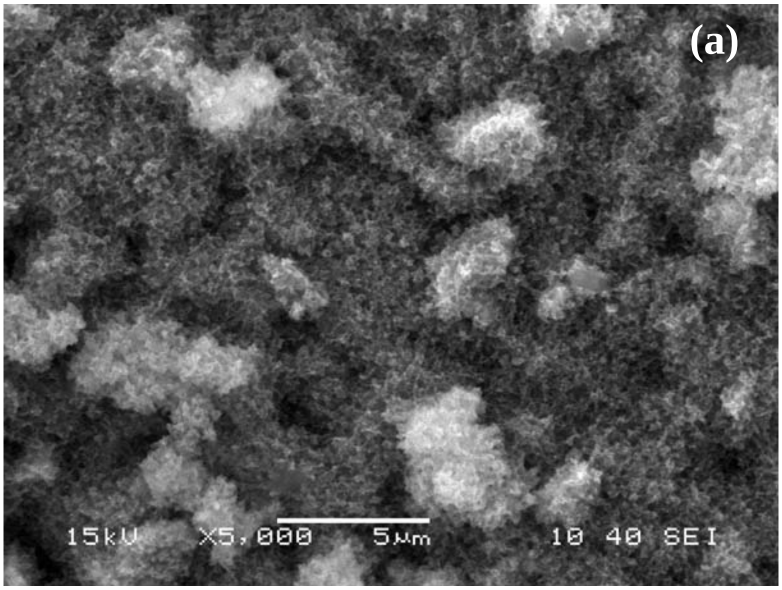
(a)
15kV X5,000 5µm 10 40 SEI

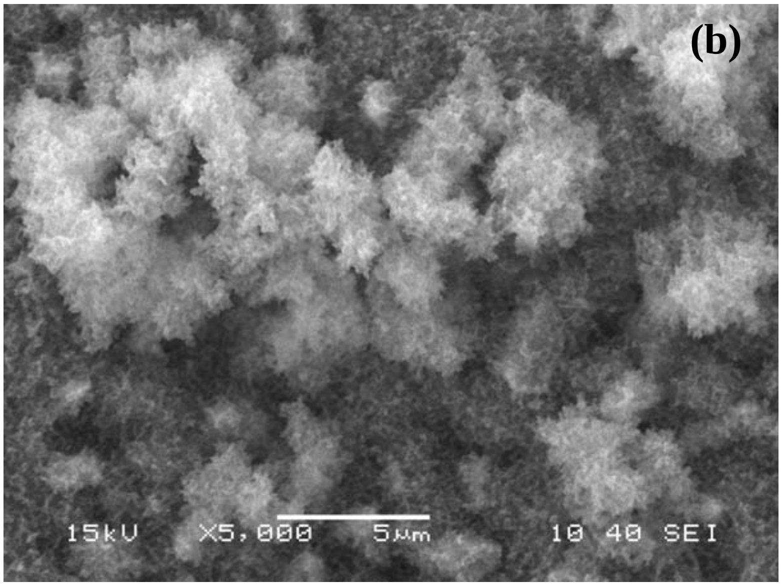
(b)
15kV X5,000 5µm 10 40 SEI

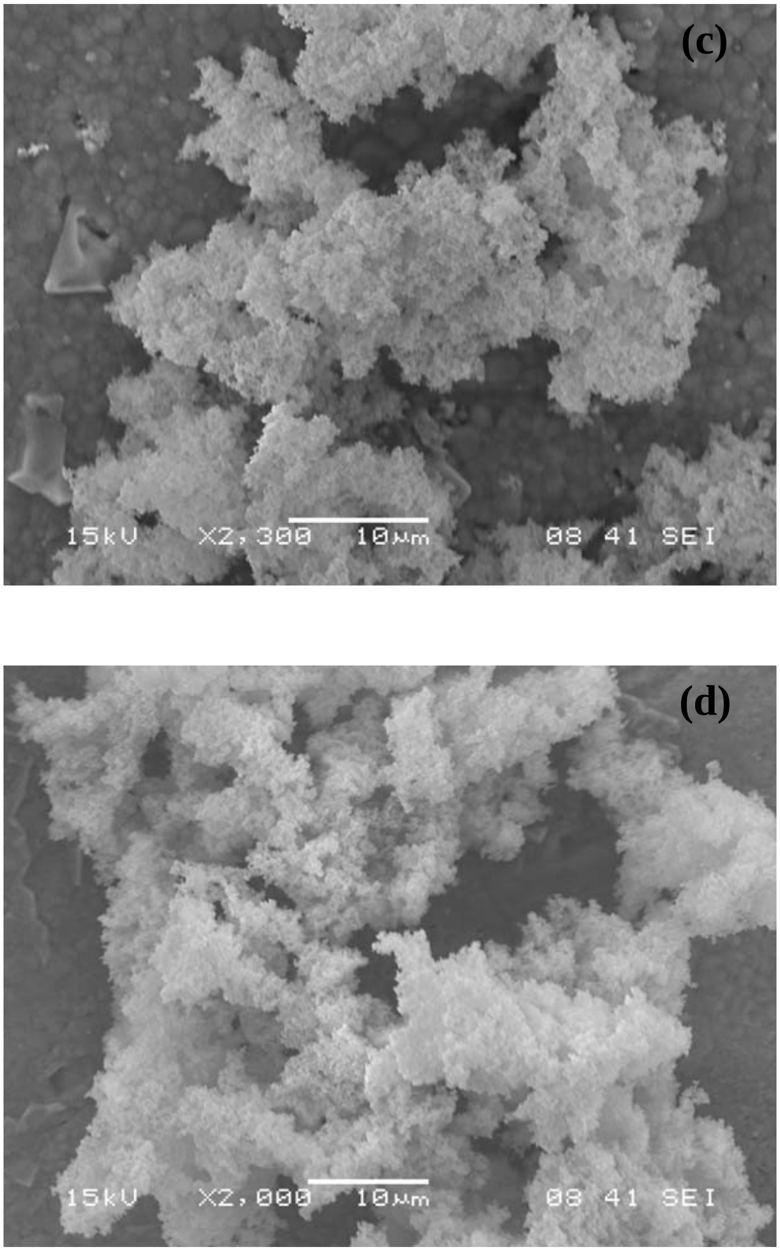

Fig.6.2. SEM of (a) H5Z12 and (b) H10Z12 composite soaked in SBF for 5 days (c) H5Z12 and (d) H10Z12 composite soaked in SBF for 10 days.

The microstructure (Fig. 6.3) of 10 days SBF aged hot pressed HA and HA-TZP composite show a different trend. Figure 6.3(a) shows the microstructure of SBF treated hot pressed HA. Figure 6.3(b) and (c) shows the microstructure for hot pressed H2Z8 and H10Z8 composite after 10 days SBF treatment and Fig. 6.3(d) and (e) are for hot pressed H2Z12 and H10Z12 composites. After 10 days of SBF aging no difference in Ca-P formation was observed with the variation of TZP amount. There was no change in the morphology or type of apatite formation as a function of either TZP amount or TZP calcination temperature. However, in all the hot pressed HA-TZP composites the Ca-P deposition on the surface of the composite was very less and could be observed only at very high magnification (1500X) after 10 days of SBF soaking. This is due to the high density of hot pressed composites. Hence, the hot pressed samples appears to be lesser bioactive in comparison to pressureless sintered HA-TZP composites. In contrast to the XRD pattern of air sintered sample, XRD pattern of hot pressed HA and HA-TZP composite [Figure 5.43 (a) and (b)] did not show any fast resorbing phase (α-TCP) due

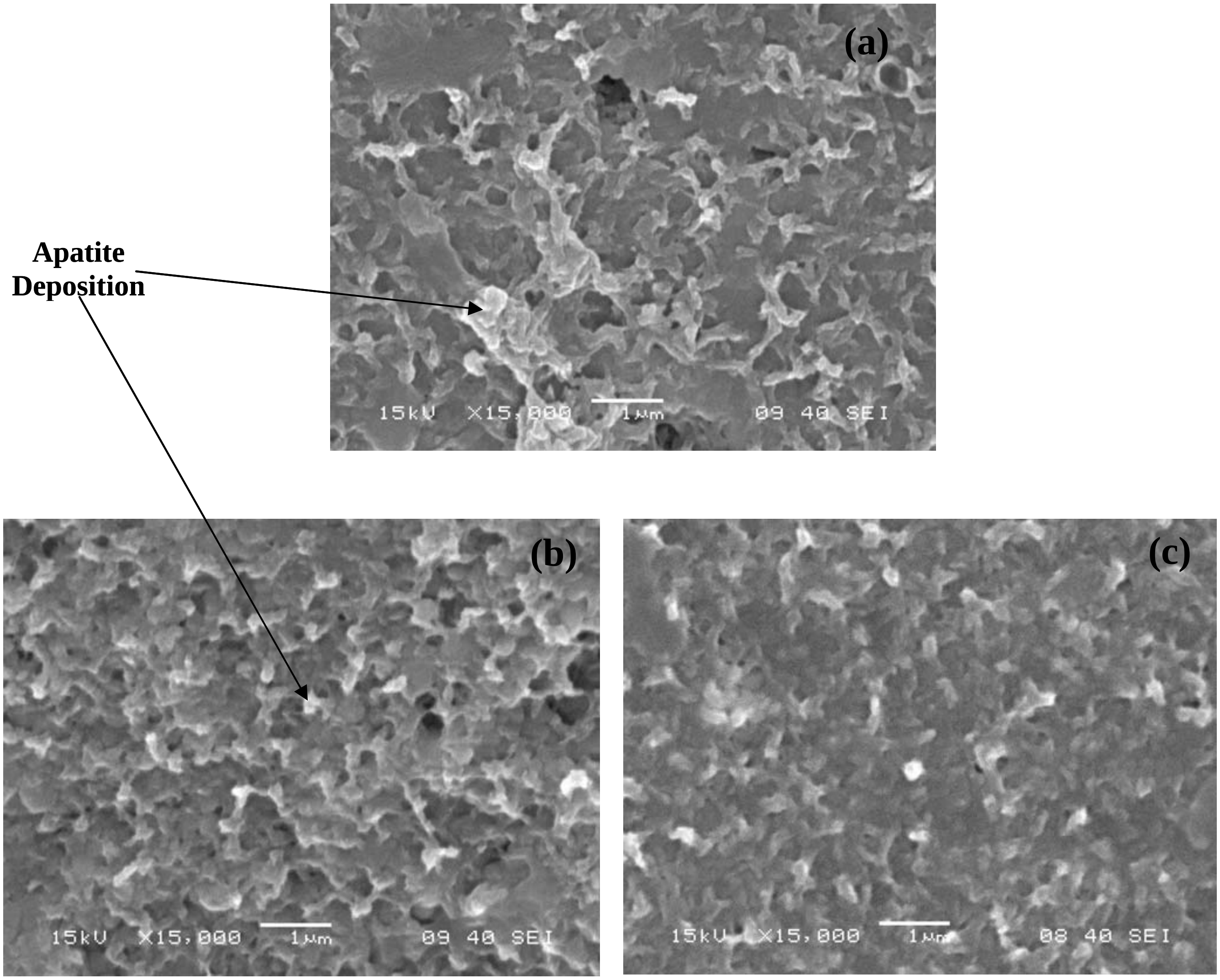

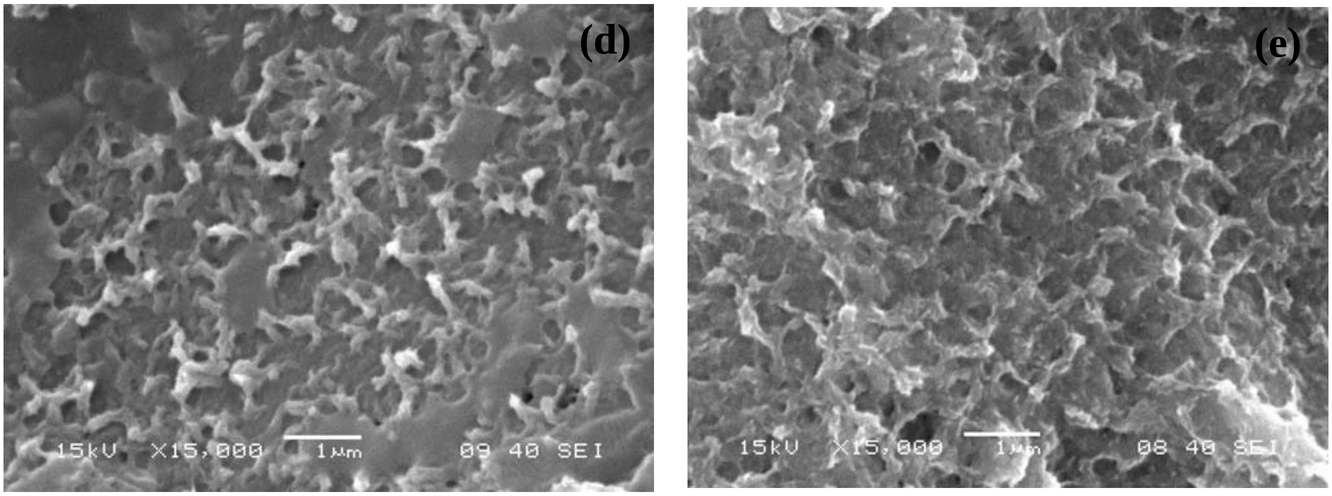

Fig.6.3. SEM of hot pressed (a) HA (b) H2Z8 and (c) H10Z8 composite (d) H2Z12 and (e) H10Z12 composite soaked in SBF for 10 days.

to lower decomposition of HA phase. Table 6.1 shows a qualitative comparison of the different phases (HA, TZP, $CaZrO_3$ and TCP) in hot pressed composites containing 7 wt % TZP (Table 6.1(a)) and 10 wt% TZP (Table 6.1(b)). It has been observed that for all the compositions of hot pressed sample the amount of TCP is virtually negligible. However, in Table 6.1, the x-ray intensity of only two compositions, viz. , HZ7 and HZ10 have been given.

Table 6.1 Relative values of X-ray intensity for air sintered and hot pressed HA-TZP composites (a) HZ7 and (b) HZ10

HZ7	**Air Sintered**		**Hot Pressed**		**HZ10**	**Air Sintered**		**Hot Pressed**	
(a)	**HZ8**	**HZ12**	**HZ8**	**HZ12**	**(b)**	**HZ8**	**HZ12**	**HZ8**	**HZ12**
HA	**high**	**high**	**high**	**high**	**HA**	**high**	**high**	**high**	**high**
TZP	**high**	**zero**	**high**	**high**	**TZP**	**high**	**zero**	**high**	**high**
$CaZrO_3$	**zero**	**high**	**low**	**low**	**$CaZrO_3$**	**zero**	**high**	**zero**	**low**
β-TCP	**Low**	**medium**	**zero**	**zero**	**β-TCP**	**low**	**medium**	**low**	**zero**
α-TCP	**high**	**zero**	**zero**	**zero**	**α-TCP**	**medium**	**zero**	**zero**	**zero**

The presence of TCP in HA helps to exhibit a higher bioactivity as compared to pure HA. As TCP is less in hot pressed HA and HA-TZP composites this contributes to lower nucleating ability of hot pressed HA and HA-TZP composites in SBF. Moreover, during hot pressing, some amount of carbon is incorporated (from graphite foil) in the sample. This (owing to nonthrombogenic property) also contributes to the reduced bioactivity of hot pressed sample.

The compositional variation of apatite formed on the surface of HA and HA-TZP composite after SBF soaking for different time period were seen through EDX analysis.

While no considerable change in apatite composition was observed in any case, the SEM images of the SBF soaked HA and HA-TZP composite shows a distinct variation in the amount of apatite formed as a function of soaking time, TZP content and sintering condition. However, as the focus of this thesis was more on the mechanical aspect of the composite, the biological characterization in particular the kinetics of SBF formation was not taken up with great detail during the course of work. However, a semi-quantitative estimation of the fraction surface coverage by amorphous apatite was found out by measuring the percentage of surface coverage caused by the apatite deposition as shown in Table 6.2.

Table 6.2 Percent surface coverage by apatite as function of aging time in SBF for HA and HA- TZP composites

Composition	Air sintered		Hot pressed
	5 days	10 days	10 days
HA	15	35	10
H5Z8	24.4	47	10.4
H10Z8	25.4	48.9	10.2
H5Z12	25.2	67.7	9.8
H10Z12	30	74	10

However, the XRD is not been able to detect any change in crystallization behavior or phase of the composite (H10Z12) even after 10 days of SBF aging (Figure 6.4). This shows that a longer aging time (> 10 days) is required to see any significant change in the XRD profile of SBF aged HA-TZP composites.

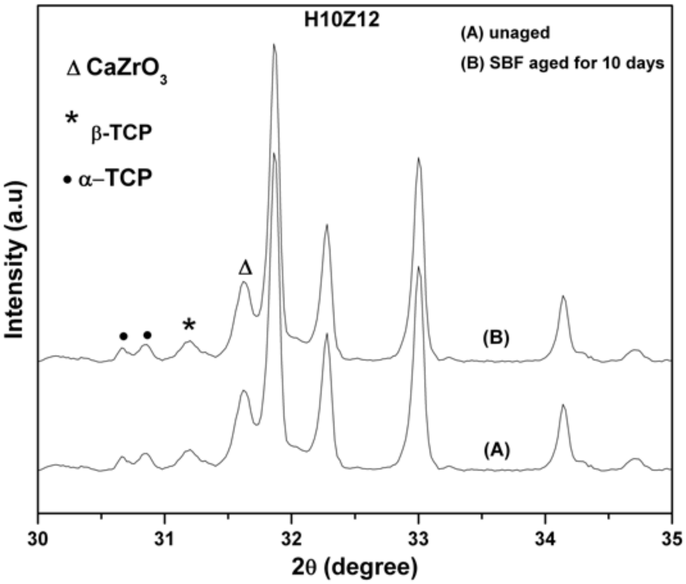

Fig. 6.4. XRD of H10Z12 composite before and after 10 days of SBF aging

6.1.2 In vitro Cytotoxicity Test

The cell viability of the prepared HA and HA-TZP composite were measured by an invitro cytotoxicity test (ISO 10993-5). Figure 6.5 (a) - (e) shows the existence of L 929 mouse fibroblast cells around sintered (1250^{O}C/4 hours) HA and HA-TZP composites after incubation of cells with test samples at 37 ± 1^{O}C for 24-26 hours [6.5]. Figure 6.5(a) shows the microscopic image of proliferated L929 cells around HA, where as Fig. 6.5(b) and (c) shows it for air sintered H2Z8 and H10Z8 composites. The images show the presence of L929 cells around all these samples. Thus the addition of different TZP amount to HA does not have any adverse effect on the cytotoxicity of the composite. Similarly with the change in TZP calcination temperature (air sintered H10Z12 composite), the microstructure did not indicate any significant change in cytotoxicity behaviour (Fig. 6.5(d)). L929 cell lines were present in large number around the sample. The H10Z8 hot pressed sample (Fig. 6.5(e)) also showed presence of cells around sample, thus proving the material to be non toxic. Moreover, the qualitative evaluation made by the microscopic observation (Table 6.3) as per the gradation (section 4.6.5, Table 4.1) shows neither HA nor HA-TZP composites did show any toxic behaviour to fibroblast cells after 24 hours of contact. This implies that the test materials did not show any detectable toxic zone around or under the specimen. As anticipated the positive control gave severe cytotoxicity reactivity where as negative control gave zero cytotoxic reactivity. While we acknowledge that everything is toxic and true toxicity depends on the concentration, the cytotoxicity test in the present work was done at a constant concentration.

Table 6.3 Qualitative evaluation of cytotoxicity result

Sl No	Sample	Grade	Reactivity
1.	Negative Control	0	None cytotoxic
2.	Positive Control	4	Severe cytotoxic
3.	HA (PS)	0	None cytotoxic
4.	H2Z8 (PS)	0	None cytotoxic
5.	H10Z8 (PS)	0	None cytotoxic
6.	H10Z12 (PS)	0	None cytotoxic
7.	H10Z8 (HP)	0	None cytotoxic

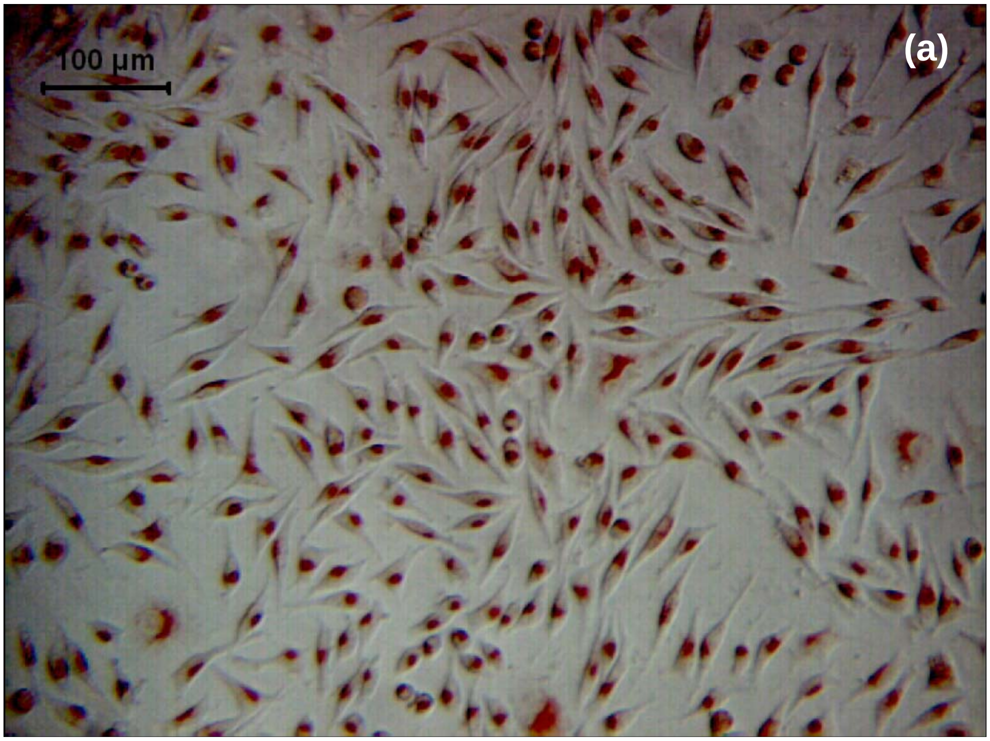

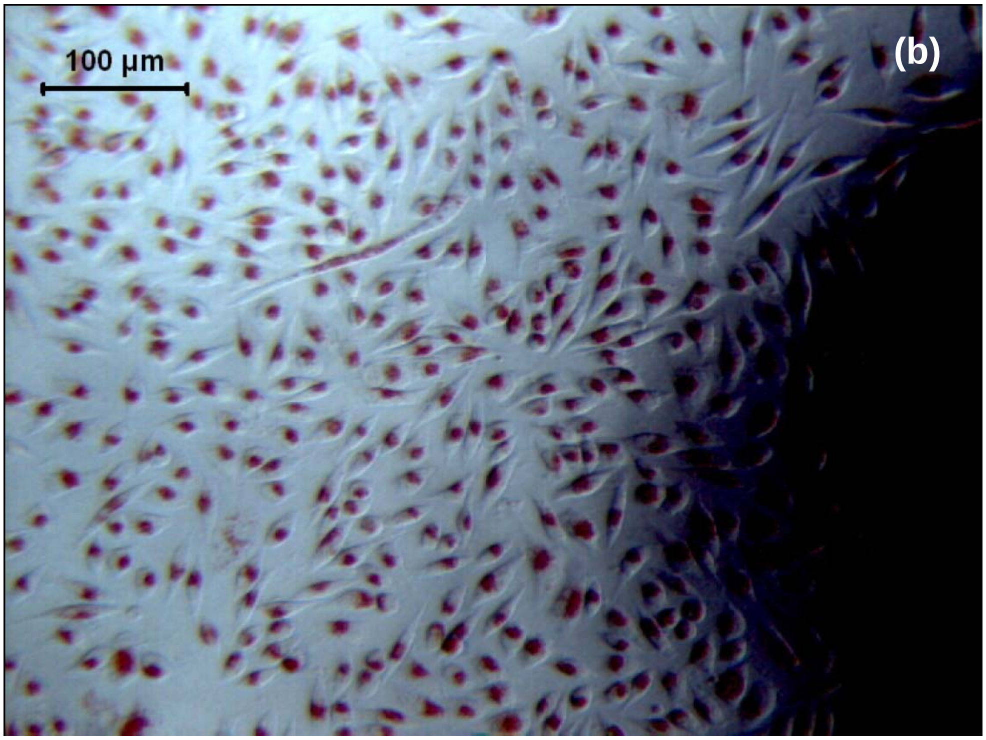
100 µm
(b)

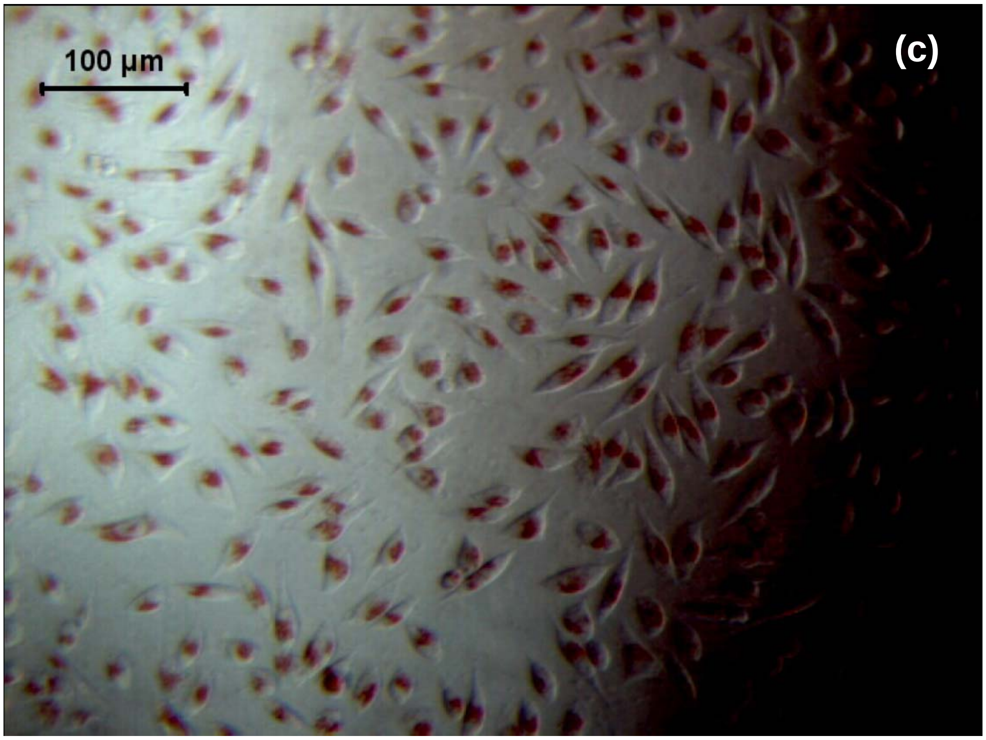
100 µm
(c)

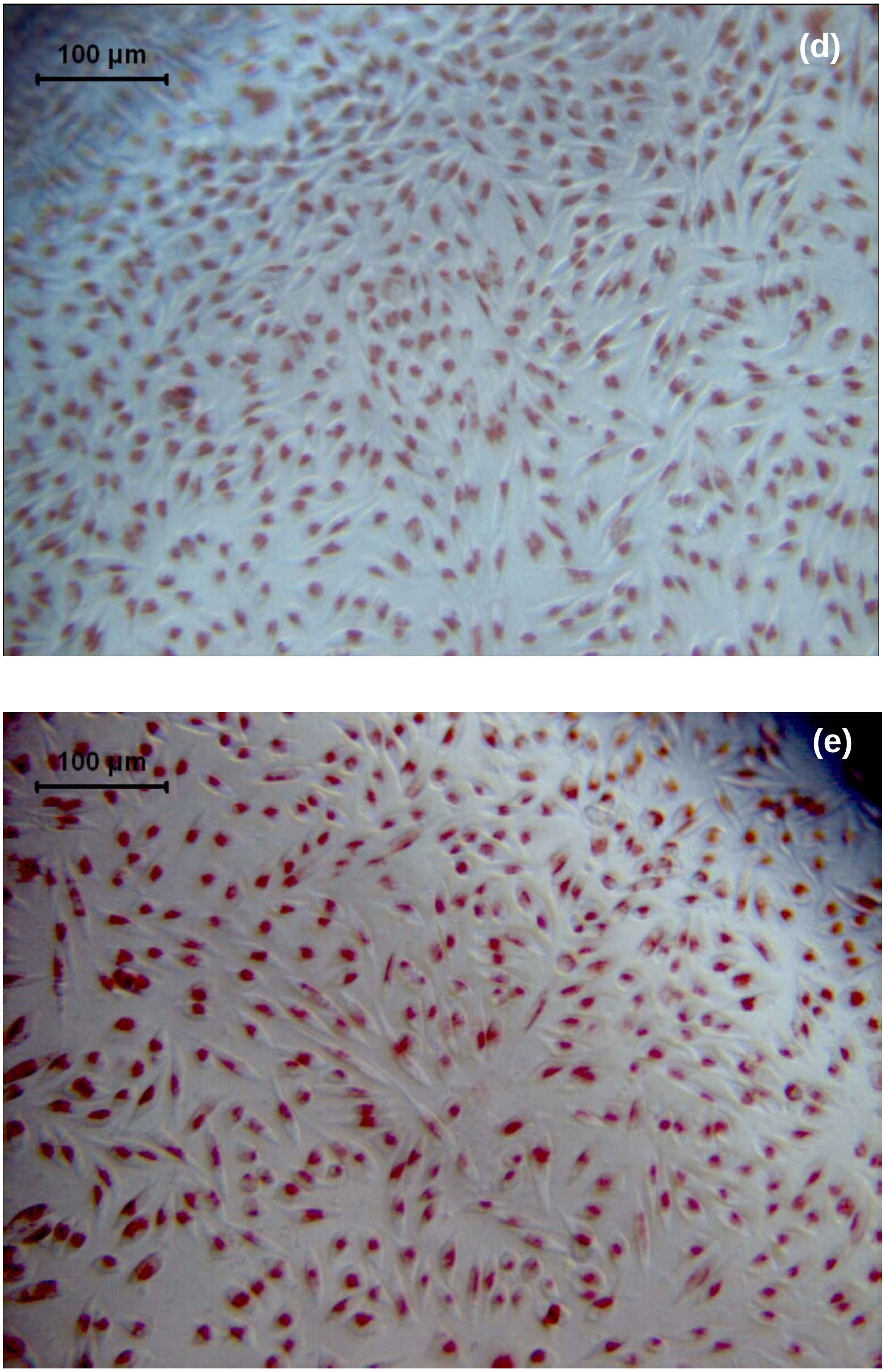

Fig.6.5. *Microscopic images of L 929 cells around pressureless sintered (a) HA, (b) H2Z8, (c) H10Z8, (d) H10Z12 and hot pressed (e) H10Z8 composites*

The toxicity assays are also quantified by counting the number of live cells present per unit area and plotting the results (Figure 6.6).

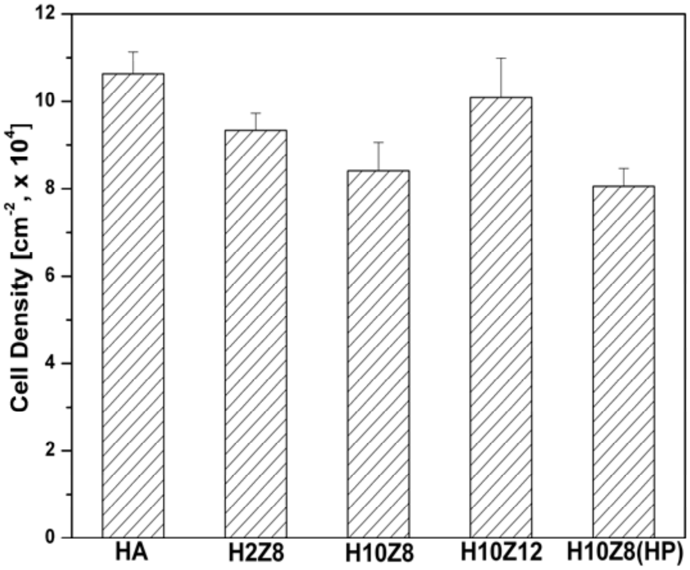

Fig. 6.6 ***Cell density of HA and HA-TZP composites as a function of TZP content ,TZP calcination temperature and sintering condition after culture for 24 hours.***

The cell proliferation rate depends on various chemical and physical aspect of material such as composition, roughness, porosity, morphology and surface energy [6.6, 6.7]. In the present case, the as calculated cell density does not show any significant difference for HA and HA-TZP composite. The, maximum cell density [10.63 x 10^4 cells cm^{-2}] was observed for pure HA and a minimum (8.06 x 10^4 cells cm^{-2}) was observed for hot pressed H10Z8 composite after 24 hrs of culture. Thus, from the cytotoxicity results it can be said that cytotoxicity is less for compositions in which higher fraction of apatite is observed during in vitro SBF aging [section 6.1.1]. This implies that the presence of a more bioactive/resorbable phase lowers the cytotoxicity. But it should be noted that although the relative cytotoxicity values were different for different HA-TZP composites, none of the compositions exhibited a very large amount of cytotoxicity. The HA-TZP composite containing 1200^{O}C calcined TZP (H10Z12) shows a higher cell density of 10.09 x 10^4 cells cm^{-2} compared to 8.41 x 10^4 cells cm^{-2} for batch containing 850^{O}C calcined TZP (H10Z8). Result also shows a marginal decrease in cell count with increased addition of TZP as the cell density for HZ28 and H10Z12 composites is less than that of pure HA.

6.1.3 In vitro Hemocompatibility Test

The blood compatibility of prepared HA-TZP composites (4mm X 4mm) were evaluated in triplicate by an in-vitro hemocompatibility test (ISO 10993-4) after 30 minutes of exposure to human blood as discussed in section 4.6.6. Four empty polystyrene culture dishes were exposed with blood as reference. The percentage hemolysis in the plasma was detected by equation 4.18 (section 4.6.6). Table 6.4 shows the percentage hemolysis in plasma samples after exposure. [6.8, 6.9].

Table 6.4 Percentage hemolysis in plasma samples after exposure

Sample No.	Sample	Percentage hemolysis
1 - a	H2Z8 (PS)	0.06
1 - b	H2Z8 (PS)	0.05
1 - c	H2Z8 (PS)	0.04
2 - a	H10Z8 (HP)	0.04
2 - b	H10Z8 (HP)	0.04
2 - c	H10Z8 (HP)	0.04

The average percentage hemolysis for reference sample after 30 minute of exposure was found to be 0.04 ± 0.00 (n=4). On the other hand the average % hemolysis for sample 1 (air sintered H2Z8 composite) and sample 2 (hot pressed H10Z8 composite) were found to be 0.05 and 0.04 respectively. These values are close to that of reference, thus showing that none of the HA-TZP composite have induced haemolysis during exposure period irrespective of their sintering condition (i.e. pressureless sintered or hot pressed). Thus the HA-TZP composites can also be used in areas of blood contact.

6.2 Conclusions

Thus, the in vitro bioactivity, cytotoxicity and hemocompatibility tests led to the following conclusions:

(a) The in vitro bioactivity of HA-TZP composites were not adversely affected by TZP additions. However the extent of apatite formation was proportional to the porosity of HA-TZP composites and the amount of TCP phase present. Thus bioactivity was very less in hot pressed HA-TZP composites.

(b) The morphology of apatite crystals varied from flowery to ball like structure depending on HA-TZP composition.

(c) The cytotoxicity tests of HA-TZP composites showed no adverse effect with TZP addition. The cytotoxicity results for all composites was in “zero” cytotoxicity group.

(d) The hemocompatibility test did not show any hemolysis induced by the HA-TZP composites.

References

6.1 T. Kokubo and H. Takadama, “How useful is SBF in predicting in vivo bone bioactivity?”, Biomaterials, 27, 2907-2915 (2006).

6.2 A. C. Tas, “Synthesis of biomimetic Ca-hydroxyapatite powders at $37^{o}C$ in synthetic body fluid”, Biomaterials, 21, 1429-1438 (2000).

6.3 Y. Fujita, T. Yamamuro, T. Nakamura, S. Kotani, T. Kokubo and C. Ohtsuki, “The bonding behavior of limestone and abalone shell to bone”, Transactions of the 11th annual meeting of Japanese Society for Biomaterials, 3 (1989).

6.4 T. Kokubo and H. Takadama, “How useful is SBF in predicting in vivo bone bioactivity?”, Biomaterials, 27, 2907-2915 (2006).

6.5 R. Quan, D. Yang, X. Wu, H. Wang, X. Miao and W. Li, “In vitro and in vivo biocompatibility of graded hydroxyapatite-zirconia composite bioceramic”, J. Mater Sci: Mater Med, 19, 183-187 (2008).

6.6 K. Anselme, “Osteoblast adhesion on biomaterials: review”, Biomaterials, 21, 667-681 (2000).

6.7 A. Okumura, M. Goto, T. Goto, M. Yoshinara, S. Masuko, T. Katsuki and T. Tanaka, “Substrate affects the initial attachment and subsequent behaviour of human oestoblastic cells (Saos-2)”, Biomaterials, 22, 2263-2271 (2001).

6.8 R. Quan, D. Yang, X. Yu, H. Wang, X. Miao and W. Li, “In vitro and In vivo biocompatibility of graded hydroxyapatite-zirconia composite bioceramic”, 19, 183-187 (2008).

6.9 L. S. Wan, Z. K. Xu, X. J. Huang, Z. G. Wang and P. Ye, “Hemocompatibility of poly(acrylonitrile-co-N-vinyl-2-pyrrolidone)s:swelling behavior and water states”, Macromole. Biosci., 5, 229 (2005).

Chapter VII

Conclusions and Scope of Further Work

7.1 Conclusions

The present study on the powder processing, densification behavior, mechanical properties, microstructure and invitro bioactive characteristics of HA - TZP composites were undertaken to study the following:

(a) Optimization of HA processing route by preparing HA by two different precipitation routes viz. normal precipitation route (NP) and reverse strike precipitation route (RS).
(b) Preparation of dense HA -TZP nano composites having different weight percent of TZP and to study the different composite properties i.e. phase, microstructure, strength, toughness, hardness and invitro bioactivity.
(c) The effect of two different TZP calcination temperatures (850^{O}C and 1200^{O}C) on the density, phase, microstructure, mechanical properties and bioactivity of the sintered HA-TZP composite.
(d) The effect of hot pressing on phase, density, microstructure, mechanical properties and bioactivity of HA-TZP composites.
(e) The invitro cytotoxic behaviour and hemolysis behaviour of sintered and hot pressed HA-TZP composites.

In the present study, hydroxyapatite (HA) was prepared by two different precipitation routes normal precipitation (NP) route and reverse strike (RS) precipitation route using $Ca(NO_3)_2.4H_2O$ and $(NH_4)_2HPO_4$ as the starting material for HA synthesis. The thermal analysis (DSC/TG) of the as precipitated RS powder showed negligible weight loss throughout the studied temperature range (up to 1250^{O}C). A broad exothermic peak between 350-400^{o}C without any associated weight loss corresponded to crystallization of HA precipitated powder. No other peak corresponding to the decomposition of HA was noticed throughout the range. These results were in consistent with that of FTIR observation where all peak corresponding to that of stoichiometric HA was observed in calcined (850^{O}C) RS powder. The XRD of the calcined (850^{O}C) and sintered (1250^{O}C) NP- HA had both HA and TCP peak but the sintered RS-HA had only HA. The particle size distribution of calcined powder was multimodal for NP and nearly monomodal for

RS route. Thus, based on these observations, it was concluded that RS route was expected to yield more stoichiometric HA compared to NP route .This marked the end of the first part of the study.

The second part of the study involved synthesis of HA -TZP composites containing 2, 5, 7.5 and 10 wt% TZP prepared by RS route. DSC/TG study of the as prepared composite showed that the addition of TZP to HA reduce the decomposition weight loss and promoted crystallization of HA at a low temperature for HA-2 wt% TZP composite. This was a very distinct feature. XRD revealed that in the calcined samples only HA and TZP were present for all composition. TEM analysis of calcined HA-TZP powders show that TZP particle are embedded in HA matrix. The sintered density of HA reached 99% of theoretical at with 2 wt% TZP addition but further addition of TZP reduces the density to a lower value. In the sintered HA-TZP composite, both β-TCP and α-TCP were present along with HA and t-ZrO_2. The bending strength and Vickers hardness of HA (35 MPa, 3.7GPa) increased to 72 MPa and 3.83GPa respectively at 2 wt% TZP addition. At higher TZP content (5, 7.5, 10 wt%), the strength decreased The highest fracture toughness (0.97MPam$^{1/2}$) was recorded for HA - 5 wt% TZP composite, the improvement in fracture toughness is > 50% from sintered HA. SEM microstructures show a grain size reduction of HA with TZP addition. The decrease in strength of HA-TZP at higher TZP addition could be related to the improper densification at higher TZP content, which caused a constraining effect as well due to the differential sintering of TZP agglomerates. The latter effect arose due to agglomeration of 850^{O}C calcined fine TZP particles. Thus an effort was made to reduce the porosity at higher TZP loading by increasing the TZP calcination temperature from 850^{O}C to 1200^{O}C. The higher temperature was expected to increase the TZP crystallite size as well as reduce its agglomeration tendency thereby reducing the differential shrinkage between HA and TZP particulates. Thus the third part of study comprised of the TZP calcination effect on the HA-TZP properties.

In the third part, a thorough study of the effect of TZP calcination temperature on the phase retention, density, microstructure and mechanical property of HA-TZP composite was evaluated. The experimental part consisted of introducing two different TZP (calcined at two different temperatures, viz. 850^{O}C and 1200^{O}C) for the two different sets of HA-TZP composites. An increase in the calcination temperature of TZP from $850^{O}C$-$1200^{O}C$ resulted in density increase for all compositions. However, the use of higher TZP calcination temperature also showed a reduction in HA and TZP phase retention along with the formation of $CaZrO_3$ and TCP. The higher amount of $CaZrO_3$ and TCP was formed due to the combined effect of HA decomposition and the increased reaction between TZP and HA. The mechanical properties showed a remarkable improvement, especially for HA -10 wt% TZP composite with strength, fracture toughness and hardness value being 65 MPa, 1.6 $MPam^{1/2}$ and 5.25 GPa respectively. These improvements were more than 85%, 140% and 40% from sintered HA. The SEM micrographs showed an increase of HA grain size with TZP addition. Although $1200^{O}C$ calcined TZP improved the mechanical properties of the composite at higher TZP content but its adverse effect on the HA and TZP phase retention could not be ignored. Thus, the use of some specialized sintering was needed so that HA-TZP composites could be densified at a much lower temperature which could prevent HA as well as TZP decomposition. It was considered that the use of Hot pressing could effectively avoid phase decomposition of HA and TZP while keeping the density intact.

The fourth part discussed the use of hot pressing in densification of HA-TZP composite at $950^{O}C$ irrespective of their composition and TZP calcination temperature. Hot pressed density of > 98% was observed for all the samples. The maximum flexural strength (120 MPa) and hardness (5.8GPa) obtained for HZ2 composite containing $850^{O}C$ calcined TZP (H2Z8). This increment was significantly higher than any other HA-TZP composition studied here. The toughness value was maximum (1.5 $MPa\sqrt{m}$) for HZ10 composite containing $1200^{O}C$ calcined TZP. In addition to this, a decrease in HA grain size (200nm) was noticed for hot pressed compacts.

The bioactivity of these HA-TZP composites were studied by the formation of apatite on their surface during aging in a SBF solution. The cytotoxicity test results showed the material to be non toxic with the presence and growth of L 929 mouse fibroblast on and around the specimen after 24 hrs of treatment. These, composites also successfully passed the blood compatibility test and showed minimum amount of hemoglobin present on the blood plasma treated with the specimen for 30 minutes.

7.2 Scope of Further Work

The present study on HA-TZP composite showed that under optimized conditions, phase stable stoichiometric HA could be produced by reverse strike precipitation (RS) route. This was also the route adopted for processing of HA-TZP composites. The introduction of TZP in HA matrix slowed the densification rate of the composites (except for HA-2 wt% TZP composites) which apparently affected the improvement in strength, toughness and hardness. The change of TZP calcination temperature though improved the densification behaviour also permitted an extensive reaction between HA and TZP thereby producing TCP, $CaZrO_3$ and reducing the amount of TZP. Hot pressing solved the problem of densification as well reaction between HA and TZP but significant improvement could be observed only for $850^{O}C$ TZP batches. In vitro bioactivity, cytotoxicity and hemolysis established the bioactive and non toxic nature of the composite. However, the study has not answered some of the following points, which can be taken up as the future study:

(a) Why the densification behaviour of HA-TZP improves significantly at 2 wt% TZP additions? This aspect can be studied by studying the densification behaviour and detailed microstructural study of HA-TZP composites with very low TZP additions (0.5 – 3 wt %).

(b) How to ensure a more homogeneous distribution of TZP in HA matrix? This can be studied by processing the composites through different processing route.

(c) The effect of fast firing techniques on the interaction between HA-TZP and on the densification behaviour.

(d) The bioactivity of hot pressed HA-TZP was low. A study should be taken up to increase the bioactivity without sacrificing the fine microstructure.

(e) Evaluation of the chemistry and crystallinity of apatite layer formed on sample surface after SBF soaking for different time period.

(e) Used of this HA-TZP composite to prepare porous scaffold so that the beneficial effect of TZP can be exploited.

(f) Evaluation of the biological properties of the composites to assess the potential of this material as a biomaterial substrate by studying the osteoblast and oestoclast differentiation assays to measure calcium deposition, alkaline phosphatese, osteocalcin etc,

(g) The future study should also include in vivo test in any suitable animal model.

Publications resulting from the Ph.D. work

1. **Y.Nayak**, R.P.Rana, S.K. Pratihar, S. Bhattacharyya, “Low Temperature Processing of Dense Hydroxyapatite-Zirconia Composites”, International Journal of Applied Ceramic Technology, 5, 29- 36 (2008).
2. **Y.Nayak**, R.P.Rana, S.K. Pratihar, S. Bhattacharyya,“Pressureless sintering of Dense Hydroxyapatite-Zirconia Composites”, Journal of Material Science: Materials in Medicines, 19, 2437-2444 (2008).

Curriculum Vitae

Yougojoti Nayak
S/O Mr. A. N. Nayak
Adarsha Colony (In front of S.B.I),
Shaktinagar, Rourkela-769014,
District- Sundergarh, Orissa, INDIA.
Phone No: +91-9937810596 (M)
Email: ynayaknitrkl@gmail.com

Date of Birth: 03.06.1981

Education: Ph.D., M.Sc. (Physics)

Technical Exposure: Publication: **2**, Conferences: **8**

Publications:

1. **Y.Nayak**, R.P.Rana, S.K. Pratihar, S. Bhattacharyya, "Low Temperature Processing of Dense Hydroxyapatite-Zirconia Composites", International Journal of Applied Ceramic Technology, 5, 29- 36 (2008).

2. **Y.Nayak**, R.P.Rana, S.K. Pratihar, S. Bhattacharyya,"Pressureless sintering of Dense Hydroxyapatite-Zirconia Composites", Journal of Material Science: Materials in Medicines, 19, 2437-2444 (2008).